

# **GAMMA-RAY SPECTROSCOPY USING DEPTH-SENSING COPLANAR GRID CdZnTe SEMICONDUCTOR DETECTORS**

by

Benjamin Walter Sturm

A dissertation submitted in partial fulfillment  
of the requirements for the degree of  
Doctor of Philosophy  
(Nuclear Engineering and Radiological Sciences)  
in The University of Michigan  
2007

Doctoral Committee:

Associate Professor Zhong He, Chair  
Professor Ronald F. Fleming  
Professor Glenn F. Knoll  
Associate Professor Thomas H. Zurbuchen

© Benjamin Walter Sturm 2007  
All Rights Reserved

To my parents, Devere and Zita Sturm

## ACKNOWLEDGEMENTS

A great many people have helped to shape me as an engineer and scientist during my graduate studies at the University of Michigan, but the person who deserves the greatest amount of recognition is my advisor, Professor Zhong He. They say that selecting a good advisor is one of the most important factors in determining how successful one will be as a graduate student. I can safely say that I lucked out in this regard and chose a very kind and supportive advisor in Professor He. I was always amazed that whenever the direction of my research was a little unclear to me, I could go and discuss this with him and thirty minutes later I would come out of his office with a whole list of new experiments to run. I thank him very much for all the guidance he has given me over the years, and I hope to someday have the chance to win the money back I lost from him playing poker.

I would also like to thank the other members of my dissertation committee who include Professor Glenn F. Knoll, Professor Ronald F. Fleming, and Professor Thomas H. Zurbuchen, for the time they took out of their busy schedules to read through my dissertation and attend my defense presentation. I feel privileged to attend a university where the person who wrote “the book” in the field that I study (Prof. Knoll) can serve on my dissertation committee. Thank you also to all the members of my research group, past and present, who have all been a vital part of my graduate studies, who include Dr. Scott Kiff, Dr. Feng Zhang, Dr. Dan Xu, Dr. Carolyn Seifert, Miesher Rodrigues, Steve Anderson, Chris Chwasz, James Berry, and Dr. José Pérez.



I was so fortunate to have such an intelligent group of people there to support me, while also getting along so well and having a lot of fun together. A special thank you is extended to Cari for being a great GSI and inspiring me to go into this field in the first place. I would also like to say a special thank you to Scott for tolerating me as a labmate the last few months. I appreciate his ability to find so much enjoyment together with me in listening to White Town and watching old skits of the Swedish Chef.

I have been so gifted over the years to have a great group of friends there to enjoy life together with me and to provide encouragement and support when I needed it most. Noé has been one of these great friends who would never turn down a chance to go dancing to Arabic music Friday night at Oz or passing juggling clubs. Belén and Anja are two cool geologists who always gave me so much to laugh and smile about. I will never forget my special graduation cap that they created for me. I would like to thank my good friend Gautam for not harassing me too much for being at Michigan during all three generations of the Kamlapurkar family. I would like to thank all my friends from 518 Hill, Jon, Rick “Harpster”, Mike, and Kevin for all the great times we shared together. Thank you to the decadence team, who include Carmen, Tara, Niels, and Sasha, for enjoying nature with me during our fun backpacking trips together and sharing in the joy of roasted garlic and Feuerzangenbowle. Thank you to all the great members of the Ann Arbor Juggling Arts Club and in particular Paul, Lena, Dave, Bruce, Sara, Darshan, Fred, and Deanna. I would also like to thank my special German friends Stephan, Eva, and Daniel and my Russian friend Elizaweta. I feel so fortunate to have a great group of friends from around the world. Thank you to my other friends from the NERS department who include Kathy, Troy, and Yan. I recognize this list is entirely incomplete, so thank you to all the other great

friends I have made over the years. The world is a better place because of you!

Lastly, I would like to extend a special thank you to my entire family. I am truly blessed to have such wonderful parents, Devere and Zita Sturm, there to love and support me. They have both been so encouraging towards my decision to go to grad school and without them I doubt I would be here finishing my Ph.D. You both are my lifelong role models. Thank you also to my sisters. Anne has always been there for me when I needed her most. I am glad that you finally listened to me and took my advice to attend Stammtisch. Eva and Julia have both given me a lot of great memories and I will never forget our Sturm sibling trip to Vegas. I would also like to say danke schön to my Tante Erika in Germany for being my European home away from home and for spending hours philosophizing about life with me over a good German beer. Thank you to you all.

# TABLE OF CONTENTS

<b>DEDICATION</b> . . . . .	<b>ii</b>
<b>ACKNOWLEDGEMENTS</b> . . . . .	<b>iii</b>
<b>LIST OF FIGURES</b> . . . . .	<b>viii</b>
<b>LIST OF TABLES</b> . . . . .	<b>xii</b>
<b>CHAPTER</b>	
<b>I. Introduction</b> . . . . .	<b>1</b>
1.1 Gamma-ray spectroscopy using semiconductors . . . . .	1
1.2 Room-temperature semiconductor detectors . . . . .	4
1.3 Single-polarity charge sensing . . . . .	6
1.4 Previous work on coplanar grid CdZnTe . . . . .	9
1.5 Project objectives . . . . .	10
<b>II. Theory</b> . . . . .	<b>13</b>
2.1 Charge induction and the Shockley-Ramo theorem . . . . .	13
2.2 Theory of single-polarity charge sensing . . . . .	15
2.2.1 Frisch grid . . . . .	16
2.2.2 Coplanar grid . . . . .	20
2.3 Electron trapping compensation techniques . . . . .	23
2.3.1 Relative gain method . . . . .	24
2.3.2 Depth sensing method . . . . .	25
2.4 Radial sensing . . . . .	28
<b>III. Coplanar Grid Electrode Design and Experimental Arrangement</b> . . . . .	<b>31</b>
3.1 Third-generation coplanar anode design concept . . . . .	33
3.2 Electrostatic simulations . . . . .	34
3.3 Sensing methods to verify improved electrode design . . . . .	36
3.4 Readout hardware . . . . .	38
3.5 Readout software . . . . .	42
<b>IV. Experimental Results for Coplanar Grid Detectors</b> . . . . .	<b>44</b>
4.1 eV Products detector results . . . . .	44
4.1.1 Methods of operation . . . . .	45
4.1.2 Spectroscopic performance . . . . .	48
4.1.3 Validation of improved electrode design . . . . .	49
4.2 Measurement results using radial sensing . . . . .	50

4.2.1	Second-generation design . . . . .	50
4.2.2	eV Products design . . . . .	55
4.2.3	Third-generation design . . . . .	55
4.3	Yinnel Tech / BSI detector results . . . . .	56
4.3.1	Detector fabrication . . . . .	56
4.3.2	Electrode configuration and measurements . . . . .	58
4.3.3	Detector spectroscopic performance . . . . .	59
4.3.4	Discussion of asymmetric characteristics . . . . .	64
<b>V. Detector Modeling . . . . .</b>		<b>67</b>
5.1	Simulation methods . . . . .	67
5.2	Comparison study of 2 electron trapping compensation techniques . . . . .	71
5.3	Surface effects of CZT . . . . .	74
5.3.1	Modeling the electron trajectory . . . . .	76
5.3.2	Modeling the spectrum . . . . .	77
<b>VI. Multi-Pair Coplanar Grid Detector Design and Results . . . . .</b>		<b>84</b>
6.1	Multi-pair coplanar grid concept . . . . .	84
6.2	Detector evaluation . . . . .	89
6.2.1	Low surface resistance and high voltage breakdown . . . . .	89
6.2.2	Biasing configuration and signal readout method . . . . .	91
6.2.3	Spectroscopic performance . . . . .	93
6.2.4	Further discussion . . . . .	94
<b>VII. Other Factors Affecting Performance . . . . .</b>		<b>97</b>
7.1	Temperature effects on CZT . . . . .	98
7.1.1	Results and evaluation for temperature study . . . . .	98
7.2	Depth sensing using summation signal . . . . .	106
7.3	Factors contributing to peak broadening . . . . .	108
<b>VIII. Summary and Future Work . . . . .</b>		<b>113</b>
8.1	Summary of results . . . . .	114
8.2	Recommendations for future work . . . . .	120
<b>BIBLIOGRAPHY . . . . .</b>		<b>125</b>

## LIST OF FIGURES

### Figure

2.1	Figure showing that the final anode signal will be a combination of the electron and hole movement in the device. . . . .	17
2.2	Figure illustrating the Frisch grid as implemented in gas ionization chambers. . . .	19
2.3	Figure illustrating the single polarity charge sensing concept as it is applied to coplanar grid electrodes. . . . .	22
2.4	This figure illustrates how the slope of the subtracted signal weighting potential in the far-grid region can be adjusted. . . . .	26
2.5	Subtraction circuit weighting potential with the relative gain set to some number less than 1. This figure depicts how the effect of electron trapping can be compensated. 26	
2.6	Weighting potential for either coplanar grid electrode along a line passing through the middle of the detector at a fixed depth near to, but greater than 1 pitch, from the anode. The convex shape is caused by the boundary electrode, where the weighting potential is forced to 0 at the anode surface. . . . .	29
2.7	Induced charge of a single electron formed at depth Z, at two different radial positions, and traveling to the collecting anode. . . . .	30
3.1	Generation 1 coplanar anode design. . . . .	32
3.2	Generation 3 coplanar grid design consisting of two coplanar anodes and a boundary electrode. This design is $15 \times 15 \text{ mm}^2$ in area. . . . .	34
3.3	Weighting potential for the selected generation 3 design as a function of position at a distance of 1.5 mm from the anode surface. The two figures show the weighting potential along the x-line (top) and along the y-line (bottom) as indicated in Figure 3.2. . . . .	37
3.4	Block diagram representing the signal chain employed for coplanar grid CZT. . . .	38
3.5	Plot of a typical pulse waveform after the preamplifier stage for the collecting anode, noncollecting anode, and cathode. The signal from the subtraction circuit is also shown. . . . .	39
3.6	Picture of the detector box including the detector, 3 preamplifiers, and a subtraction circuit. . . . .	40

3.7	Peak-hold circuit pulse waveforms. The DAQ card is set to acquire a sample on the downward slope of the trigger signal. . . . .	41
3.8	Picture of the 4-channel peak hold circuit. . . . .	41
4.1	Picture of the eV Products detector. The detector itself is housed inside of the yellow protective package. . . . .	45
4.2	Figure illustrating the three outermost electrodes and how the collection of the electrons is affected by the detector biasing conditions. . . . .	46
4.3	Cs-137 spectrum obtained using an eV Products MO2 2-2 square detector utilizing the depth sensing method. Condition (a) results in only the electrons generated in the central region being collected by the coplanar anodes, whereas, in (b) electrons generated in the whole device are collected by the coplanar anodes. . . . .	47
4.4	eV Products M02 2-2 square detector spectrum of a Cs-137 source obtained using the relative gain method for electron trapping compensation. This spectrum was taken with a cathode bias of -1700 V and anode bias of -80 V. . . . .	49
4.5	Energy spectra at each depth using a Cs-137 $\gamma$ -ray source for (a) the eV Products generation 2 detector and (b) the generation 3 detector, both spectra were taken with a cathode bias of -1700 V and anode bias of -80 V. The plot in (c) shows the energy resolution (% FWHM) as a function of the interaction depth for both electrode configurations. . . . .	51
4.6	Cs-137 spectra taken at different radial positions at one particular interaction depth for (a) the generation 2 detector, where spectra numbers 1-4 indicate increasing radial positions (b) the I9-01 detector with eV's generation 2 design and (c) the MO2 2-2 square detector with the generation 3 design, where both (b) and (c) were taken with a cathode bias of -1700 V and anode bias of -80 V. In (b) and (c), numbers 1 $\rightarrow$ 2 $\rightarrow$ 3 indicated increasing radial positions. . . . .	52
4.7	Generation 2 detector weighting potential as a function of lateral position. The data points shown are along a center section of the device at a depth of 1 mm from the anode surface. . . . .	54
4.8	Picture of the BSI detector. The 6 wire leads are connected to the 3 electrodes on opposite sides of the detector. . . . .	56
4.9	662 keV $\gamma$ -ray energy spectrum for the CZT2-4-2 detector using the relative gain compensation method. Results in the range of 1.65% to 1.70% were consistently achieved. . . . .	60
4.10	These measurements were taken using the BSI CZT2-4-2 detector with side 'A' biased as the anode. The cathode was set to -1400 V and the noncollecting anode was set to -45 V. . . . .	62
4.11	BSI CZT2-4-2 detector measurements with side 'B' biased as the anode. The cathode was set to -1200 V and the noncollecting anode was set to -50 V. . . . .	63
4.12	Cs-137 spectrum taken with the BSI CZT2-4-1 detector employing the depth sensing method. In this spectrum, the 31 keV X-ray from Ba-133 is clearly visible. . .	64

5.1	Block diagram highlighting the steps for the simulations discussed in this chapter.	68
5.2	Simulated Cs-137 spectra for the coplanar grid detector, where (a) was acquired employing the depth sensing method with a relative gain of 1 and (b) was acquired employing the relative gain method with an optimized relative gain of 0.81. . . . .	73
5.3	Resolution versus depth data separated by interaction location where (a) is for a relative gain of 1 and (b) is for a relative gain of 0.81. The differences observed between (a) and (b) are fairly minimal. . . . .	75
5.4	Illustration of the electron track for electrons originating at $z = 8$ mm determined for a cathode bias of -1200 V and a coplanar anode bias of 43 V. The effects for two different boundary conditions are shown on the same plot. The left side was calculated for a linearly varying potential at the surface and the right side was calculated when no potential was applied at the surface (floating case). The right side shows better focusing of the electrons. . . . .	77
5.5	Illustration of the electron track determined for a cathode bias of -1200 V and a coplanar anode bias of 86 V. A critical bias was achieved for the right side (floating potential case) where full electron collection takes place. . . . .	78
5.6	Plot of the potential at the surface of the detector, where the left and right sides are the positions of a collecting anode and the middle is the position of a noncollecting anode. The convex shape in the potential for the floating case helps to focus electrons better to the collecting anode than for the linearly varying case. . . . .	78
5.7	Simulated spectra for the case in which the oxide layer was left floating where (a) is with a coplanar bias of 43 V and (b) is with a coplanar bias of 86 V. For these simulations the cathode was set to -1200 V. The effects of incomplete charge collection are shown in (a). . . . .	81
5.8	Experimental data taken with the BSI CZT2-4-1 detector using a cathode bias of -1200 V and a noncollecting anode bias of -20 V (a) and -50 V (b). The degradation in resolution observed in (a) was likely the result of incomplete charge collection. .	83
6.1	Illustration of the multi-pair coplanar grid design. This design consists of 4 sets of grid pairs surrounded by a single boundary electrode (shown in the green). The multi-pair coplanar electrodes were placed on both the top and bottom of the crystal. The anode surface area is 30 mm $\times$ 30.5 mm and the final crystal thickness was 12 mm. . . . .	85
6.2	Plot of the weighting potential 1.25 mm from the anode surface along a line depicted in the inlaid figure. The grid I data (blue) is the weighting potential of the subtracted grid I signal. The grid I + grid IV data (red) is the resulting weighting potential when the subtracted signal from grids I and IV are added together. This plot illustrates that the weighting potential is more uniform in the border region ( $y = 10 \rightarrow 20$ ) for the summed grid case than it is for the single grid case. . . . .	88
6.3	A view of one of the anode surfaces for the multi-pair coplanar grid detector. The electrodes are color coded to a particular color hook-up wire such that the electrodes can be distinguished properly biased. . . . .	90

6.4	Illustration of the breakdown region relative to the grids on the cathode side. Operation of the detector was limited to 1200 V for grids I and II on the cathode side due to the large noise. However, the corresponding grids I and II on the anode side could be operated at 1700 V with stable behavior. This indicates that the breakdown region may be located closer to the cathode side. . . . .	91
6.5	A cut-out illustration of the multi-pair detector in the center of the device. This indicates the proper biasing of the detector such that the strips alternate between the collecting anode bias ( $V_{ca}$ ) and the noncollecting anode bias ( $V_{nca}$ ). . . . .	92
6.6	Large volume detector data from grid I only using a 662 keV gamma-ray source. This data was acquired with a cathode bias of -1700 V and a noncollecting anode bias of -35 V. The data indicates that the energy resolution is poorest near the middle of the device. . . . .	95
7.1	Spectrum taken with the eV Products detector MO2 2-2 square for each temperature setting using a 662 keV $\gamma$ -ray source. Spectrum 1 (blue) is the initial temperature setting and spectrum 13 (purple) is the final measurement. The spectrum at -30°C is characterized as a low energy continuum. . . . .	100
7.2	Yinnel Tech/BSI CZT2-4-2 detector spectrum taken at each temperature setting. For this case, spectrum 1 (blue) was the initial temperature setting and spectrum 10 (yellow) was the final one. The behavior is similar to the other detector, which also resulted in a low energy continuum for the -30°C temperature setting. . . . .	101
7.3	$\mu_e \tau_e$ product values for two detectors as a function of operating temperature (20°C $\rightarrow$ 10°C $\rightarrow$ 5°C $\rightarrow$ -5°C $\rightarrow$ -10°C $\rightarrow$ -20°C). Measurements were repeated at each temperature for the eV Products detector while heating. Only three measurements were performed for the BSI detector during the heating cycle (-20°C $\rightarrow$ -5°C $\rightarrow$ 10°C). . . . .	102
7.4	BSI CZT2-4-2 detector $\mu_e$ values for changing temperature where the leftmost point is the initial measurement and the rightmost point is the final measurement. . . . .	103
7.5	Pulse waveforms obtained with the BSI CZT2-4-2 detector at -20°C. . . . .	104
7.6	Experimental results for the BSI CZT2-4-1 detector where (a) is the 3-D depth spectrum obtained using $d = \text{Sum}/A$ and (b) gives a comparison in the photopeak area for both depth sensing methods. . . . .	109
7.7	Simulation results where (a) is the 3-D depth spectrum obtained by taking $d = \text{Sum}/A$ and (b) gives a comparison of the peak area. The simulation data agrees with the experimental data very well. . . . .	110



## LIST OF TABLES

### Table

3.1	Figure of merit (FOM) and capacitance data calculated by way of simulation. . . .	36
4.1	Electron transport measurement data taken by BSI for 2 Yinnel Tech detectors. . .	58
4.2	Coplanar grid detector measurements taken by BSI after fabrication. The energy resolution measurements were taken using the relative gain method for electron trapping compensation and with side ‘A’ biased as the anode. . . . .	58
4.3	Energy resolution data for both Yinnel Tech/BSI detectors using the depth sensing or relative gain methods for electron trapping compensation and with either side ‘A’ or side ‘B’ biased as the anode. . . . .	64
5.1	Parameters which were used for modeling the coplanar grid CZT detector in Geant4.	70
7.1	Results quantifying each component of peak broadening included into the model. The data in the middle shows the total spectrum % FWHM at 662 keV after adding in each component listed in sequential order. The data along the right details the % FWHM for each of these components individually. . . . .	111

## CHAPTER I

### Introduction

The coplanar grid CdZnTe gamma-ray detector was first introduced as a means to read out the signals from the relatively fast moving electrons in CdZnTe while mitigating the normally detrimental effect of slow moving holes. This readout technique was the main driving force that helped to advance the utilization of CdZnTe as a viable gamma-ray detection medium. Since the beginning of coplanar grid CdZnTe, many advancements have been made that have resulted in better performing detectors. Some of which are a result of better crystal growth and detector fabrication techniques. However, many advancements are a direct result of a deeper physical understanding of this detection method. This document will detail the many such improvements and discoveries made during the course of this research.

#### 1.1 Gamma-ray spectroscopy using semiconductors

At the onset of gamma-ray spectroscopy, NaI(Tl) scintillation detectors were the most predominantly used gamma-ray detectors. These detectors have the advantage of good gamma-ray detection efficiency in addition to the relatively easy implementation in portable instrumentation. Even today, NaI(Tl) is the most commonly employed gamma-ray detection medium [1]. The main drawback of this material is the generally poor energy resolution that can be obtained of about 6% FWHM at 662

keV. The cause of this is due to the relatively small number of information carriers produced at the photocathode of the photomultiplier tube, which is a combined result of the high ionization energy of NaI(Tl) of  $\sim 25$  eV and the small quantum efficiency of the photocathode. When good energy resolution is of the utmost importance, an alternative to NaI(Tl) must be sought.

Semiconductors are solid-state materials that possess the properties of crystallinity with a band structure that is neither totally conducting nor insulating. These materials typically have band gap energies of 1-3 eV and ionization energies just slightly greater. For Si, a ubiquitous semiconductor material, the average particle energy loss per electron-hole pair produced is around 3.6 eV at room temperature. This means that for a 662 keV gamma-ray photoelectric interaction,  $\sim 1.8 \times 10^5$  e-h pairs are produced. The statistical limit in energy resolution is governed by the number of information carriers  $N$  produced. The general formula that describes this limit is given by Equation (1.1)

$$R|_{\text{statistical limit}} = 2.35 \sqrt{\frac{F}{N}} \quad (1.1)$$

where  $F$  is the Fano factor. A good approximation of  $F$  for Si is 0.1. Hence, at 662 keV the energy resolution for Si due only to statistical fluctuations in the number of charge carriers, is limited to 0.18%. This is significantly better than in NaI(Tl) scintillators.

Another favorable property of semiconductors are their fast response. The drift velocity of the charge carriers  $\nu$  is given by  $\nu = \mu \mathcal{E}$  where  $\mathcal{E}$  is the electric field magnitude and  $\mu$  is the carrier mobility. This relationship generally holds for electric field strengths below the point at which a saturation velocity is achieved. At the saturation velocity, further increases in the electric field will have no effect on the charge carrier drift velocity. For a 0.1 cm Si detector, charge carriers drifting at the

saturation velocity can be collected in under 10 ns [1]. Fast collection times generally results in less charge trapping, since charge carriers tend to have an average lifetime in the crystal, which can be on the order of  $100\mu\text{s}$  for Si [2]. Hence, this means that a large fraction of all the carriers formed by the incident radiation should be collected. More efficient collection of charge carriers will ultimately result in better energy resolution. In addition, the fast response of semiconductor detectors generally results in better noise properties, since shaping times in the pulse processing electronics can be kept quite small, which results in less parallel noise being integrated into the final signal.

Gamma-ray detection requires that the material have a large atomic number, or  $Z$  value. This is because the probability for a photoelectric interaction to occur in a given material is approximately proportional to  $Z^{4.5}/E^{3.5}$ , where  $E$  is the energy of the incident gamma-ray. Photoelectric absorption is the preferred mode of gamma-ray interaction, because it entails full energy deposition in the device. For this reason, Si is generally not a very good material for gamma-ray detection, because the  $Z$  value of Si has a relatively small value of 14. In addition, detectors using Si tend to have relatively small thicknesses which results in even poorer detection efficiency. A much better material for gamma-ray detection is Ge, which has a  $Z$  value of 32. Refining techniques have been developed to render a version of Ge called high-purity germanium (HPGe). HPGe has the advantage that much larger depletion depths can be achieved, resulting in a greater active volume for gamma-ray detection. The combination of high  $Z$ , relatively large volumes, and an  $\epsilon$  value of only  $\sim 3$  eV has lead to the prevalence of HPGe when energy resolution is of the utmost importance. As a means of comparison, this material can achieve 0.14% energy resolution at 662 keV [3]. However, a major drawback of HPGe is the necessity to cool it to cryogenic

temperatures of 77 K, because the small bandgap (0.7 eV) results in a large amount of thermally induced leakage current when operated at room temperature. The requirement to keep HPGe cooled to liquid nitrogen temperatures makes it difficult to employ this material in portable instrumentation. Hence, a push for finding room-temperature semiconductor detectors that can achieve performance near to HPGe, but with the added capability to operate at room temperature has been ongoing for the past few decades.

## 1.2 Room-temperature semiconductor detectors

Room-temperature semiconductor gamma ray detectors all possess a similar series of attributes. These include a wide bandgap, generally greater than 1.5 eV, which limits the number of thermally generated conduction electrons and hence dark current noise at room temperature. They also have a high  $Z$ , helping to maximize the cross section for photoelectric absorption. In addition, these detectors are almost exclusively based on the use of compound semiconductors. The most commonly employed semiconductors for such purposes include  $\text{HgI}_2$ ,  $\text{CdTe}$ , and  $\text{Cd}_{1-x}\text{Zn}_x\text{Te}$ .

$\text{CdTe}$  has been studied extensively since the 1960s [4–6]. This material has a high  $Z$  of 48 and 52, resulting in good gamma-ray stopping efficiency, and has a bandgap energy of 1.52 eV [1]. Charge carrier mobilities are  $1000 \text{ cm}^2/\text{Vs}$  for electrons and  $80 \text{ cm}^2/\text{Vs}$  for holes [2]. The low hole mobility results in a high percentage of hole trapping and hence incomplete charge collection. Hence,  $\text{CdTe}$  devices employing the planar electrode configuration are generally limited to thinner devices (1-2 mm thick). Another detrimental property of this material is the polarization effect that is often observed [7, 8]. This effect is thought to be caused by the build-up of space charge in the material over time, resulting in a degradation in spectroscopic performance.

Although CdTe is a wide bandgap semiconductor, it has a relatively high leakage current, which ultimately contributes to more noise in the system.

HgI<sub>2</sub> has been investigated since the 1970s as a room-temperature detector [9–12]. It is an even more efficient detector for gamma-ray detection than CdTe due to its high  $Z$  of 80 and 53. This material has another distinct advantage in that leakage current at room temperature is very low because of the generally large bandgap energy of 2.13 eV [1]. Hence, operation at high electric fields of 2500 V/cm or greater, resulting in better charge transport properties, is possible [13]. However, this material also suffers from a very low hole mobility of 4 cm<sup>2</sup>/Vs. Hence, incomplete charge collection is also a problem with this material. In addition, polarization seems to be a persistent problem with HgI<sub>2</sub> that hampers performance [14]. Although, it is found that maintaining the bias for a period of several weeks helps to limit the effect of polarization [15].

Detectors based on Cd<sub>1-x</sub>Zn<sub>x</sub>Te (CZT) have a slightly more recent history [16,17]. This semiconducting material is formed by the alloying of CdTe with ZnTe where  $x$  gives the ZnTe blending concentration [1]. The addition of Zn to the melt of Cd and Te during growth helps to reduce the dislocation density and thus gives rise to higher quality materials [2]. CZT has a bandgap energy range of 1.53-1.64 eV depending on the concentration of Zn in the material [1]. It has a similar photoelectric interaction probability to CdTe, but because of its slightly larger bandgap, it has a higher resistivity ( $10^{10} - 10^{11}$  Ωcm) than CdTe and thus improved leakage current properties. Unlike HgI<sub>2</sub> or CdTe, CZT detectors seemingly do not suffer from the effects of polarization. This material does possess the characteristic of much higher electron mobility (1350 cm<sup>2</sup>/Vs) than hole mobility (120 cm<sup>2</sup>/Vs), giving rise to relatively stationary hole movement within the electron collection time. Therefore,

this material also suffers from the characteristic of incomplete charge collection. However, special sensing methods can be used to mitigate the effects of low hole mobility, which will be the topic of much discussion in this dissertation.

### 1.3 Single-polarity charge sensing

The aforementioned property of poor hole transport in room-temperature semiconductors means that incomplete charge collection generally results for thicker detectors ( $> 5$  mm in thickness). For the planar detector configuration, this will cause a significant dependency in the induced charge as a function of the gamma-ray interaction. Hence, the resulting signal will be highly position dependent and thus energy resolution will be severely degraded. One obvious method to combat this issue would be to fabricate thinner devices such that the holes and electrons can both be collected within a short enough time. However, thinner devices will be at the expense of much poorer gamma-ray detection efficiency. When thicker devices with higher efficiency are desired, then alternative methods must be developed to address the incomplete charge collection issue.

Some methods used to treat the effect of incomplete charge collection rely on pulse processing electronics. One such method accomplishes pulse-shape discrimination, which selects events with the same conditions for charge induction [18]. This is done by selecting pulses with nearly the same risetime. By doing so, the energy resolution can be drastically improved, however at the cost of poorer efficiency. Another method employs charge-loss compensation, which analyzes the detector signals and applies an appropriate signal correction to compensate for the effect of incomplete hole collection [19]. The charge-loss compensation technique has achieved good energy resolution results ( $< 1.8\%$  FWHM), but such results are only achievable with

detectors that have superior material uniformity. Moreover, this technique generally relies on fairly sophisticated electronics for pulse shape analysis, which adds another level of complexity to the system.

It has been found that a much better way to address the hole trapping issue in room-temperature semiconductor detectors is to utilize single-polarity charge sensing. This term is derived from the manner that only one polarity of charge (the negative electrons) is sensed in order to infer the energy deposited by the incident gamma-ray. This is advantageous because the effect of poor hole mobility can be mitigated, since the resulting signal will only be sensitive to the fast moving electrons. This method was first carried out by Frisch in 1944 for gas ionization chambers [20]. Frisch employed a gridded electrode, now known as a Frisch grid, placed inside of the ionization chamber surrounding the anode. The Frisch grid acts as an electrostatic shield to the region between the cathode and the grid, while making the region between the grid and the anode highly sensitive to the movement of charge. Therefore, events that occur between the cathode and the grid, which constitutes most of the detector volume, will result in the fast moving electrons passing through the grid and inducing all of their charge on the anode, while the slow moving positive ions will travel in the opposite direction and induce no charge on the anode. This charge sensing method has helped to greatly improve the performance of ionization chambers [21]. However, the Frisch grid scheme would be difficult to implement for semiconductor detectors, since this would require that the grid be embedded into the crystal material. Therefore, other methods employing single polarity charge sensing for semiconductors must be sought.

The first major stride in single polarity charge sensing of room-temperature semiconductor detectors was made in 1994 by Luke [22]. Luke developed an electrode



structure called the coplanar grid, which was designed for use with semiconductors. The coplanar grid consists of a series of narrow strips, which are connected together in an alternate fashion producing two sets of interdigitated grid electrodes. By biasing these grid electrodes properly and taking the difference between the two grid signals, one can achieve a resulting signal that is only sensitive to the movement of electrons. Hence, the coplanar grid structure achieves single polarity charge sensing much like the Frisch grid. The primary advantage of this electrode design is that it can be constructed on the surface of the crystal. In theory, coplanar grids can be applied to any of the compound semiconductors previously described. However, because of the good material properties of CZT, this research work solely focused on the implementation of coplanar grid on CZT crystals.

Other methods for single polarity charge sensing have also been studied. One such method that has been extensively used is the pixellated method. This technique employs small pixel electrodes to sense the signal due to charge carriers drifting in close proximity to the anode structure. When biased to collect electrons, the pixel signal will be almost entirely sensitive to the electrons being collected and insensitive to the holes. This is known as the small pixel effect and is used to make the effects of hole trapping less significant [23]. A dramatic improvement in energy resolution was shown using this method on large volume CZT detectors [24, 25]. An added benefit to the pixellated readout system is the ability to achieve 3-D position information of the gamma-ray interaction [26]. Although seemingly less popular than the pixellated readout system, other single polarity charge sensing methods have been studied. Included in these are hemispherical detectors [27], parallel strip Frisch grid detectors [28–30], a detector employing a control electrode surrounding a small pixel anode [31], and capacitive Frisch grid detectors [32]. Advantages and

limitations of these methods was previously reviewed by He [33].

#### 1.4 Previous work on coplanar grid CdZnTe

Prior to this dissertation work, much effort was devoted to the understanding and improvement of coplanar grid CZT detectors. In 1995, Luke first reported results on a  $5 \times 5 \times 5 \text{ mm}^3$  crystal having an energy resolution at 662 keV of 3.7% [34]. These results were achieved without correcting for the effects of electron trapping. Electron trapping is a very important effect to account for, since thicker devices will result in an attenuated signal ( $\sim 5\text{-}10\%$  for a 1 cm thick device) for cathode side events. This will then give rise to a distribution in the photopeak signal depending upon where the interaction takes place in the detector. Hence, in order to achieve the ultimate in spectroscopic performance, one must compensate for the effects of electron trapping. Also in 1995, Luke proposed a technique known as the relative gain method for electron trapping compensation [34]. This method applies a relative gain component between the two coplanar grid signals before signal subtraction. By applying the optimal relative gain value, one can achieve nearly uniform charge induction efficiency for all depths in the device, assuming that charge trapping is uniform within the detector. According to simulations, using this method, energy resolutions close to the charge generation statistics limit can be achieved [35,36]. In reality, Luke reported an energy resolution of 2.4% at 662 keV on a  $1 \text{ cm}^3$  crystal employing this method for electron trapping compensation [35].

Coinciding with the introduction of the relative gain method, He *et al.* proposed a method using depth sensing to correct for electron trapping [37–39]. This method uses the ratio of the cathode signal and the subtracted signal to determine the depth of the gamma-ray interaction. In this way, spectra can be obtained as a function of

interaction depth, allowing one to compensate for electron trapping for any depth-dependent function. Employing the depth sensing method, He *et al.* reported energy resolution results of 1.79% and 1.97% at 662 keV with two different 1 cm<sup>3</sup> detectors. In the early coplanar grid designs, He *et al.* observed significant energy resolution degradation near the coplanar anodes, which was later attributed to the weighting potential non-symmetric effect [40,41]. Based on this understanding, He *et al.* proposed using a boundary electrode surrounding the coplanar anodes which would aid in balancing the weighting potentials along the edges of the detector. With this new design, named generation 2, the difference of the weighting potentials along the edges of the detector was significantly reduced. Still, the anode geometry was not optimized, and so a generation 3 design was proposed. In this design, the strip widths of the two outermost grids and three outermost gaps were fine-tuned in order to minimize the difference of the weighting potential about the area of the detector. Preliminary results using the generation 3 design were less than ideal, with energy resolutions of 3.2-4.1% FWHM at 662 keV at different depths in the detector. However, the detector suffered from significant noise at low operating bias, and it was believed that much improved results could be achieved using the same design on a better fabricated detector.

## 1.5 Project objectives

This dissertation work continues where the coplanar grid CZT project previously left off. That is, continuing to study the effects that go into determining coplanar grid detector performance. Previous work showed that the coplanar grid design plays an essential role in establishing the most uniform response. And so, the generation 3 design was proposed, which sought to improve upon the response uniformity. Using

this design, we studied the performance of coplanar grid detectors and attempted to determine the limit in energy resolution that can be achieved with such devices.

Chapter II of this dissertation begins with the theoretical background. To start, a discussion of the Shockley-Ramo theorem and its implications are given along with the concept of single-polarity charge sensing. Then, the coplanar grid readout method is addressed and different compensation techniques are proposed. Chapter III describes the generation 3 coplanar grid design and the simulation tools used to model it. In addition, details of the readout hardware and software used to acquire and process the signals from the detector are also discussed. In Chapter IV experimental results from 2 different sets of coplanar grid detectors are given. Results from these detectors are compared to those obtained from previous detectors employing different coplanar grid designs. One particular set of detectors produced very good results, which will be discussed and analyzed in detail. Chapter V involves modeling the coplanar grid detectors through simulation techniques. These simulation tools give us an additional approach to better analyze detector characteristics. Here we analyzed different electron trapping compensation methods. We also examined surface effects of CZT and how this can affect performance. Chapter VI describes the concept of the multi-pair coplanar grid design. Methods to account for certain detrimental effects are given and how we plan to achieve similar performance to the smaller volume detectors but with much greater detection efficiency. Preliminary results for this detector are shown. Chapter VII details some other factors that have an important role in determining coplanar grid detector performance. This includes a temperature effects study on CZT. In addition, another depth sensing technique was examined. Some of the major sources of peak broadening were analyzed. Lastly, Chapter VIII gives a summary of the results and conclusions that can be drawn.

Recommendations for future work are also provided.

## CHAPTER II

### Theory

Gamma-ray detection is always done in an indirect manner. This means that the gamma-rays themselves do not directly ionize the material through which they pass. Instead, the detection of these uncharged particles requires that interactions must take place that impart a portion or all of their kinetic energy to the medium. In semiconductors, these interactions will produce an energetic electron which will cause the formation of many electron-hole pairs. It is these electron-hole pairs that will act as the charge carriers of the device. The detection system must therefore sense the charge carriers produced in order to determine the amount of energy initially imparted by the incident gamma-ray. This chapter will discuss the theory of how the signal is formed in the coplanar grid detector. A detailed analysis will be given of single-polarity charge sensing and the methods used to account for electron trapping.

#### 2.1 Charge induction and the Shockley-Ramo theorem

A gamma-ray that interacts in a semiconductor will form electron-hole pairs. The electrons and holes formed will then drift in a direction that is dictated by the electric field. Holes will drift in the direction pointed to by the electric field line arrows, while electrons will drift in the opposite direction. The formation of a signal in a radiation detector will be caused by the change in the induced charge  $\Delta Q$  on one or more

of the electrodes. It is the motion, and not the actual collection, of the electrons and holes that will result in such a change in the induced charge. Hence, the signal generated within a radiation detector will be critically dependent on the transport of the charge carriers.

A simplification to the calculation of the induced charge due to the movement of a point charge was developed independently by Shockley and Ramo [42, 43]. This very useful tool is now known as the Shockley-Ramo theorem. The Shockley-Ramo theorem states that the charge induced on an electrode  $Q$  by the movement of a point charge  $q$  is given by

$$Q = -q\varphi_o \quad (2.1)$$

where  $\varphi_o$  is designated as the weighting potential. It then follows that the change in the induced charge will simply be given by

$$\Delta Q = -q\Delta\varphi_o \quad (2.2)$$

In a physical context, this theorem states that the change in the induced charge on an electrode is simply equal to  $q$  multiplied by the change in the weighting potential from the starting point to the ending point of the charge's path. The weighting potential is a position dependent function that is found by setting a fictitious set of boundary conditions to the electrodes on a detector. These boundary conditions are given as follows:

1. The electrode of interest, for which the weighting potential is to be calculated, is set to an electric potential of unity.
2. All other electrodes are set to an electric potential of 0.
3. Any space charge within the device is ignored.

Once these conditions are set, then the Laplace equation  $\nabla^2\varphi = 0$  is solved to determine the electric potential, and hence the weighting potential, within the device. The weighting potential does not give the true electric potential within the device, since that is determined by the actual potential applied to the detector as well as the space charge density. Instead, the weighting potential is simply a tool that provides a simplistic means in determining the induced charge on an electrode as governed by Equation 2.1. The path of the charge, however, is still affected by the true electric field within the device. Therefore, in order for one to know the charge induced on an electrode, one must still know the beginning and ending point of the charge's path, which can be determined based on the direction of the electric field lines.

The Shockley-Ramo theorem was originally developed for the conditions found in a vacuum tube, where the space charge density is 0. However, it was later proven that this theorem can also be applied to devices in which a stationary space charge is present [44,45]. The universality of the Shockley-Ramo theorem allows its application for a greater set of charge sensing devices, including semiconductor detectors. This theorem allows for a more simplified means for calculating the induced charge on an electrode for a wide variety of electrode geometries, since prior to this theorem many surface integrals had to be calculated to determine the induced charge at different locations along the electron trajectory. The utilization of the Shockley-Ramo theorem as it applies to single-polarity charge sensing devices was previously discussed in the literature and will be further examined in the following section [33].

## 2.2 Theory of single-polarity charge sensing

One of the simplest methods to measure the charge formed in a semiconductor radiation detector is by employing planar electrodes. In such a configuration, the



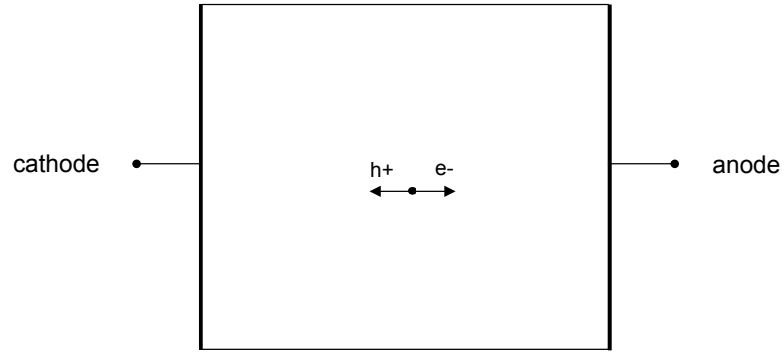
movement of both the positive and negative polarity charge produced in the active volume of the detector will contribute to the anode signal. This effect can be understood from Figure 2.1. Figure 2.1(a) illustrates the simple configuration of a planar detector and Figure 2.1(b) gives the weighting potential of the anode as a function of depth. The anode weighting potential is calculated by applying a potential of 1 to the anode and a potential of 0 to the cathode. It is then a simple matter of solving the Laplace equation with these boundary conditions to find that  $\varphi_o$  is a linearly increasing function. If we assume that 1 electron and 1 hole is formed in the device and each travel to their respective electrodes, then from Equation 2.2,  $\Delta Q$  will have both an electron and a hole component. The total  $\Delta Q$  is given by

$$\Delta Q = -q \cdot \Delta\varphi_o(\text{electron}) + q \cdot \Delta\varphi_o(\text{hole}) = -q(1 - Z) + q(-Z) = -q \quad (2.3)$$

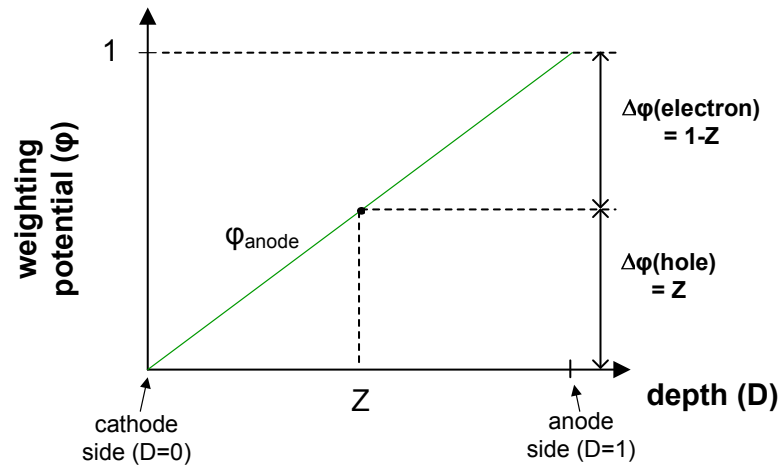
Hence, the total charge induced on the anode is simply the charge of the electron. In the planar configuration, this condition only holds when both the electron and hole get collected. In the case in which the hole is stationary and the electron gets collected by the anode, then  $\Delta Q = -q(1 - Z)$ . That is, the charge induced on the anode will only be a fraction (ranging from 0 - 1) of the electron's charge. Moreover,  $\Delta Q$  will be dependent upon at which depth the charge is formed. Therefore, one can imagine that for charge carriers generated uniformly in the device, this will then result in a distribution, from 0 to -q, of induced charge on the anode. This scenario will then lead to very poor spectroscopic performance. Two methods by which to circumvent this position dependency in the signal are shown in the following subsections.

### 2.2.1 Frisch grid

The method of single-polarity charge sensing was discussed in Section 1.3 as a means to mitigate the effects of poor ion transport in gas ionization detectors and



(a) Simple planar detector configuration.



(b) Anode weighting potential as a function of depth.

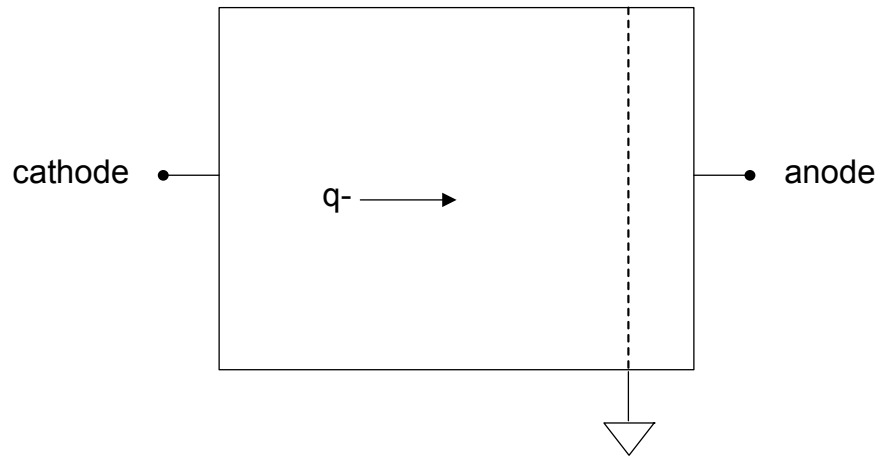
Figure 2.1: Figure showing that the final anode signal will be a combination of the electron and hole movement in the device.

poor hole transport in compound semiconductor detectors. One of the earliest applications of single-polarity charge sensing was achieved using the Frisch grid technique. A depiction of an ionization chamber employing a Frisch grid is shown in Figure 2.2(a). The Frisch grid is represented by the dotted line, which is placed close to the anode. Using the Shockley-Ramo theorem to calculate the weighting potential  $\varphi_o$  of the anode, the distribution of  $\varphi_o$  will have the functionality as depicted in Figure 2.2(b). This is because, when calculating the weighting potential of the anode, we apply a potential of 1 to the anode and a potential of 0 to both the cathode and the Frisch grid. Using the Laplace equation to solve for  $\varphi_o$ , we will find that  $\varphi_o$  is 0 everywhere between the cathode and the Frisch grid (the far-grid region) and then linearly rises to 1 in the area between the Frisch grid and the anode (the near-grid region). In order for charge to be induced on the anode, the electrons formed in the far-grid region must travel through the Frisch grid and enter the near-grid region. Hence, the biasing of the Frisch grid detector must be done in such a fashion that the electric field lines terminate on the anode. When the electrons travel the entire near-grid region and get collected by the anode,  $\Delta\varphi_o$  will be simply equal to 1. If  $n$  electrons travel from the far-grid region to the near-grid region and get collected by the anode, then  $\Delta Q$  is given by

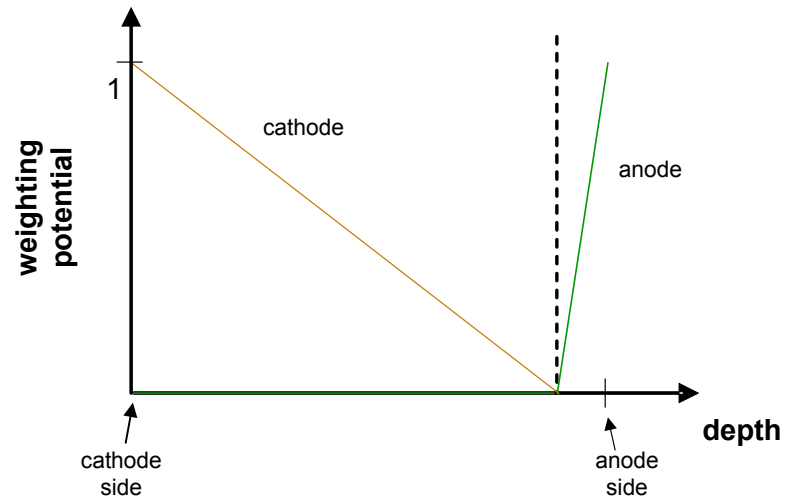
$$\Delta Q = -nq\Delta\varphi_o = ne_o \quad (2.4)$$

where  $e_o = -q$ . Therefore, the charge induced on the anode will be proportional to the number of electrons collected.

The Frisch grid is a very powerful technique to circumvent the effects of poor ion transport in ionization chambers. That is, the anode signal no longer has a position dependent component, in contrast to the planar case. According to Equation 2.4, the signal will always be proportional to the number of electrons collected by the anode.



(a) Frisch grid layout.



(b) Anode and cathode weighting potential as a function of depth.

Figure 2.2: Figure illustrating the Frisch grid as implemented in gas ionization chambers.

Therefore, the slow, or stationary movement, of the ions in the far-grid region will have no effect on the signal. Assuming that all of the electrons generated in the detector are collected, then we can obtain precise energy information of the gamma-ray interaction. Other factors, such as electronic noise, ion recombination, and electron trapping will act to create uncertainty in the energy information. However, through the single-polarity charge sensing technique, significantly better energy resolution can be achieved in ionization chambers than could be obtained otherwise.

### 2.2.2 Coplanar grid

In an analogous manner to the Frisch grid in gas ionization chambers, the coplanar grid is a method to achieve single polarity charge sensing in semiconductors. As discussed in Section 1.3, the coplanar grid was developed by Luke to address the complications that arise from poor hole mobility in CZT [22]. A cross-sectional view of the coplanar grid geometry is shown in Figure 2.3(a). On one face of the semiconductor is a planar cathode and on the other face are the coplanar anodes. The coplanar anodes consist of a collecting anode and a noncollecting anode. The collecting anode is biased slightly more positive than the noncollecting anode. Hence, as the electrons drift toward the anode structure, they preferentially drift toward the collecting anode. How exactly the coplanar anode can act as a single polarity charge sensing device can best be illustrated by examining the trend in weighting potential using Figure 2.3(b). Again, we use the Shockley-Ramo theorem to calculate the weighting potential for each of the electrodes. Like the Frisch grid detector, we can divide the detector into a far-grid and a near-grid region. The near-grid region is within 1 pitch  $P$  of the anode structure and the far-grid region is anything beyond this. By calculating the weighting potential along a line perpendicular to the collecting anode surface in the far-grid region, the collecting anode and noncol-

lecting anode both have the same linear rise in weighting potential with the same slope. Then, calculating along this same line, we find that the weighting potentials diverge in the near-grid region. The collecting anode sharply rises to 1 (where the boundary condition is set to 1), whereas the noncollecting anode sharply falls to 0 (where the boundary condition is set to 0). By subtracting the collecting anode and noncollecting anode signals, the effective weighting potential of the subtracted signal will be 0 in the far grid region and then will sharply rise to 1 in the near grid region. The effective weighting potential for the subtracted signal is shown in Figure 2.3(b) and this is very similar to the trend observed in Figure 2.2(b) for the Frisch grid case. Invoking the same argument as in Section 2.2.1, if  $n$  electrons travel from the far-grid region to the near-grid region, then the induced charge on the subtracted signal will be  $\Delta Q = ne_{\circ}$ .

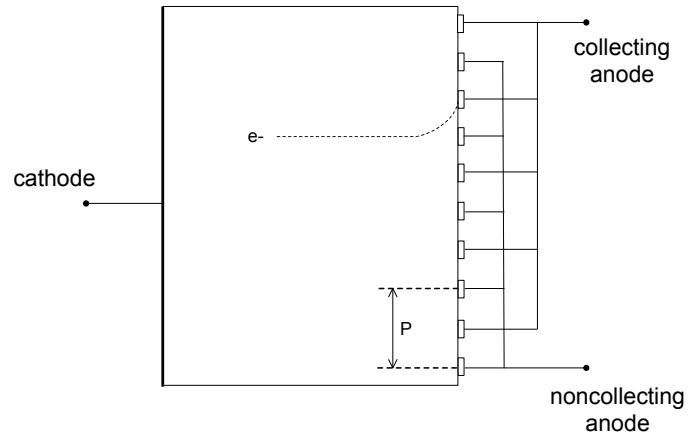
A more physical interpretation of the coplanar grid signal can be realized if we consider the symmetry of the grid structure. Suppose a gamma-ray interaction occurs somewhere in the middle of the device between the cathode and the anode, which constitutes the far-grid region. We can divide the signal into both an electron and a hole component. Considering only the electrons as they drift in the far-grid region toward the anode surface, the induced charge on both the collecting and noncollecting anodes will be the same. This is because the induced charge on a conducting surface due to a point charge is given by

$$Q = \int \sigma da$$

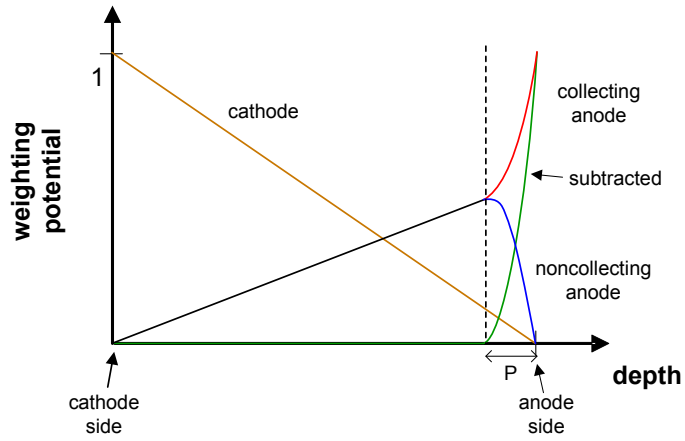
and

$$\sigma = -\epsilon_{\circ} \frac{\partial V}{\partial n}$$

where  $\sigma$  is the surface charge induced on a conductor [46]. The potential  $V$  due to



(a) The coplanar grid geometry.



(b) Weighting potential for each of the electrodes in the coplanar grid detector. The weighting potential functions are calculated for a line perpendicular to the collecting anode surface.

Figure 2.3: Figure illustrating the single polarity charge sensing concept as it is applied to coplanar grid electrodes.

the point charge will have a nearly equal distribution for both grids, because of the symmetric nature of the coplanar grid structure. Hence, the signal due to the drift of the electrons in the far-grid region will be the same for both of the coplanar grids. One can imagine that since the signals will be the same for both grids, if we take the difference between these signals, the resulting signal  $Q_{sub}$  will be 0. However, once the electrons enter the near-grid region, then the charge induced will no longer be equivalent. This is because the electrons will follow the electric field lines, which are almost entirely determined by the biasing conditions of the detector. Because of this, the electrons will be directed toward the collecting anode and away from the noncollecting anode. As the electrons move closer and closer to the collecting anode,  $V$  will continue to rise until the electrons are collected, at which point  $Q_{ca} = -nq$ , where  $Q_{ca}$  is the collecting anode signal. Conversely, as the electrons move further from the noncollecting anode,  $V$  will continue to fall until  $Q_{nca} = 0$ , where  $Q_{nca}$  is the noncollecting anode signal. Therefore, at the point of collection, the subtracted signal induced charge will always be  $Q_{sub} = -nq$ . Because  $Q_{sub}$  in the far-grid region is 0, it then follows that for electrons originating in the far-grid region and drifting to the collecting anode  $\Delta Q_{sub} = -nq$ . So far in this analysis we have only considered the movement of electrons. If we also consider the movement of holes in the far-grid region, it becomes apparent that their movement will also induce an equal amount of charge on both of the grid electrodes. Hence, the hole component to the subtracted signal will be 0.

### 2.3 Electron trapping compensation techniques

The method described in Section 2.2 is done to dramatically reduce the adverse effects of poor hole mobility in compound semiconductors, such as CZT. However,



another property of compound semiconductors that complicates matters is that of electron trapping. For instance, a typical value for the electron mobility-lifetime product  $\mu_e\tau_e$  in CZT is  $6 \times 10^{-3} \text{ cm}^2/\text{V}$  [47]. The percentage of electrons trapped after traveling a distance  $z$  can be found using Equation 2.5

$$N(z) = N_o \exp\left(-\frac{z}{\lambda_e}\right) \quad (2.5)$$

where  $N$  is the number of electrons and  $\lambda_e$  is the mean free drift distance of the electron as given by

$$\lambda_e = \mu_e\tau_e E$$

The ratio of  $N(z)/N_o$  gives the fraction of electrons remaining after traveling a distance of  $z$ , hence taking  $1 - N(z)/N_o$  will provide the fraction of electrons trapped. By assuming an electric field magnitude of 1600 V/cm and a detector thickness of 1 cm, the percentage of electrons trapped when traveling the full detector thickness is  $\sim 10\%$ . This means that a 10% shift in the photopeak position will occur depending on whether the event is a cathode-side or an anode-side event. Hence, in order to achieve energy resolutions around 2% at 662 keV, one must compensate for the effects of electron trapping. Two methods to achieve this are discussed as follows.

### 2.3.1 Relative gain method

One of the advantages of the coplanar grid structure, in contrast to the Frisch grid, is the ability to compensate for electron trapping. The first method that was proposed for electron trapping compensation of coplanar grid detectors is called the relative gain method, which was introduced by Luke [34]. In this technique, a gain factor  $G$  is applied to either the collecting anode signal or the noncollecting anode signal during signal subtraction. The formula which governs signal subtraction is

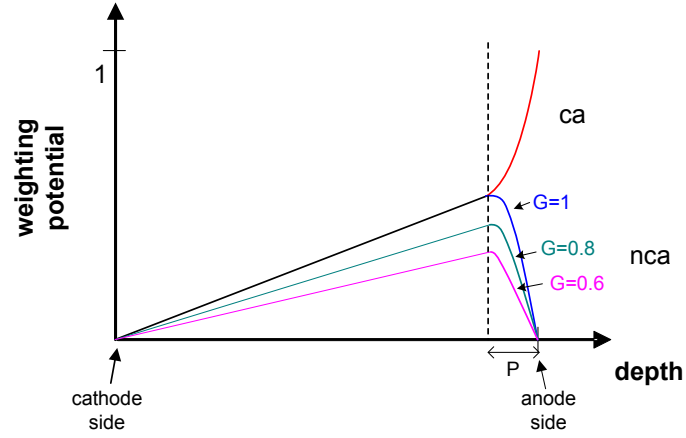
given by Equation 2.6

$$A_{sub} = A_{ca} - G \times A_{nca} \quad (2.6)$$

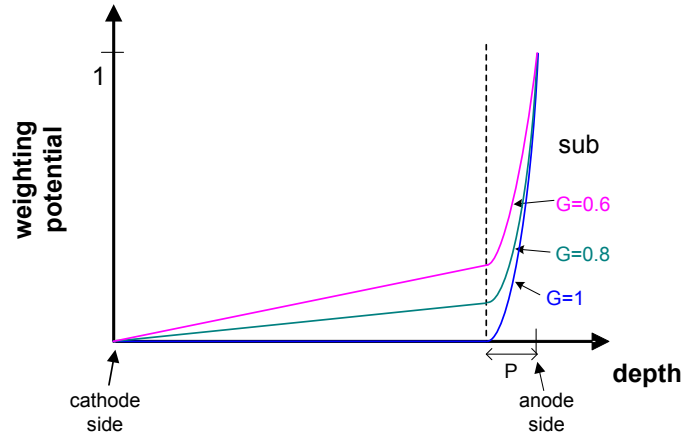
where  $A_{ca}$  and  $A_{nca}$  are the preamplifier signals of the collecting anode and noncollecting anode, respectively, and  $A_{sub}$  is the subtraction circuit signal. By adjusting the relative gain according to Equation 2.6, we are essentially altering the slope of the noncollecting anode weighting potential as depicted in Figure 2.4(a). Likewise, this will affect the subtracted signal weighting potential function as shown in Figure 2.4(b). The non-zero slope of the subtracted signal weighting potential in the far-grid region entails that electrons that originate further from the anode will have a greater weighting on the subtracted signal than events that occur closer to the anode. Figure 2.5 illustrates this effect. We find that  $\Delta\varphi_1 > \Delta\varphi_2$ . Hence, electrons that originate at  $z_1$  and get collected by the collecting anode will contribute a larger signal than electrons that originate at  $z_2$ . Due to charge trapping, we know from Equation 2.5 that the number of electrons collected will be greater for events originating at  $z_2$  than events originating at  $z_1$ . The two effects of weighting potential and charge trapping will act to offset one another, such that the charge induced will be nearly uniform at all detector depths. Therefore, by adjusting the relative gain to the optimal value, one can achieve a good, first order compensation for electron trapping.

### 2.3.2 Depth sensing method

Shortly after Luke's introduction to the relative gain method, He *et al.* proposed another method for electron trapping compensation [38]. This method is called the depth sensing method, because for every gamma-ray event, 1-D depth information can be obtained. Depth information can be acquired by calculating  $C/A_{sub}$  for each event, where  $C$  is the cathode signal. The cathode signal behaves identical to the



(a) The relative gain factored weighting potential for the collecting anode and noncollecting anode.



(b) The effective weighting potential of the subtracted signal.

Figure 2.4: This figure illustrates how the slope of the subtracted signal weighting potential in the far-grid region can be adjusted.

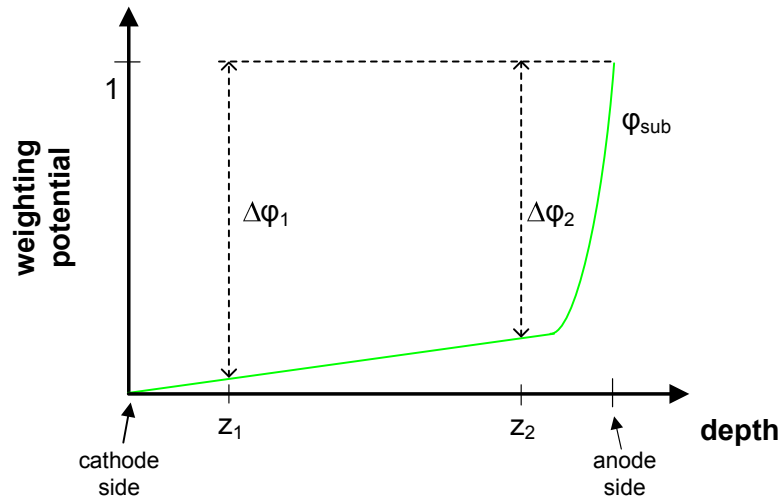


Figure 2.5: Subtraction circuit weighting potential with the relative gain set to some number less than 1. This figure depicts how the effect of electron trapping can be compensated.

planar electrode signal, which was discussed in Section 2.2. This is because the cathode weighting potential is a linear function of depth as shown in Figure 2.3(b). This means that the cathode signal will have a depth dependent component which can be approximately expressed as  $C \propto D \cdot E_\gamma$ , where  $D$  is the distance from the coplanar anodes and  $E_\gamma$  is the energy deposited by the incident gamma-ray. As discussed in Section 2.2.2, the subtracted signal will be equal to the number of electrons collected. This is assuming that the relative gain is set to 1 and the weighting potential is 0 from the cathode side up to one pitch from the anode side for all lateral positions. Hence, the subtracted signal can be closely expressed as  $A_{sub} \propto E_\gamma$ . It is then evident that by taking the ratio of the cathode and subtracted signals, the interaction depth  $d$  can be estimated by  $d = C/A_{sub} \propto D$ . In reality,  $D$  is not exactly equal to depth, because of electron trapping and nonuniform weighting potential effects. Instead,  $D$  is a monotonically increasing function of depth. However, taking  $C/A_{sub}$  still provides precise enough depth information to accurately compensate for electron trapping.

The depth resolution of the detector employing the depth sensing method can be found by applying error propagation to the formula  $d = C/A_{sub}$ . Calculating the variance of  $d$  and knowing that  $\text{FWHM} = 2.35\sigma$ , we will find that the  $\text{FWHM}(d)$  is given by Equation 2.7.

$$\text{FWHM}(d) = \sqrt{\left(\frac{\text{FWHM}(C)}{C}\right)^2 + \left(\frac{\text{FWHM}(A_{sub})}{A_{sub}}\right)^2} \cdot \left(\frac{C}{A_{sub}}\right) \quad (2.7)$$

This equation gives us a measure of the uncertainty of the measured depth from the true depth. For a 662 keV event, it has been estimated that the depth resolution for a 1 cm thick device on the cathode side is 0.1 mm and on the anode side is 0.06 mm [39]. This estimate is assuming that the gamma-ray interacts by way of photoelectric absorption. If multiple interactions occur, i.e. Compton scattering, then the depth resolution will be poorer since the calculated depth will actually be

the centroid of all the interaction locations.

## 2.4 Radial sensing

The ability to achieve 1-D position information, by way of depth sensing, in CZT radiation detectors was a breakthrough for improving, analyzing, and verifying detector performance. Another important discovery introduced by He *et al.* was that of radial sensing [40]. This sensing technique is critically dependent on the anode geometry. In 1998 He proposed using a boundary electrode surrounding the coplanar grid anodes to achieve a more symmetric weighting potential profile [40]. This concept will be expanded upon further in Chapter 3 of this dissertation. With the addition of the boundary electrode, we force the weighting potential of the collecting and noncollecting anodes to be 0 along the periphery on the anode surface. This creates a convex distribution in the weighting potential, in the lateral direction, for a fixed depth. This is shown in Figure 2.6. According to Equation 2.2, the induced charge on an electrode due to the movement of a single charge carrier is proportional to the difference of the weighting potential between the beginning and end positions of the charge's path. Since the weighting potential of the collecting anode is greater in the center  $W_{center}$  than it is along the periphery  $W_{edge}$  at a specific depth  $Z$ , and the weighting potential on the anode surface where the electrons are collected is 1, then the induced charge on the collecting anode  $A_{ca}$  will be larger for events starting near the periphery than for events starting near the center. This effect is illustrated in Figure 2.7. Using this information, we can obtain the relative radial position of an event using the following relationship

$$\left. \frac{A_{ca}}{A_{ca} - A_{nca}} \right|_{edge} > \left. \frac{A_{ca}}{A_{ca} - A_{nca}} \right|_{central} \quad (2.8)$$

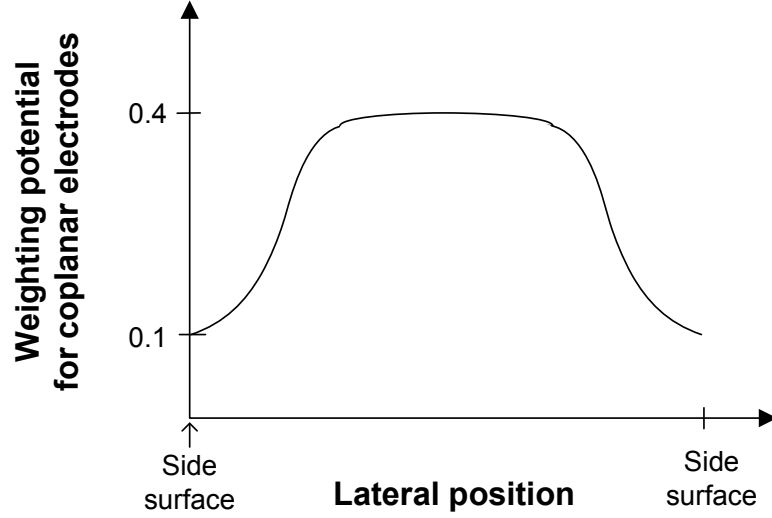


Figure 2.6: Weighting potential for either coplanar grid electrode along a line passing through the middle of the detector at a fixed depth near to, but greater than 1 pitch, from the anode. The convex shape is caused by the boundary electrode, where the weighting potential is forced to 0 at the anode surface.

where the subtracted signal  $A_{ca} - A_{nca}$  is taken with the relative gain set to 1. When the relative gain is set to 1, the weighting potential of the subtracted signal should be mostly independent of radial position. This technique allows us to obtain spectra as a function of radial position.

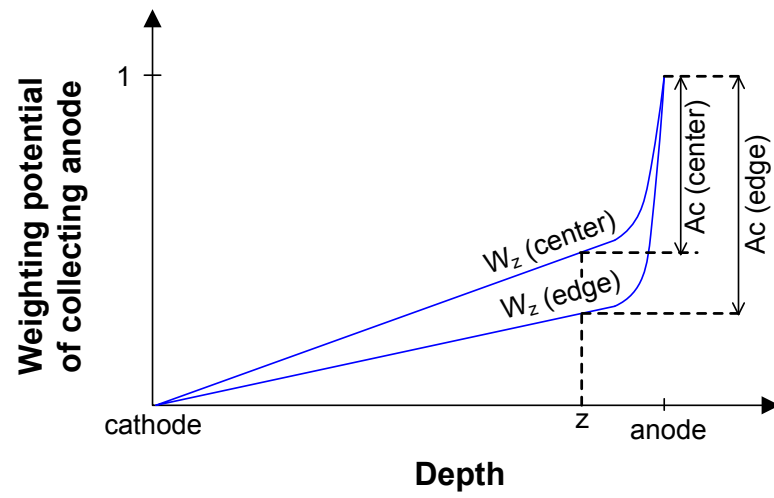


Figure 2.7: Induced charge of a single electron formed at depth  $Z$ , at two different radial positions, and traveling to the collecting anode.

## CHAPTER III

### Coplanar Grid Electrode Design and Experimental Arrangement

It has been shown that the coplanar grid design itself can have a significant effect on the overall energy resolution of the device [40]. This is due to the effect of a nonsymmetric weighting potential for the collecting and noncollecting anodes at a given depth in the detector. In the first-generation coplanar grid design, parallel electrode strips were connected together alternately to form two sets of coplanar electrodes as shown in Figure 3.1. If we calculate the weighting potential for coplanar anode 1, we set the potential of this anode to be 1 and the potential of the other anode to be 0. Hence, the weighting potential of coplanar anode 1 will be larger on the left side of the detector than on the right, because this anode occupies the periphery on the left side. Likewise, the weighting potential of coplanar anode 2 will be larger on the right side. It then follows that if we subtract the two signals, one side of the detector will have a positive weighting potential and the other side will have a negative one, because of the nonsymmetric weighting potentials for the two coplanar grids. This effect will give rise to a variation in the subtracted signal for the same gamma-ray interaction depth and the variation becomes more severe near the coplanar anodes. This is because the closer proximity of the coplanar anodes will lead to a greater variation in the nonsymmetric effect. Hence, using the generation



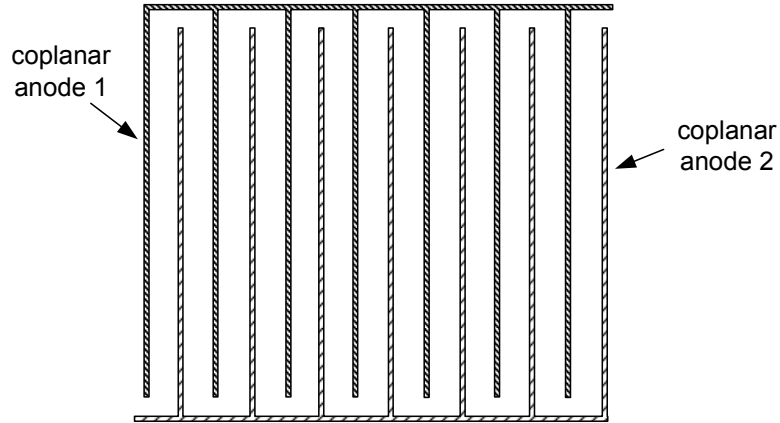


Figure 3.1: Generation 1 coplanar anode design.

1 coplanar grid design, He *et al.* observed significant energy resolution degradation near the coplanar anodes [38].

A method to combat the large nonsymmetric weighting potential effect observed with the generation 1 detector was proposed by He *et al.* [40]. This method employs a boundary electrode surrounding the two coplanar anodes and was labeled the generation 2 coplanar grid design. The purpose of the boundary electrode is to aid in balancing the weighting potentials for both coplanar anodes. This is because, if we calculate the weighting potential of either coplanar anode, 1 V is assigned to that anode and 0 V is assigned to all other electrodes, including the boundary electrode. When the boundary electrode is excluded, the boundary conditions force an imbalance in the potential near the periphery of the anode surface, because the most outside strip electrode will have either a 1 or 0 weighting potential, but not both. With the addition of the boundary electrode, the potential is fixed to 0 along the periphery of the anode surface, making it possible to balance the weighting potentials of the two central coplanar anodes. Therefore, the weighting potential of the subtracted signal will not have as much variation along the edge of the detector as in the generation 1 design. He *et al.* [40] observed significant improvement in the detector

performance near the anode surface with the use of the boundary electrode. However, there was still room for further improvement, which gave way to the generation 3 design.

An additional advantage of the boundary electrode is that it generally allows for higher detector biasing. This is because the boundary electrode aids in absorbing leakage current from the sides of the detector. Without the addition of the boundary electrode, it is thought that this leakage current would contribute to the noise in the subtracted signal. Hence, by employing the boundary electrode, it is believed that a higher cathode bias can be applied since the side surface leakage current should be absorbed and not contribute to the total noise. A higher cathode bias will result in better charge collection efficiency, which generally leads to better detector performance.

### 3.1 Third-generation coplanar anode design concept

The third-generation coplanar anode design was proposed by He *et al.* [40] to improve the weighting potential uniformity of the subtracted coplanar grid signal. When the weighting potentials of the coplanar anodes are insufficiently balanced, events occurring near the anode will result in degraded energy resolution. To circumvent this problem, the generation 3 design was introduced and an illustration of the design is shown in Figure 3.2. As with the generation 2 detector, this anode geometry involves a coplanar anode grid structure surrounded by a boundary electrode. The generation 3 design was improved from the generation 2 design by changing the widths of the two outermost strips and three outermost gaps. The basis behind this change was the effect of the weighting potential around the perimeter of the detector being dominated by the outermost anode strip. By reducing the width

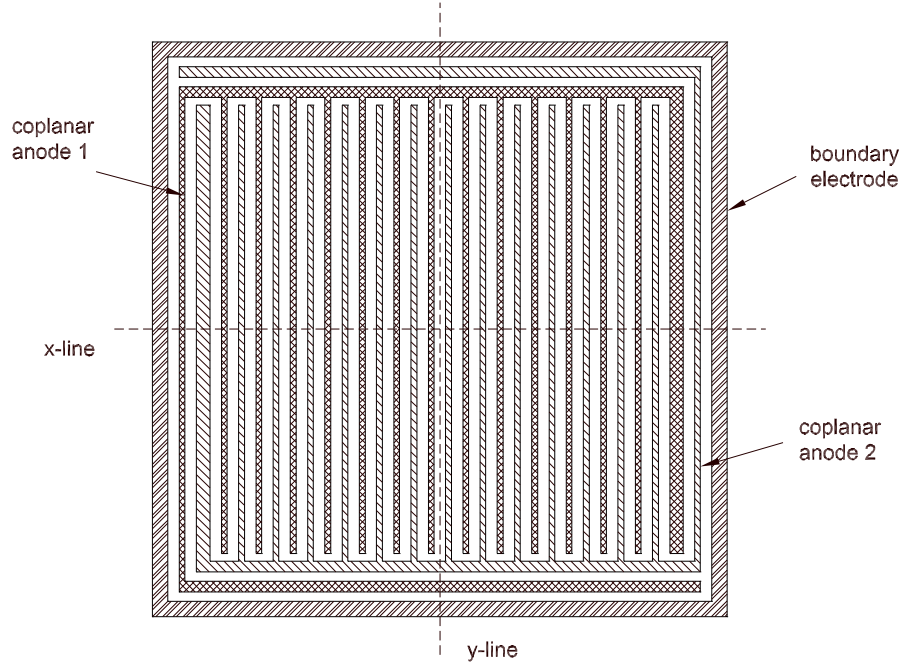


Figure 3.2: Generation 3 coplanar grid design consisting of two coplanar anodes and a boundary electrode. This design is  $15 \times 15 \text{ mm}^2$  in area.

of the outermost strip and increasing the width of the second outermost strip, a much more balanced weighting potential profile can result.

### 3.2 Electrostatic simulations

The design of the coplanar grid electrodes was carried out using the three-dimensional electrostatic finite-element analysis software package Maxwell [48]. This package can easily simulate the weighting potential field for any electrode of interest. Because our goal is to achieve uniform response independent of the  $\gamma$ -ray interaction location, we sought to minimize the difference of the weighting potentials for the coplanar anodes. As a means of comparing design simulations, we used the following figure of merit (FOM) value

$$\text{FOM} = |W1 - W2| \quad (3.1)$$

where  $W1$  and  $W2$  are the weighting potentials for either coplanar grid anode at some specified point within the simulation mesh. The FOM value was calculated along a plane 1.5 mm from the anode surface. This calculation was done close to the anodes, because the weighting potential nonuniformity is always the most severe near the grids. Hence, by minimizing the FOM near the grids, we can be certain that this value is even less for planes beyond 1.5 mm from the anode surface. Smaller FOM values indicate better weighting potential uniformity.

In addition to the weighting potential symmetry, it is also very important to keep in mind the effects of detector capacitance, which is an important factor in the amount of electronic noise observed in the system. Using Maxwell, we can easily calculate the capacitance by using the well known equation  $C = \Delta Q / \Delta V$ . If we want to calculate the capacitance of just the coplanar grids, we set the collecting anode potential to unity and the other electrodes to zero. Then we calculate the induced charge  $\Delta Q$  on the noncollecting anode using Gauss's law

$$\Delta Q = \oint_{surf} D \cdot ds \quad (3.2)$$

where  $D$  is the electric displacement vector. After determining  $\Delta Q$ , it is a simple matter to calculate  $C$ . These calculations were done for the inter-grid capacitance, since this will be the dominate form of capacitance for the coplanar grid detector. However, to determine the total capacitance of the detector, we can carry out the same calculation for the boundary electrode and the cathode and add each component together in parallel.

So, a balance between the detector capacitance and the FOM value must be met in order to achieve the optimal detector performance. We adapted our design from a previous detector design having a strip width of 150  $\mu\text{m}$  and a gap width of 300  $\mu\text{m}$  in the central region of the electrode surface. We then made adjustments to

Table 3.1: Figure of merit (FOM) and capacitance data calculated by way of simulation.

Configuration name	FOM	Capacitance (pF)
cgrev3a	0.0165	-
cgrev4a	0.0139	-
cgrev5a2	0.0135	11.8993
cgrev7a2	0.0133	11.9033
cgrev8a	0.0136	11.5491

the outermost gaps and strips and simulated a variety of different designs to achieve what we believed to be nearly an optimal balance between the FOM and capacitance. Table 3.1 shows the simulated values for a few different design iterations. Design “cgrev7a2” was selected as the final design for detector fabrication, because the smallest FOM value was achieved for this design without sacrificing a significant increase in capacitance. Figure 3.3 gives the weighting potential for the selected design at 1.5 mm from the anode surface along the x and y-lines as indicated in Figure 3.2.

### 3.3 Sensing methods to verify improved electrode design

The depth sensing method described in 2.3.2 is a very useful tool to not only achieve higher quality spectra, but to also better understand detector behavior. Using this method, we can record spectra as a function of interaction depth. This information can then be used to verify the improvement in the coplanar grid design. This is because the coplanar grid weighting potential suffers more severe nonuniformity near the grids. Hence, if we don’t consider the effects of charge trapping, events that occur near to the coplanar anodes will generally result in greater variations in the induced charge. This variation will cause the FWHM to be larger for smaller depth indices (closer to the anode side). By employing the depth sensing technique, we can observe whether the energy resolution degrades near the coplanar anodes.

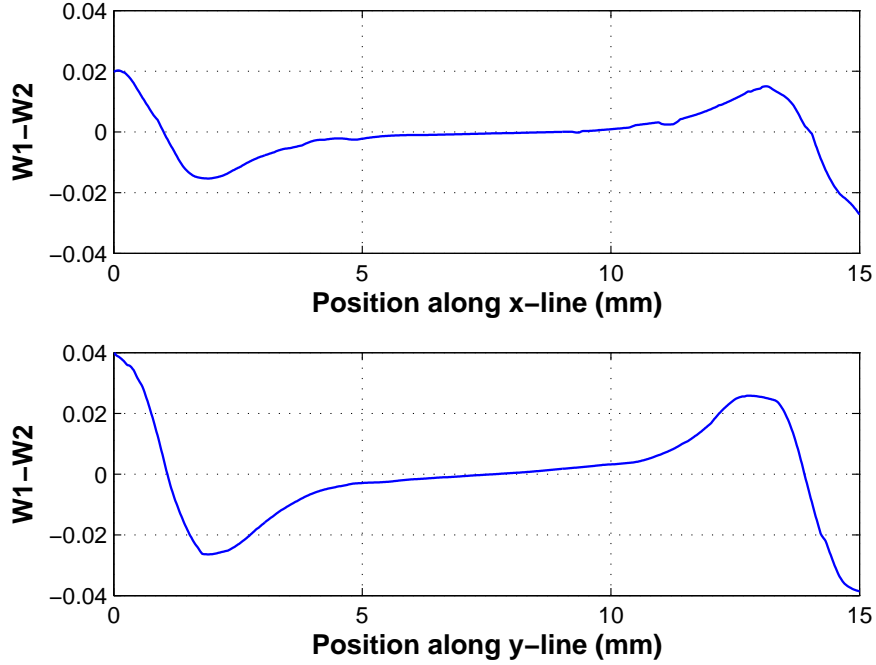


Figure 3.3: Weighting potential for the selected generation 3 design as a function of position at a distance of 1.5 mm from the anode surface. The two figures show the weighting potential along the x-line (top) and along the y-line (bottom) as indicated in Figure 3.2.

This information will provide a good indication of the weighting potential uniformity. Therefore, depth sensing allows us to analyze the improvement in the coplanar grid design. Results and a further discussion will be given in Section 4.1.3.

In Section 2.4 the radial sensing technique was introduced. This sensing method is another useful tool that can be used to diagnose the effectiveness of the coplanar grid design. The radial sensing method allows us to obtain spectra as a function of radial position. This is useful, because the weighting potential nonuniformity will always be most severe along the periphery of the detector. Thus, electrons that originate along the edges of the detector will lead to greater variations in the induced charge than those that originate in the center. This effect can be well understood from Figure 3.3 since the deviation from zero of the subtracted weighting potential is more significant along the edges of the device than in the center ( $x$  or  $y = 7.5$  mm). The degree of this

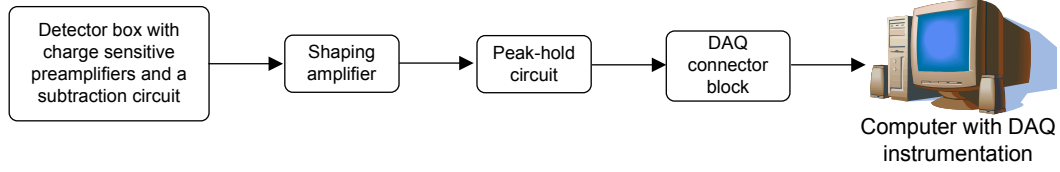


Figure 3.4: Block diagram representing the signal chain employed for coplanar grid CZT.

deviation will cause greater variation in the induced charge. By observing the spectra for different radial positions at a specific depth in the detector, we can observe how significant the performance of the detector is affected for increasing radial positions. This sensing method provides a means of comparison for different detector designs, since better coplanar grid designs should have less degradation in the spectroscopic performance for increasing radial positions. Measurement results using the radial sensing method will be discussed and analyzed in Section 4.2.

### 3.4 Readout hardware

Signals from the coplanar grid CZT detector are very small charge signals, which may correspond to the collection of a few hundred thousand electrons. For instance, for a 662 keV gamma-ray that is fully absorbed by the detector, the total charge collected at the anode will correspond to  $1.41 \times 10^5$  electrons, assuming no charge trapping. For this scenario, if the charge originates in the far-grid region, then  $\Delta Q_{sub}$  will be  $2.26 \times 10^{-14}$  C. Hence, in order to process such small charge signals, very precise readout electronics are necessary to be able to maximize the signal to noise ratio. A block diagram illustrating the signal chain is given in Figure 3.4.

The first stage in the signal chain is the preamplifier and subtraction circuit. The preamplifier used is the Amptek A250, which is a standard off-the-shelf charge sensitive preamplifier commonly employed with semiconductor detectors. For most of the experiments, three preamplifiers were used. One for the cathode signal, another

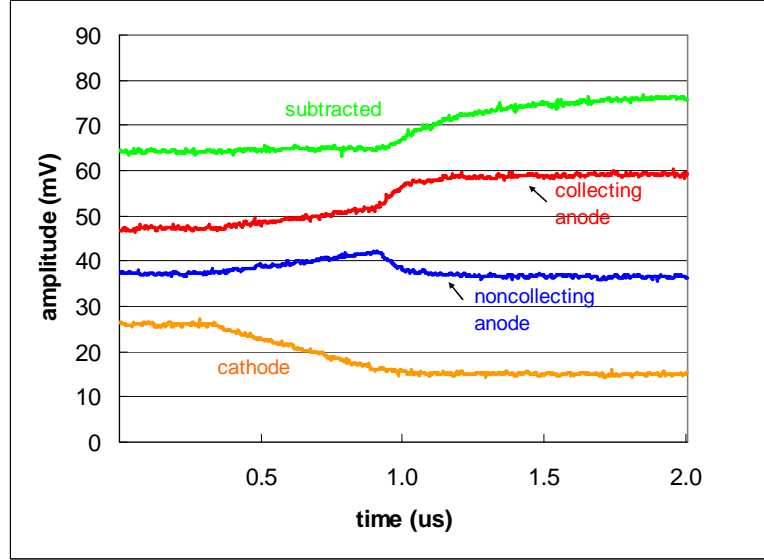


Figure 3.5: Plot of a typical pulse waveform after the preamplifier stage for the collecting anode, noncollecting anode, and cathode. The signal from the subtraction circuit is also shown.

for the collecting anode signal, and the final one for the noncollecting anode signal. The collecting and noncollecting anode preamplifier output signals were sent to a variable gain subtraction circuit, which was a custom built circuit as described in [38]. Typical coplanar grid signals, including those after the subtraction circuit stage, are shown in Figure 3.5. All of these components, along with the detector itself, are housed in an aluminum box in order to shield the detector from most external sources of electromagnetic interference. A picture of the actual detector box is shown in Figure 3.6.

To be able to achieve depth sensing, the cathode and subtracted signals must be amplified and shaped. Then, the peak value of this shaped signal must be determined. The shaping is done with standard NIM instrumentation, either the Ortec 572A or the Canberra 2026 shaping amplifiers. The unipolar output is selected, since it was determined that this provided adequate enough noise rejection. The shaped Gaussian signal is then sent to a custom built 4-channel peak-hold circuit. This circuit accepts the shaped signal as its input and then once the input exceeds a certain threshold



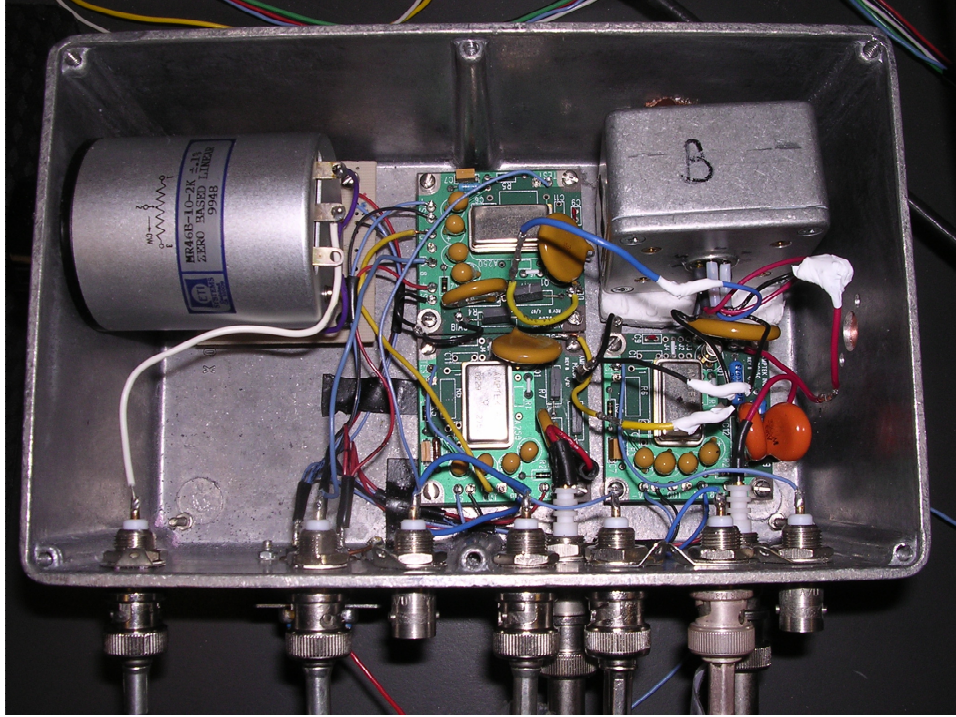


Figure 3.6: Picture of the detector box including the detector, 3 preamplifiers, and a subtraction circuit.

voltage which can be adjusted, the peak value is held. The hold time is an adjustable value, which is typically set to about  $20 \mu\text{s}$ . In addition to the analog signal, the peak-hold circuit provides a digital trigger signal, which indicates to the data acquisition (DAQ) card when to acquire a sample. A graph illustrating the signal train for the peak-hold circuit is given in Figure 3.7. A picture of the circuit itself is shown in Figure 3.8. The analog peak-hold signal and the digital trigger signal are then sent to the National Instruments SCB-68 I/O Connector Block. This device provides an interface between the peak-hold circuit and the DAQ card. The DAQ device used is the National Instruments PCI-6110 4 analog input DAQ card with 12-bit ADC precision [49].

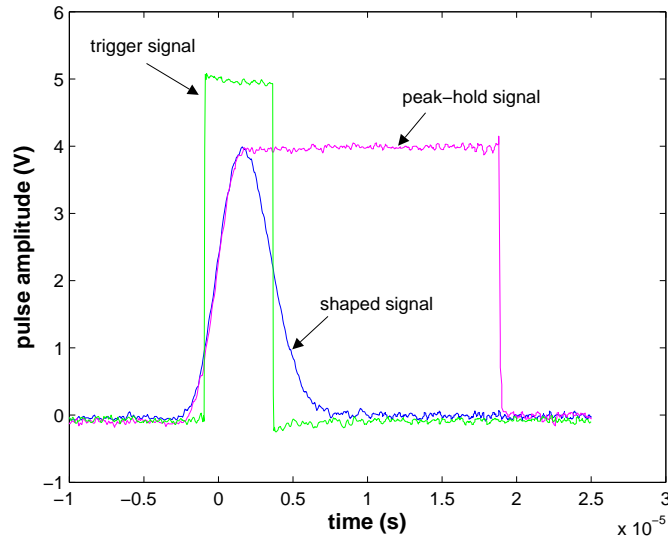


Figure 3.7: Peak-hold circuit pulse waveforms. The DAQ card is set to acquire a sample on the downward slope of the trigger signal.

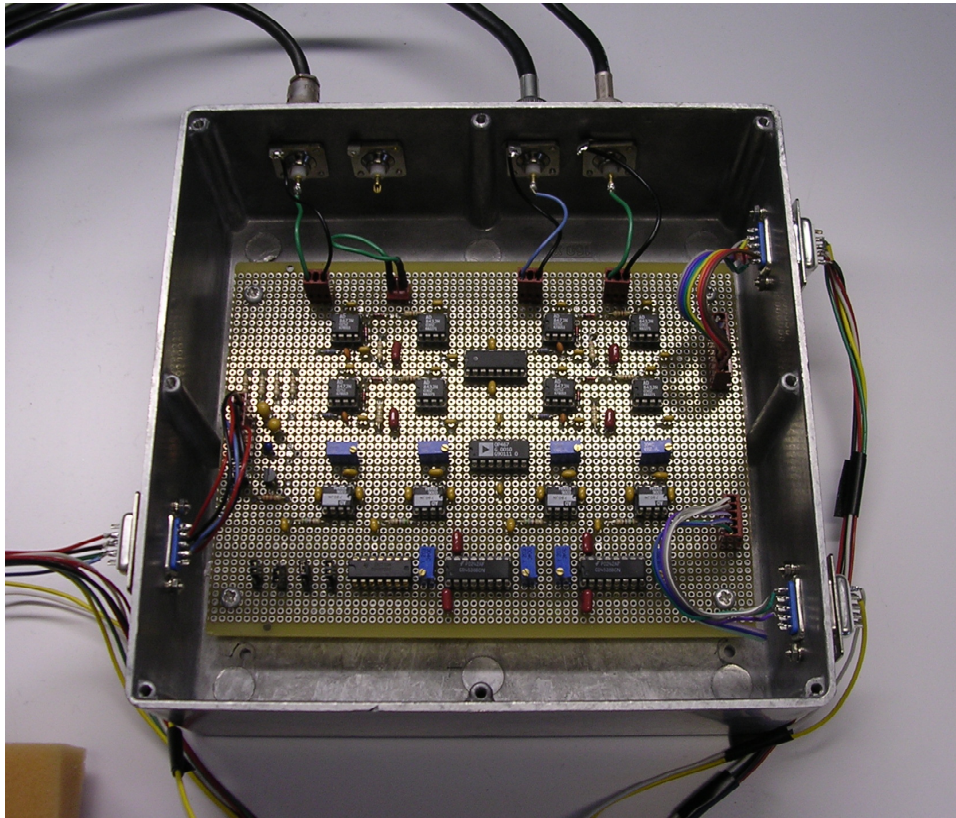


Figure 3.8: Picture of the 4-channel peak hold circuit.

### 3.5 Readout software

Data collection was done using LabVIEW [49], which is a program specifically designed to communicate with NI DAQ devices. Using this programming environment, a virtual instrument (VI) was written to acquire and process the signals sent to the DAQ card. The main duty of this program is to read in signals from the peak-hold circuit and to bin the data according to the depth of the gamma-ray interaction. Depth information is determined using the method described in Section 2.3.2. Here, the interaction depth  $d$  is calculated for every event resulting in a number from 0 to 1. 0 corresponds to an anode side event and 1 to a cathode side event. In the program,  $d$  is multiplied by a value corresponding to the number of depth indices. This number is equivalent to the number of depth divisions (typically 20-30). The calculated depth numbers are then rounded, such that each integer value corresponds to a specific slice within the detector. The depth spectrum is then saved so that it can be analyzed off line, after the data has been collected. In addition to determining the depth, the program also has the capability to bin the data as a function of radial position for a specific depth index. Therefore, using this method we can also obtain the radial spectrum. In order for depth and radial sensing to be achieved, 4 signals must be read in. This includes 3 analog signals corresponding to the subtracted, cathode, and collecting anode signal and 1 digital signal corresponding to the trigger signal. The trigger signal indicates to the DAQ card when in time to acquire a sample.

Once data collection is complete, a set of functions written in MATLAB were employed for data postprocessing. These functions read in the depth spectrum data, saved in LabVIEW, and output the depth corrected spectrum. The depth corrected

spectrum is generated by calculating the peak centroid for each of the depth spectra. Once the peak centroid is determined, an appropriate gain value is applied to each of the depth spectra such that all of the peaks align to the same channel number. Then, the spectrum is simply summed up, resulting in the depth corrected spectrum. This process acts to compensate for the effects of electron trapping. After the depth corrected spectrum is generated, one of the MATLAB functions is employed to calculate the FWHM for the depth corrected spectrum as well as for each of the individual depth spectra. The importance of the FWHM data will be made evident in Chapter IV.

## CHAPTER IV

### Experimental Results for Coplanar Grid Detectors

The emphasis of this dissertation work has been focused on the characterization and understanding of coplanar grid CZT detectors through experimental techniques. The focus of this chapter is to report the experimental results that were observed from these detectors and to provide explanations for these results. Two sets of detectors were fabricated and tested. One set, consisting of 3 different detectors, was fabricated by eV Products using crystals grown in house [50]. The other set, consisting of 2 different detectors, was constructed using crystals grown by Yinnel Tech, Inc., and fabricated into detectors by Baltic Scientific Instruments, Ltd., (BSI) [51, 52]. Both sets of detectors were made employing the generation 3 coplanar grid electrode design concept.

#### 4.1 eV Products detector results

A total of three detectors were ordered from eV Products [50]. Two of these were parallelepipeds with dimensions  $1.5 \times 1.5 \times 1.0 \text{ cm}^3$  and consisting of a square electrode design similar to that shown in Figure 3.2 except with slightly different anode geometry. These two detectors were designated as MO2 2-2 square and MO2 2-3 square. The other detector was cylindrical in shape 1.5 cm in diameter and 1.0 cm in length. This detector was designated as MO2 2-2 cylindrical and consisted of

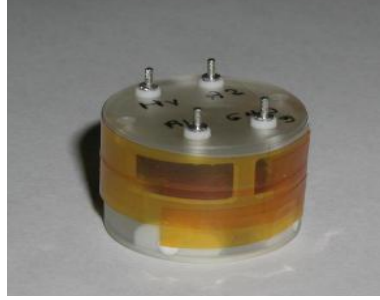


Figure 4.1: Picture of the eV Products detector. The detector itself is housed inside of the yellow protective package.

a circular electrode design with electrodes in the shape of a concentric helix. The cylindrical design was tested to determine if the circular shape of the electrodes could help to mitigate edge effects, such as those observed at corners, that would be present on the square design. A picture of one of these detectors is shown in Figure 4.1.

#### 4.1.1 Methods of operation

Coplanar grid detectors with boundary electrodes can be operated in two modes. When the noncollecting anode and the boundary electrode are biased at the same potential, lower than that of the collecting anode, electrons generated in the whole detector volume will be collected by the collecting anode. Alternatively, the collecting anode can be biased to the same potential as the boundary electrode, while the noncollecting anode is set to a lower potential. This results in the collection of electrons by the boundary electrode when charges are generated near the sides of the detector. Only electrons generated in the central region of the device can be collected by the collecting anode. This effect is illustrated in Figure 4.2. The loss in detection efficiency as a function of the biasing conditions was discussed by Pérez *et al.* [53]. For the generation 3 design discussed in Section 3.1, the loss in detection efficiency is  $\sim 15\%$  when only the central region of the detector is active.

The biasing condition illustrated in Figure 4.2(b) results in electrons being col-

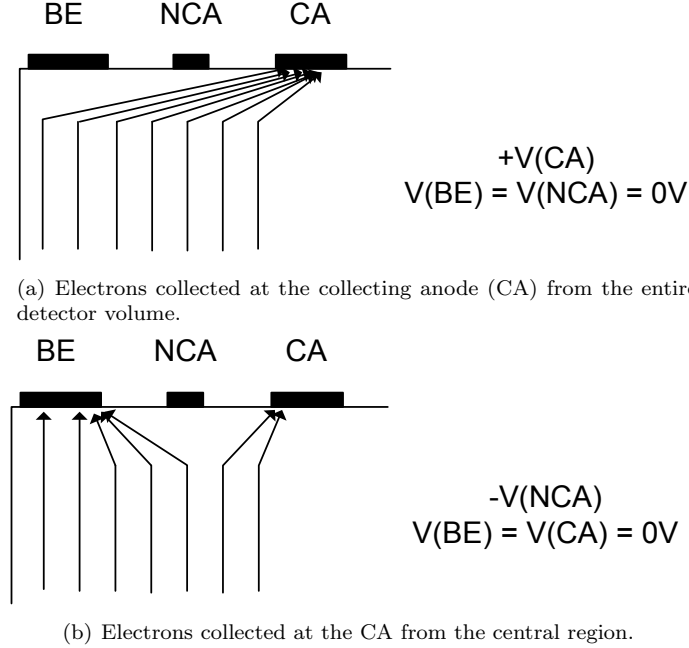
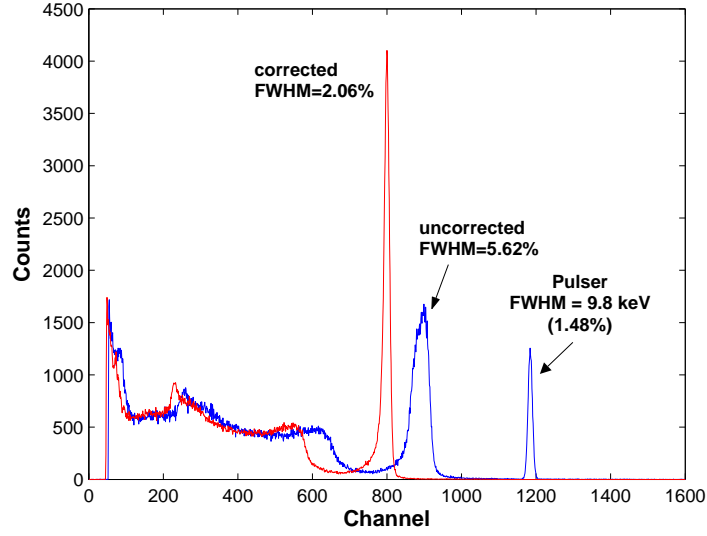
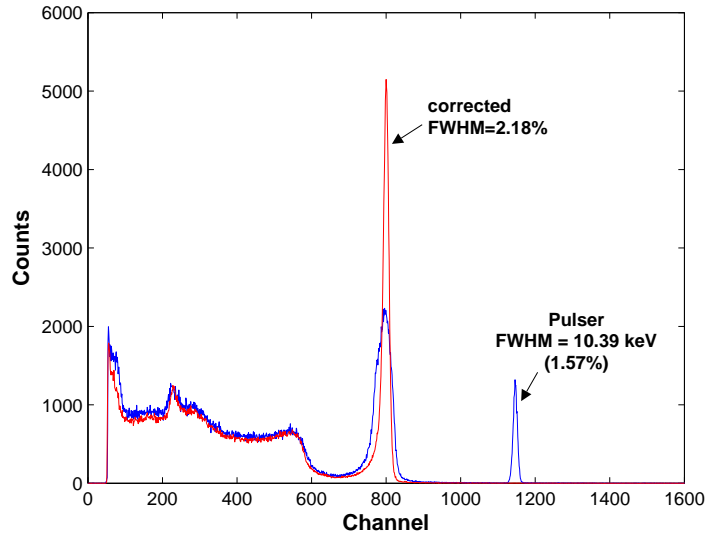


Figure 4.2: Figure illustrating the three outermost electrodes and how the collection of the electrons is affected by the detector biasing conditions.

lected from the central region of the detector. We observed from Figure 3.2 that the central region of the detector is where the difference of the weighting potentials of coplanar anodes is minimum. Hence, electrons originating from this region will give rise to less variation in the induced charge, because the difference in the weighting potential  $\Delta\varphi_o$  will be closer to 1. Therefore, the detector performance is expected to be better in this mode of operation, since charge induction will be more uniform than in the mode illustrated in Figure 4.2(a). Depth sensing results obtained using one of the eV Products detectors under these two modes of operation are illustrated in Figure 4.3. Our experimental results show a typical degradation of about 0.2% FWHM when the full detection volume is active to radiation, indicating that the detector performance is worse near the periphery of the devices.



(a) Spectrum is taken with the cathode set to -1700 V, the noncollecting anode set to -80 V, and the collecting anode and boundary electrode are set both to ground.



(b) Taken with the cathode set to -1600 V, the collecting anode set to +80 V, and the noncollecting anode and boundary electrode both set to ground.

Figure 4.3: Cs-137 spectrum obtained using an eV Products MO2 2-2 square detector utilizing the depth sensing method. Condition (a) results in only the electrons generated in the central region being collected by the coplanar anodes, whereas, in (b) electrons generated in the whole device are collected by the coplanar anodes.



#### 4.1.2 Spectroscopic performance

Employing the depth sensing method, energy resolutions between 2.0% and 2.1% FWHM at 662 keV for the MO2 2-2 square detector were consistently achieved [54]. A spectrum for this detector was shown previously in Figure 4.3(a). The performance for the other two detectors was not as notable. Using the MO2 2-3 square detector, an energy resolution of  $\sim 2.4\%$  was achieved, whereas the MO2 2-2 cylindrical detector resulted in an energy resolution of  $\sim 2.5\%$ . Despite having much fewer sharp corners, the helical design employed in the later detector did not result in better spectroscopic performance.

Spectra were also acquired using the relative gain method for electron trapping compensation. The optimal relative gain value was determined by tweaking the potentiometer of the subtraction circuit until the spectra with the best energy resolution was observed. Any offsets from the optimal relative gain value will result in poorer spectroscopic performance. Employing this method for the MO2 2-2 square detector, an energy resolution of 2.23% FWHM at 662 keV was achieved, which is shown in Figure 4.4.

The poorer performance observed using the relative gain method, in comparison to the depth sensing method, agrees with theoretical predictions. For one, the depth sensing method allows us to obtain depth information for each gamma-ray event. Hence, electron trapping compensation can be achieved independently for each detector depth. This allows us to compensate for electron trapping occurring for any depth dependent function. In contrast, the relative gain method can only apply a linear compensation as a function of depth, which means it is a more restrictive method. Second, the relative gain method will not produce optimal performance when using a boundary electrode [55]. This is because the boundary electrode affects the weight-

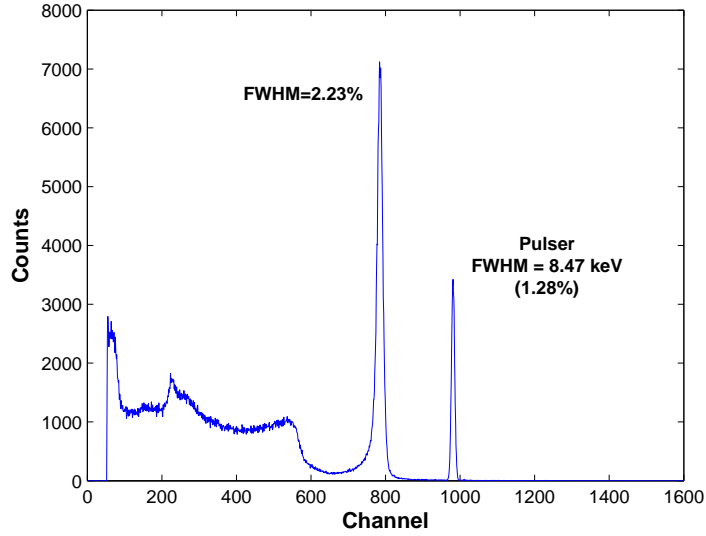


Figure 4.4: eV Products M02 2-2 square detector spectrum of a Cs-137 source obtained using the relative gain method for electron trapping compensation. This spectrum was taken with a cathode bias of -1700 V and anode bias of -80 V.

ing potential of both the collecting and noncollecting anodes resulting in reduced weighting potential along the edges of the detector. This can be seen in Figure 2.6. Because the weighting potential varies laterally across the detector at a particular depth, the optimal relative gain to properly compensate for electron trapping will also vary laterally. Since only one gain factor  $G$  can be set, there will be regions in the detector where the charge induced deviates from this optimum value in order to properly compensate for electron trapping.

#### 4.1.3 Validation of improved electrode design

To verify the improvement of the anode design, pulse height spectra as a function of depth were obtained on two detectors, one using the eV Products generation 2 design [53], where all strips and gaps had constant widths, and the other using UM's generation 3 design. Figure 4.5(a) shows the spectrum obtained at each depth for the generation 2 design. We observe that the photopeak resolution is best near the cathode side of the detector and worse near the coplanar anode side. This

phenomenon is the result of the weighting potential nonsymmetry rather than charge trapping, because the effect of charge trapping should be most severe towards the cathode side. Figure 4.5(b) shows the same measurement using the detector with the generation 3 design. In contrast, the spectra show better resolution near the coplanar anodes. A direct comparison of energy resolution as a function of interaction depth for the two different electrode designs is illustrated in Figure 4.5(c). The effects of weighting potential asymmetry observed on the generation 2 detector were reduced on the generation 3 detector to the point where the best resolution obtained was very near to the coplanar grid anode. The fact that the generation 3 design showed no degradation near the coplanar anodes supports our postulate that the new design is superior [54].

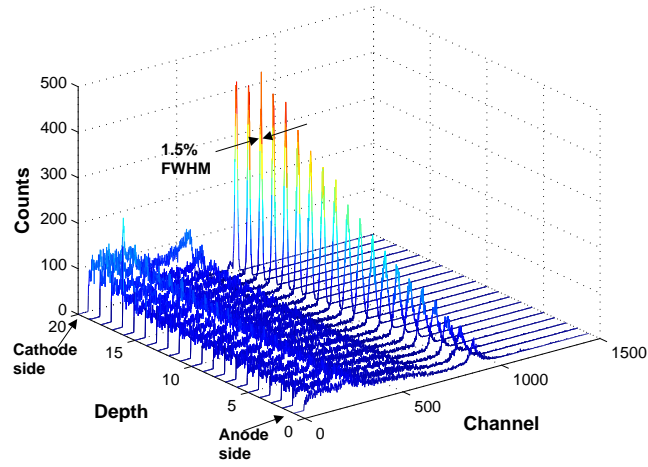
## 4.2 Measurement results using radial sensing

Results using radial sensing for three detectors with different anode designs are shown in Figure 4.6. The spectra shown in these figures are taken at different radial positions at about the same interaction depth, near the coplanar anodes. These spectra indicate the charge induction uniformity for electrons formed at different radial positions within the detector.

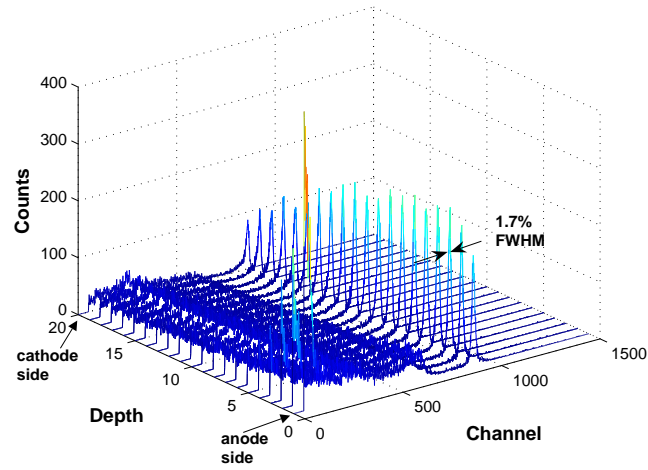
### 4.2.1 Second-generation design

The spectra obtained in Figure 4.6(a) confirm the severity of the non-symmetric weighting potential in the generation 2 design. These results show that the deviation of the photopeak centroid position from that of the center region of the detector increases with increasing radial position. The amount of deviation in the photopeak position is  $\sim 5 - 6\%$ .

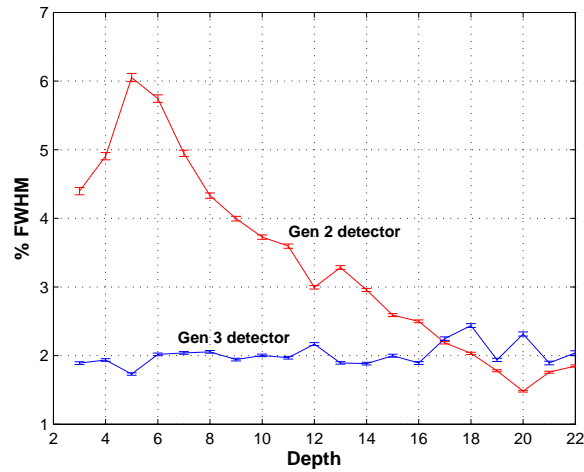
It is also clear from Figure 4.6(a) that multiple peaks were observed for spectra



(a)



(b)



(c)

Figure 4.5: Energy spectra at each depth using a Cs-137  $\gamma$ -ray source for (a) the eV Products generation 2 detector and (b) the generation 3 detector, both spectra were taken with a cathode bias of -1700 V and anode bias of -80 V. The plot in (c) shows the energy resolution (% FWHM) as a function of the interaction depth for both electrode configurations.

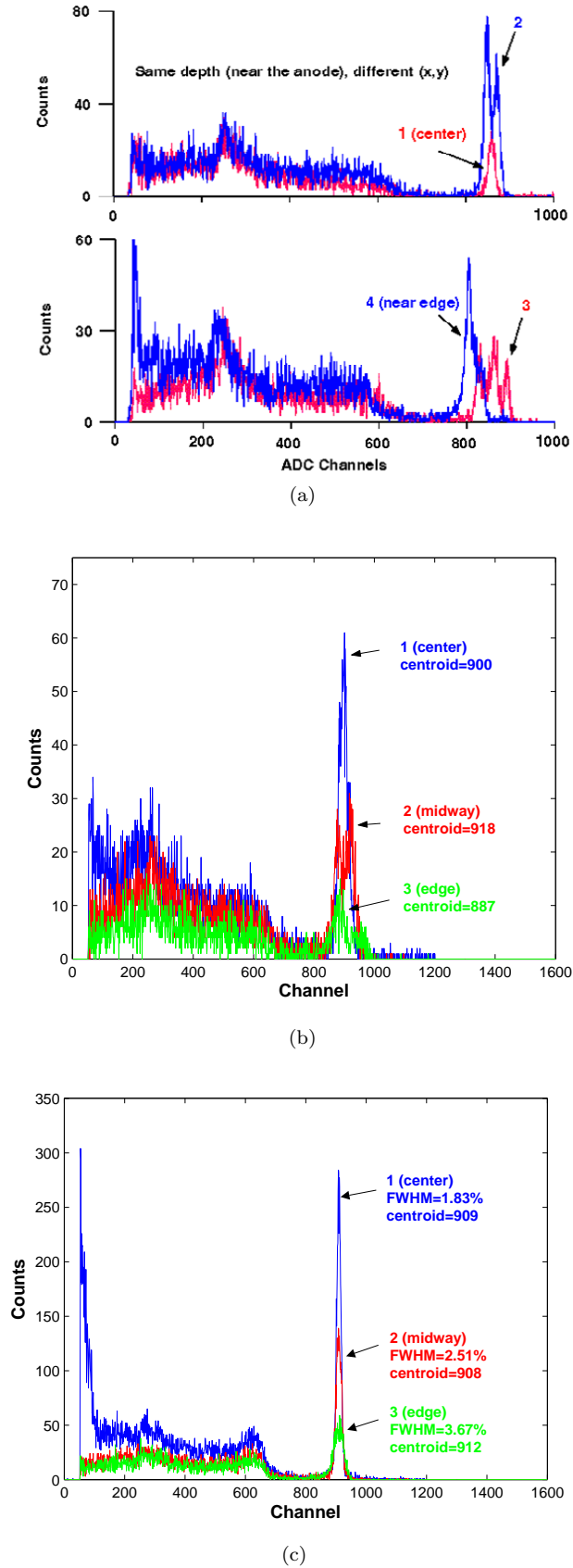


Figure 4.6: Cs-137 spectra taken at different radial positions at one particular interaction depth for (a) the generation 2 detector, where spectra numbers 1-4 indicate increasing radial positions (b) the I9-01 detector with eV's generation 2 design and (c) the MO2 2-2 square detector with the generation 3 design, where both (b) and (c) were taken with a cathode bias of -1700 V and anode bias of -80 V. In (b) and (c), numbers 1  $\rightarrow$  2  $\rightarrow$  3 indicated increasing radial positions.

2 and 3. To better understand why this was observed, we can study the plot of the coplanar grid weighting potentials for the generation 2 design in Figure 4.7. For the generation 2 design, the weighting potential of the collecting anode  $W_{ca}$  is higher than that of the noncollecting anode  $W_{nca}$ , on the left hand side. This is because the collecting anode is the outermost anode strip on the left hand side. Therefore, the weighting potential of the subtracted signal ( $W_{ca} - W_{nca}$ ) is greater than 0. This causes the induced subtracted signal to be smaller than for those events produced in the central region, where the weighting potential is  $\sim 0$ . Conversely, on the right hand side, the weighting potential of the collecting anode is lower than that of the noncollecting anode. Hence, the weighting potential of the subtracted signal is less than 0, causing the induced subtracted signal to be larger than for those events produced in the central region. These variations in the weighting potentials cause the double-peak feature as shown in Figure 4.6(a), spectrum 2. It can be imagined that when the interaction position shifts from the left side of the detector to the right side, the amplitude of the coplanar signal will change from lower to higher values. In some intermediate regions, such as the top or bottom of the device, the weighting fields of the collecting and noncollecting anodes may be very close. This results in a third peak in the middle, as shown in Figure 4.6(a), spectrum 3.

Another important feature in Figure 4.6(a) is the shift towards lower energy in the peak centroid position for spectrum 4. This spectrum constitutes events that occur at the largest radial position. The reason why events occurring in this region are shifted to a lower channel number can be explained again based on Figure 4.7. Suppose the radial index value at position 1 ( $R_1$ ) is given by Equation 4.1.

$$R_1 = \frac{A_{ca}}{A_{ca} - A_{nca}} \quad (4.1)$$

If the difference of the collecting anode and noncollecting anode at position 1 is  $+D$ ,

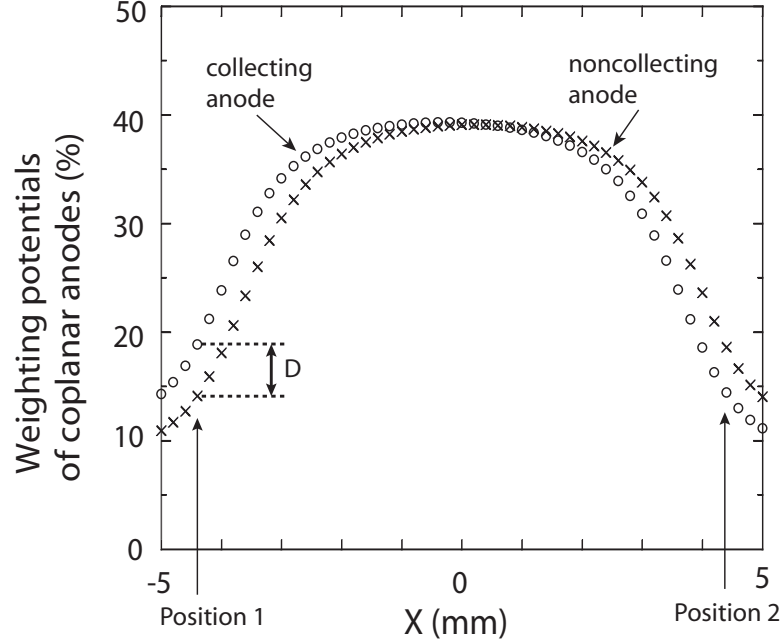


Figure 4.7: Generation 2 detector weighting potential as a function of lateral position. The data points shown are along a center section of the device at a depth of 1 mm from the anode surface.

then the difference at position 2 is  $-D$ , assuming positions 1 and 2 are equidistant to the center of the device. The weighting potential of the collecting anode at position 2 is shifted lower by  $D$  and hence the collecting anode signal will be greater by  $D$ . Likewise, the weighting potential of the subtracted signal at position 2 is shifted lower by  $2D$  and hence the subtracted signal will be greater by  $2D$ . Therefore, the radial index value at position 2 ( $R_2$ ) is given by Equation 4.2.

$$R_2 = \frac{A_{ca} + D}{A_{ca} - A_{nca} + 2D} \quad (4.2)$$

It can be found that  $R_1 > R_2$  if  $A_{ca} > -A_{nca}$ . That is, if the collecting anode signal is greater than the negative component of the noncollecting anode signal, then position 1 will have a larger radial index value than position 2. This inequality will hold for all events occurring at depths greater than 1 pitch ( $\sim 1\text{mm}$ ) from the anodes. Events occurring at position 1 will have smaller pulse amplitude, because the coplanar weighting potential at this position is some finite positive value. Hence,

the largest radial position events will give rise to a smaller peak centroid value.

#### **4.2.2 eV Products design**

For the modified generation 2 design, as described in [53], the effects of a non-symmetric weighting potential are evident in Figure 4.6(b), which are not as severe as in the previous case, but are still substantial. A shift of  $\sim 2\%$  in the photopeak centroid position was observed. Also, multiple peaks for radial position 2 were again observed in addition to a low-energy peak shift for radial position 3. All of these effects provide additional evidence of the weighting potential nonsymmetric effect, resulting in the poor spectroscopic performance near the coplanar anodes.

When the weighting potentials of the coplanar anodes are not symmetric, the difference is a maximum near the periphery and a minimum in the central region. Therefore, by observing the difference of detector performance in the central region and near the periphery (larger radial coordinates), we can observe the improvement of our overall design symmetry between the weighting potentials, since the variation of charge generation and material properties are not likely to depend solely on the radial coordinates.

#### **4.2.3 Third-generation design**

The radial spectra for the generation 3 design are shown in Figure 4.6(c). We observe a much sharper photopeak than in the previous two detectors and a much smaller deviation of the photopeak position. The magnitude of this deviation is  $\sim 0.3\%$ . Also, multiple peaks were not observed for this device, which confirms that the difference in the weighting potentials has been significantly reduced and that the design is superior to the previously discussed designs [54].



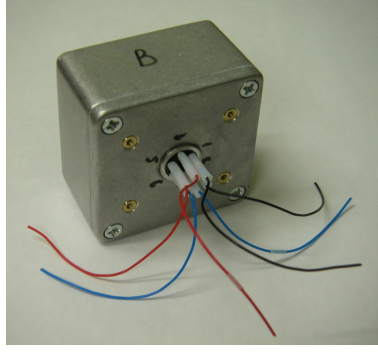


Figure 4.8: Picture of the BSI detector. The 6 wire leads are connected to the 3 electrodes on opposite sides of the detector.

### 4.3 Yinnel Tech / BSI detector results

In this section, a discussion of results from two detectors using Yinnel Tech, Inc., crystals will take place [51]. These crystals were grown by way of the Modified Vertical Bridgman (MVB) technique [56]. Crystals grown by the MVB method are stated to have higher single crystal yield than those grown using the high-pressure Bridgman method. The crystals were fabricated into detectors by BSI using the generation 3 coplanar grid design that was discussed in Section 3.2 [52]. The final detector sizes were  $1.5 \times 1.5 \times 0.9 \text{ cm}^3$ , labeled as BSI CZT2-4-1, and  $1.5 \times 1.5 \times 0.95 \text{ cm}^3$ , labeled as BSI CZT2-4-2. A picture of one of these detectors is displayed in Figure 4.8.

#### 4.3.1 Detector fabrication

Fabrication of the 2 detectors was done by BSI. During our initial discussions with them, we agreed upon a series of tests to help ensure that the detector would have suitable performance. These tests are as follows:

1. Measurement of the interstrip resistance. The resistance should be greater than  $1 \text{ G}\Omega$  on at least one of the surfaces.

2. Leakage current measurement between the coplanar grid anodes (tested in the range of 0 V - 60 V) and cathode (tested in the range of 1000 V - 2000 V).
3. Measurement done at room temperature of the spectroscopic performance at 59.5 keV and 662 keV.

Before these tests were done, however, an initial evaluation of the detector was conducted by BSI using simple planar electrodes. These tests would help determine whether the crystal would be suitable as a radiation detection device. The crystals were first ground, polished, and etched using a  $\text{Br}_2$  in methanol etch. Then, planar gold electrodes were deposited on opposite faces of the crystal using a solution of gold and 5% hydrochloroauric acid. The area of the electrodes were  $\sim 1 \text{ cm}^2$ . Two initial measurements conducted to determine the electron transport properties, and therefore the material quality, were  $\mu_e \tau_e$  and  $\mu_e$ . The  $\mu_e \tau_e$  measurements were found using the Hecht relationship [57], and the  $\mu_e$  using time of flight measurements [58, 59]. Both measurements were taken using  $\alpha$ -particles irradiated on the cathode side. The results for the two crystals are summarized in Table 4.1. These results are generally quite high, so the electron transport properties of the two crystals were deemed satisfactory for detector operation. In addition, measurements were also taken of the I-V characteristics of these crystals. Fitting a line to this data, one can determine the resistivity  $\rho$ , which is given in Table 4.1. The area of the electrodes were substantially smaller than the surface area of the crystal. Hence, the leakage current measurements should be almost exclusively due to bulk leakage current and so the resistivity measured should be the bulk resistivity. Finally, spectral measurements were taken using an Am-241 source. The energy resolution for these measurements, taken at 1000 V bias, is given in Table 4.1 and was found to be very good for both crystals. All of these measurements provided strong evidence

Table 4.1: Electron transport measurement data taken by BSI for 2 Yinnel Tech detectors.

Crystal number	$\mu_e$ (cm <sup>2</sup> /Vs)	$\mu_e\tau_e$ (cm <sup>2</sup> /Vs)	$\rho$ ( $\Omega$ cm)	FWHM at 59.5 keV (keV)
CZT2-4-1	740	$6.8 \times 10^{-3}$	$1.75 \times 10^{10}$	4.2
CZT2-4-2	750	$6.9 \times 10^{-3}$	$1.03 \times 10^{10}$	6.7

Table 4.2: Coplanar grid detector measurements taken by BSI after fabrication. The energy resolution measurements were taken using the relative gain method for electron trapping compensation and with side ‘A’ biased as the anode.

Crystal number	Resistance (G $\Omega$ )		Energy resolution (% FWHM)	
	side A	side B	59.5 keV	662 keV
CZT 2-4-1	1.7	1.03	8.4 keV (14.1%)	13.2 keV (2.0%)
CZT 2-4-2	5.0	1.28	8.2 keV (13.8%)	12.0 keV (1.8%)

that these crystals could result in good performing detectors.

The next step involved the actual fabrication of the coplanar grid detectors. The crystal surface processing was done in a similar fashion to what was previously described, except an extra step was included for surface passivation. Standard photolithography techniques were used to pattern the coplanar grids using gold as the electrode material. Coplanar grid electrodes were deposited onto both sides of the crystal for reasons that will be explained in Section 4.3.2. The crystal was then mounted onto a dielectric substrate and wire bonded using gold wires. The aforementioned tests were conducted on the detector and the results are described in [60]. A summary of these results, including the intergrid resistance, and the energy resolution at 59.5 keV and 662 keV are shown in Table 4.2. The interstrip resistance exceeded our requirement of  $> 1$  G $\Omega$  on both sides of the detector, and the spectral measurements indicated very good energy resolution can be achieved with these detectors.

#### 4.3.2 Electrode configuration and measurements

Through discussions with Yinnel Tech, we were made aware that the CZT crystals they grew have a Te-rich side and a Cd-rich side. Furthermore, we were informed that there was always one best side for anode operation. Hence, in order to ensure

that the proper side could be selected for anode operation, coplanar grid electrodes were fabricated on both sides of the detector. To operate one side of the detector as a cathode, the three electrodes on that side are coupled together by connecting the corresponding signal wires together. The other side is then operated in the standard coplanar anode mode. With the advent of coplanar anodes on both sides of the detector we now have the added flexibility to select which side is to be operated as the anode and which side is to be operated as the cathode. This then assures us that the detector can be operated in a means to achieve the best performance.

To characterize the performance of the detectors at room temperature, we acquired gamma-ray spectra using either of the two electron trapping compensation techniques. One technique is the relative gain method and the other technique is the depth sensing method. With coplanar electrodes on either side of the detector (labeled side ‘A’ and ‘B’) we acquired spectra for both biasing configurations, that is with side ‘A’ biased as the anode and side ‘B’ biased as the cathode and *vice versa*. We also conducted  $\mu_e\tau_e$  product calculations using the method for single-polarity charge-sensing devices [61]. In this method, we expose the detector to a low energy  $\gamma$ -ray source on the cathode side such that the electron cloud will drift over the entire detector thickness. Then, we measure the photopeak centroid position for spectra acquired at two different bias voltages. The  $\mu_e\tau_e$  product can be determined based on the photopeak shift observed at these two bias voltages.

#### 4.3.3 Detector spectroscopic performance

We began by testing the Yinnel Tech/BSI CZT2-4-2 detector because it was found by BSI to be the better of the two detectors. With a bias of -1200 V supplied to the cathode, -40 V supplied to the noncollecting anode, and with the collecting anode and boundary electrode set to ground, we achieved a FWHM at 662 keV of 1.65%

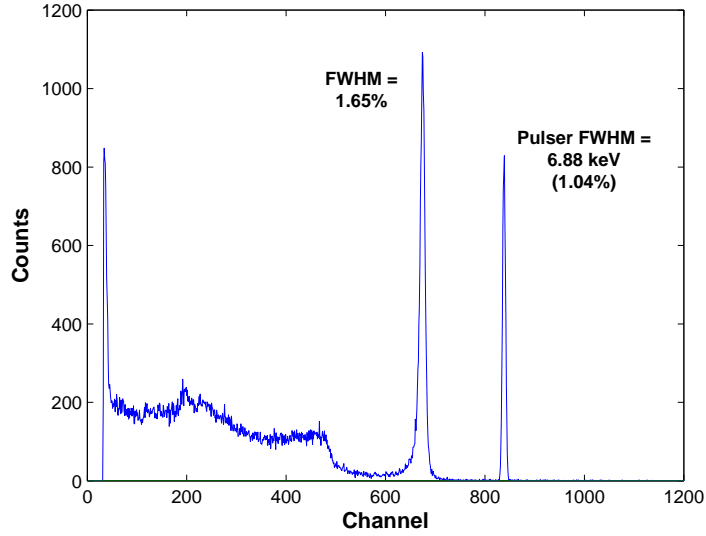


Figure 4.9: 662 keV  $\gamma$ -ray energy spectrum for the CZT2-4-2 detector using the relative gain compensation method. Results in the range of 1.65% to 1.70% were consistently achieved.

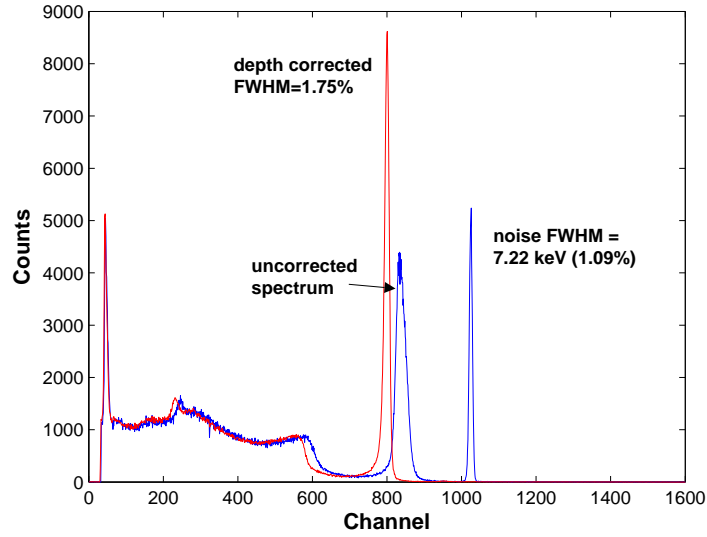
using the relative gain method for electron trapping compensation [62]. The pulse height spectrum for this measurement is given in Figure 4.9. These results were a significant improvement from previous detectors. The spectrum in Figure 4.9 was acquired with side ‘A’ biased as the anode. By reversing the biasing polarity such that side ‘B’ is biased as the anode, we achieved a FWHM at 662 keV of 6.8% using the relative gain method, which clearly indicates a severe degradation in performance.

As was previously described, the depth sensing method for electron trapping compensation allows us to obtain energy spectra as a function of interaction depth. For the condition in which side ‘A’ is biased as the anode, Figure 4.10(a) shows both the uncorrected  $\gamma$ -ray spectrum and depth corrected spectrum. This spectrum shows a depth corrected resolution of 1.75% at 662 keV, which is slightly poorer than that achieved with the relative gain method [62]. Figure 4.10(b) illustrates the depth dependency for energy resolution in the detector where larger depth indices indicate increasing distance from the anodes. We find that the resolution remains fairly con-

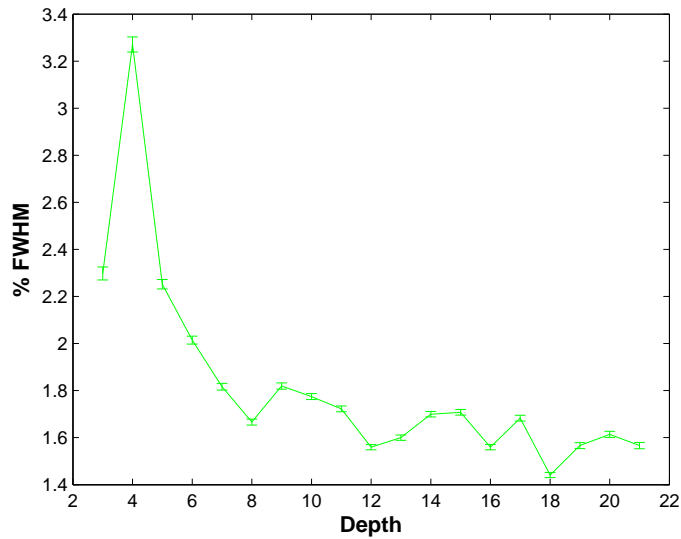
stant in the bulk of the detector, but then degrades significantly near the coplanar anodes. This effect was surprising to us, because of what we had observed on an eV Products detector using a similar generation 3 coplanar grid electrode design as described in Section 4.1.3. However, in the new generation 3 design, restrictions were imposed by BSI that only allowed for a minimum strip dimension of  $150\text{ }\mu\text{m}$ . These restrictions were not as severe for the eV Products detector, and so better weighting potential symmetry could be achieved. With side ‘B’ biased as the anode, we acquired the energy spectrum as shown in Figure 4.11(a). In Figure 4.11(b) we observe linearly degrading resolution as a function of increasing depth from the coplanar anodes. These results indicate that the degradation of energy resolution is related to the drift distance of electrons, where increasing drift distance causes more significant photopeak broadening. The asymmetric effect that we observed with this detector is discussed further in Section 4.3.4.

A measurement of the CZT2-4-2 detector  $\mu_e\tau_e$  product was carried out as described previously. With side ‘A’ biased as the anode we measured a value of  $1.13 \times 10^{-2}\text{ cm}^2/\text{V}$ . This value is high in comparison to traditional  $\mu_e\tau_e$  values, which should help to explain the excellent performance achieved with this detector. With side ‘B’ biased as the anode we measured a value of  $8.83 \times 10^{-3}\text{ cm}^2/\text{V}$ . The uncertainty in this measurement is characterized by the depth resolution of the detector, which is  $\sim 5\%$ , so the difference in the  $\mu_e\tau_e$  for opposite biasing polarities is significantly greater than the uncertainty. This result provides some indication why we observed degraded performance with side ‘B’ biased as the anode, since the detector characteristics were observed to be asymmetric.

Energy spectra were also taken with the Yinnel Tech/BSI CZT2-4-1 detector and very similar behavior was observed. The best resolution achieved for this detector

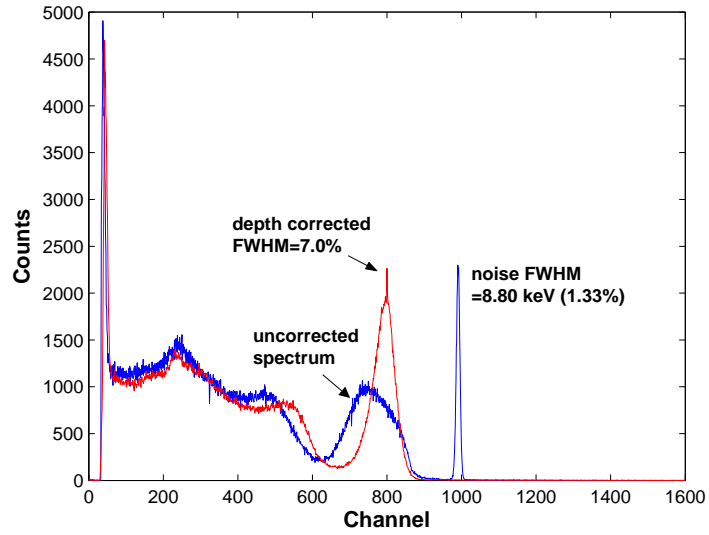


(a) Energy spectrum for 662 keV  $\gamma$ -rays using the depth sensing method, where the red is the depth corrected spectrum and the blue is the uncorrected spectrum.

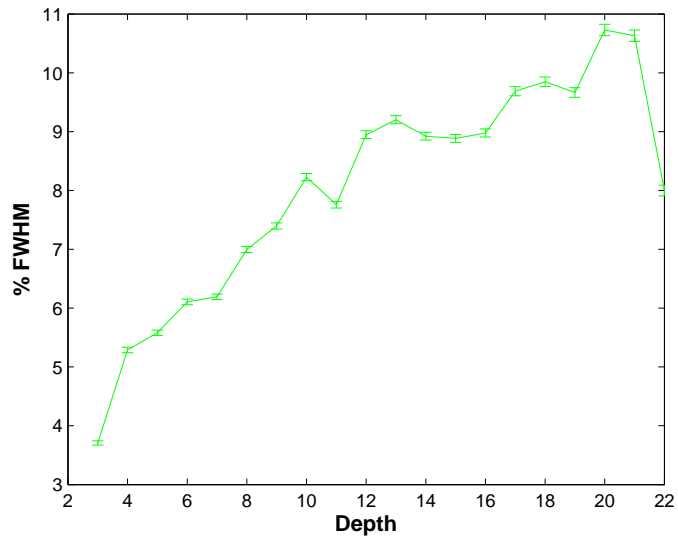


(b) Resolution versus depth index were increasing depth indices indicate increasing distances from the anode side of the detector.

Figure 4.10: These measurements were taken using the BSI CZT2-4-2 detector with side 'A' biased as the anode. The cathode was set to -1400 V and the noncollecting anode was set to -45 V.



(a) 662 keV spectrum.



(b) Resolution versus depth index plot.

Figure 4.11: BSI CZT2-4-2 detector measurements with side 'B' biased as the anode. The cathode was set to -1200 V and the noncollecting anode was set to -50 V.



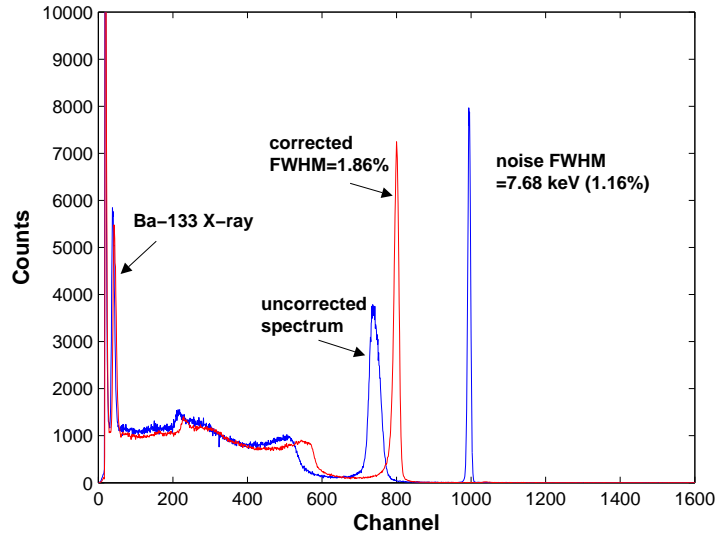


Figure 4.12: Cs-137 spectrum taken with the BSI CZT2-4-1 detector employing the depth sensing method. In this spectrum, the 31 keV X-ray from Ba-133 is clearly visible.

Table 4.3: Energy resolution data for both Yinnel Tech/BSI detectors using the depth sensing or relative gain methods for electron trapping compensation and with either side ‘A’ or side ‘B’ biased as the anode.

Detector	Anode side	% FWHM with depth sensing	% FWHM with relative gain
CZT2-4-2	A	1.75%	1.65%
	B	8.3%	6.8%
CZT2-4-1	A	1.86%	1.99%
	B	8.3%	7.0%

was 1.86% at 662 keV. A spectrum of this detector employing the depth sensing method for electron trapping compensation is shown in Figure 4.12. A summary of the energy resolution data for both detectors is given in Table 4.3.

#### 4.3.4 Discussion of asymmetric characteristics

The asymmetric effect discussed previously may be caused either by a surface effect or by a bulk effect. In the case of a surface effect, changes in the surface resistivity may cause the electric field in the device to be nonuniform, resulting in a reduced electric field in the bulk of the semiconductor. Such an effect could cause the linearly degrading energy resolution observed in our measurement, since the effect

of electron trapping will become more severe in this case. However, observations of the cathode waveform do not comply with this hypothesis, since the cathode signals were observed to be linear and the signal rise times were on the same order of those observed when side ‘A’ was biased as the anode. Hence, a reduced electric field due to a surface layer effect is most likely not the cause of the poor performance. The other hypothesis is that the asymmetric behavior is due to a material bulk effect in which the bulk properties change as a function of biasing orientation. If the bulk properties changed such that the transport of electrons was inhibited, such as a decreasing  $\mu_e\tau_e$ , this could explain our measured result. As was reported in Section 4.3.3, the  $\mu_e\tau_e$  did decrease by  $\sim 21\%$ , however this reduction was not enough to substantiate the dramatic degradation in resolution that we observed. Therefore, it is not yet evident the cause of the resolution degradation with side ‘B’ biased as the anode.

Another study by Wright *et al.* also indicated asymmetric behavior on  $\{1\ 1\ 1\}$  oriented CZT crystal acquired from Yinnel Tech [63]. In this study, (111)A and (111)B surfaces were identified using a special lactic acid etch. Then, tests were carried out using the same CZT crystal, but processed with different chemical treatments. One of the chemical treatments used was 5%  $\text{Br}_2$  in methanol, which is the same etchant used on the BSI detectors in our study. For this scenario, the energy resolution at 59.6 keV was found to be slightly better when the (111)B surface was operated as the anode. Similar to our observation, differences in the  $\mu_e\tau_e$  values were also reported as a function of whether the (111)A side or (111)B side was biased as the cathode. These observations were interpreted to be likely the result of variations in the surface recombination rates of electrons due to differences in the surface stoichiometry [63]. In this study, measurements of the surface recombination velocities were carried out and were found to be more than  $2\times$  greater when the (111)A surface was operated

as the anode. Although these findings do provide evidence for asymmetric behavior of CZT, they do not provide a valid explanation for the linearly degrading resolution as a function of increasing drift distance that we observed. Greater trapping at the surface should effect the energy resolution equally at all depths, however we did not observe this in our experiment. Hence, further study must be done to fully understand the physics of the asymmetric behavior.

## CHAPTER V

### Detector Modeling

The experimental data reported thus far has shown that coplanar grid CZT detectors can result in good spectroscopic performance devices. We showed that  $< 2\%$  energy resolution at 662 keV can be achieved. Although such results are very promising, there are still many aspects of these devices that have not been fully understood through experimentation alone. Fortunately, simulation tools can be used to help answer some key issues pertaining to these devices that would otherwise be difficult to understand. The simulation packages used in this study include Maxwell for modeling the signal induction process and drifting of charge carriers in the electric field, in addition to Geant4 for modeling the physics of gamma-ray interactions within the detector [48, 64]. A  $1.5 \times 1.5 \times 1.0 \text{ cm}^3$  detector was modeled employing the generation 3 coplanar grid design. The results from these simulations and the insight they provide us will be discussed in this chapter.

#### 5.1 Simulation methods

The simulations for the coplanar grid CZT detector were carried out in a series of steps detailed in the block diagram in Figure 5.1. The first step involves simulating the detector charge induction characteristics using Maxwell. In Maxwell, we modeled the electrode geometry “cgre7a2” discussed in Section 3.2 and employed in the BSI

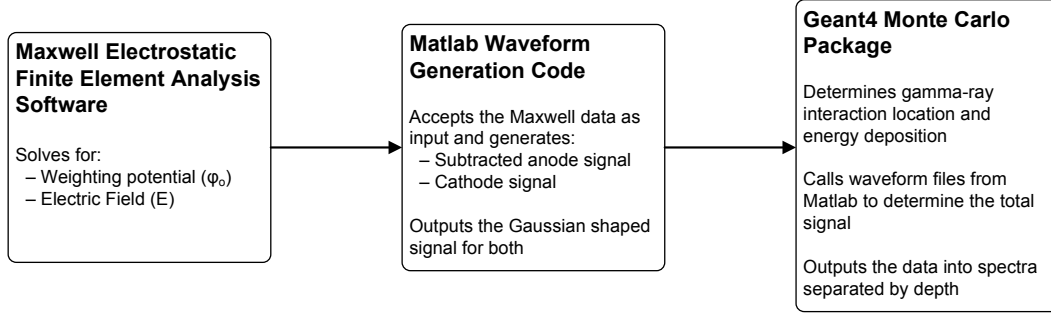


Figure 5.1: Block diagram highlighting the steps for the simulations discussed in this chapter.

detectors. Using this simulation tool, we solved for the weighting potential  $\phi_o$  of the subtracted anode and cathode, in addition to the electric field  $\mathbf{E}$  and saved this information to a grid. For the 3-D simulations discussed in Section 5.2 a spacing of 0.1 mm in the x- and y-directions (lateral directions) and 0.2 mm in the z-direction (depth) was used. For the 2-D simulations discussed in Section 5.3 a finer spacing of 25  $\mu\text{m}$  in the x-direction and 0.25 mm in the z-direction was used. Both of these electrostatic parameters are necessary in order to generate the pulse waveforms due to the electron drift. After this data was saved, the next step involves running a MATLAB program, which does the electron transport calculations [65].

The idea behind the MATLAB waveform generation code is to calculate the path of the electrons, governed by the electric field, as they drift toward the anodes. In these simulations, we assumed that the holes remain stationary during the time it takes for the electrons to be collected. The program determines the change in the electron position  $\Delta\lambda$  for every time step  $\Delta t$ , which can be simply calculated based on Equation 5.1.

$$\Delta\lambda(x, y, z) = \mu_e \mathbf{E} \Delta t \quad (5.1)$$

Care was taken to ensure that the time steps were sufficiently small such that the electrons conform to the direction of the electric field lines. For these simulations, time steps of 10 ns were typically used. Once the change in position is determined,

it is a straightforward matter to determine the change in the induced charge using Equation 2.2. In our model, we also incorporated the effects of electron trapping. We can employ Equation 2.5 to determine the number of electrons trapped within each time step, which can then be included in the charge induction equation. These signals emulate the preamplifier waveforms. After the preamplifier signal is generated, we then determine the shaped signal. A CR-(RC)<sup>4</sup> shaping filter with a variable shaping time was modeled. A shaping time of 2  $\mu$ s was chosen in the simulation, because this was the value used in the experiment. The shaped cathode and subtracted anode signals were finally saved in a data file, ready for the next step using the Geant4 program.

The last step in the simulation involves running the Geant4 Monte Carlo code for modeling the gamma-ray interaction physics. This program models all major gamma-ray interaction mechanisms, such as photoelectric absorption, Compton scattering, pair production, and Rayleigh scattering. A gamma-ray flood source was positioned on the cathode side. For each hit, the 3-D position information and energy deposition was determined in the simulation. The number of charge carriers (e-h pairs) produced was determined by assuming an average ionization energy of 4.7 eV/e-h pair. Other parameters assumed in the model are given below in Table 5.1. Fano statistics were included by sampling a random variable from a Gaussian distribution and spreading it by  $\sigma_{Fano} = \sqrt{F \cdot N}$ , where  $F$  is the Fano factor and  $N$  is the total number of charge carriers produced. Other causes of peak broadening were included into the model as well, including electronic noise and electron trapping statistics. The standard deviation of the electronic noise  $\sigma_{noise}$  can be calculated simply by applying the error propagation formula to Equation 2.6, resulting in Equation 5.2

$$\sigma_{A_{sub}} = (\sigma_{A_{ca}}^2 + (G \cdot \sigma_{A_{nca}})^2)^{1/2} \quad (5.2)$$

Table 5.1: Parameters which were used for modeling the coplanar grid CZT detector in Geant4.

ionization energy ( $\epsilon$ )	4.7 eV/e-h pair
Fano factor (F)	0.1
ENC <sub>anode</sub>	448 electrons
ENC <sub>cathode</sub>	377 electrons
$\mu_e \tau_e$	$10^{-2} \text{ cm}^2/\text{V}$

where  $\sigma_{noise} = \sigma_{A_{sub}}$  and  $\sigma_{A_{ca}} = \sigma_{A_{nca}} = \text{ENC}_{\text{anode}}$ , therefore

$$\sigma_{noise} = (1 + G^2)^{1/2} \cdot \text{ENC}_{\text{anode}}$$

For a relative gain of 1 and an ENC of 448 electrons, this gives a noise FWHM of 7 keV, which is the best-case-scenario noise measured in the experiment. The last cause of peak broadening that was included into the Geant4 code was electron trapping statistics. Although electron trapping was determined in the MATLAB waveform generation program, the electron trapping statistics could not be included into that program because of missing information. One needs to know the number of electrons drifting toward the anode in order to calculate the uncertainty in the number being trapped  $\sigma_{trap}$ . For this calculation, we assume a binomial distribution since the probability for an electron to be trapped  $p_{trap}$  is not in general  $\ll 1$ , where a Poisson distribution can be assumed. Therefore, the uncertainty is calculated as  $\sigma_{trap} = \sqrt{N_o \cdot p_{trap} \cdot (1 - p_{trap})}$ , where  $N_o$  gives the initial number of electrons formed. These sources of peak broadening are incorporated together with the waveform data generated in MATLAB in order to determine the total anode and cathode signals.

In the Geant4 program, events can be processed in different ways. For the case of a single-site event, the interaction location is determined and the closest index value, as established in MATLAB, is found. Then, the maximum values of the shaped anode and cathode waveforms for this index position are determined. This process nearly emulates what is done by the peak-hold circuit in the experiment, as

discussed in Section 3.4. In the case of multi-site events, the location of each gamma-ray interaction is obtained and the corresponding index values are determined. The shaped signals from each index value are weighted by the amount of energy deposited at each site and then summed together. The maximum value for the resulting shaped signal is determined just as in the single-site case. The program then calculates  $C/A$  to determine the depth of the gamma-ray interaction. Then, the data gets binned into pulse height spectra separated by depth and saved into a data file for further analysis.

## 5.2 Comparison study of 2 electron trapping compensation techniques

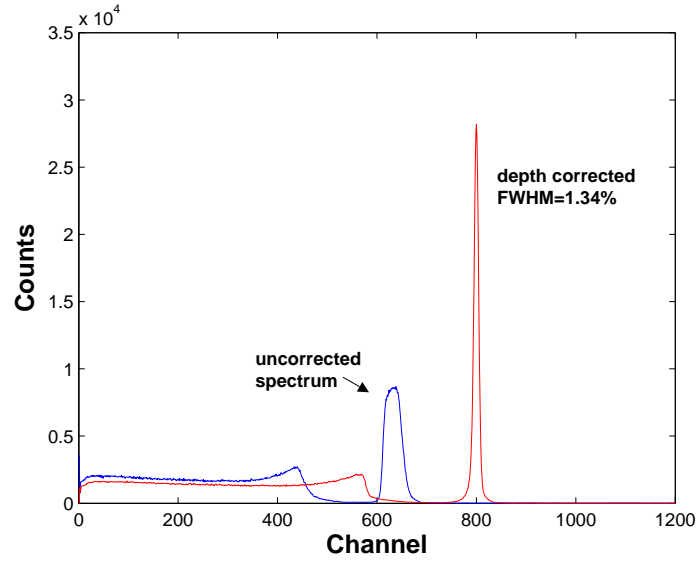
We have observed through experimentation that both the depth sensing method and the relative gain method can be used to correct for electron trapping. For the BSI detectors, differences in spectroscopic performance were observed for each method, however these differences did not always follow expectations. As shown in Table 4.3, for the CZT2-4-2 detector, the best energy resolution was recorded using the relative gain method. For the CZT2-4-1 detector, the depth sensing method gave way to the best energy resolution results. According to theoretical predictions, the depth sensing method should result in better electron trapping compensation when employing a boundary electrode [55]. However, this was not observed in all cases. Moreover, differences in the energy resolution using either method varied by only  $\sim 0.1\%$ . This study sought to determine through simulation which method for electron trapping compensation would give better performance.

Simulation results for depth sensing are shown in Figure 5.2(a). The depth corrected energy resolution was determined to be 1.34% FWHM at 662 keV. The result employing the relative gain method is shown in Figure 5.2(b), which was obtained

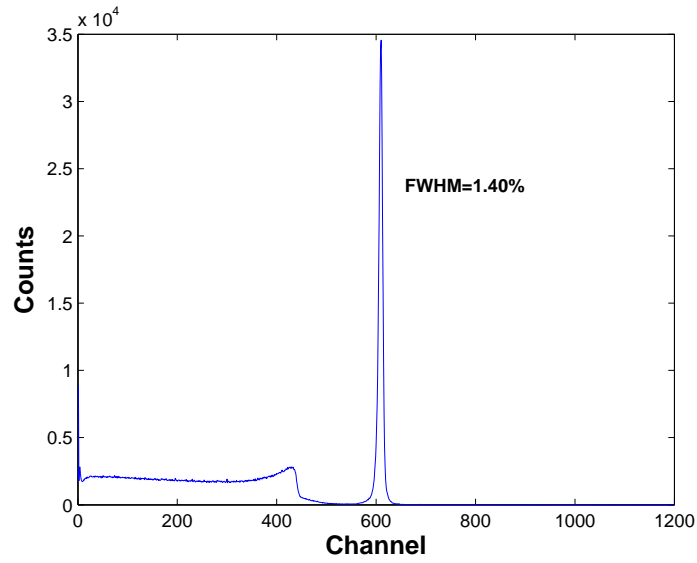


by setting the relative gain to the optimized value of 0.81. This value was determined by factoring in the relative gain component to the weighting potential data and re-running the simulation until the best energy resolution was achieved. The best energy resolution determined using this method was 1.40% FWHM at 662 keV. The simulation results agree with theoretical predictions indicating that the depth sensing method should be the better method for electron trapping compensation when a boundary electrode is employed. The small difference in energy resolution of 0.06% observed between these two compensation techniques agrees quite well with the experimental data.

To better understand the cause of the discrepancy in energy resolution between the relative gain method and the depth sensing method, events were separated according to the interaction location. The first case involved only recording events with interactions that occurred entirely within the center portion of the detector. The center region was considered anything within a 5 mm radius of the middle of the detector. The second case involved only recording events with interactions that occurred entirely outside of this region. This is similar to radial sensing, except no calculations of radial position are necessary, since in the simulation we know the exact locations of the gamma-ray interactions. Figure 5.3(a) shows the resolution as a function of depth for both cases when the relative gain is set to 1 (depth sensing method). Correspondingly, Figure 5.3(b) shows the same data when the relative gain is set to 0.81. Based on our theoretical predictions as well as the experimental data, the resolution should be poorest for the edge region of the detector. In addition, applying a non-unity relative gain should result in greater weighting potential nonuniformity along the edge of the detector than for the scenario in which the relative gain is equal to 1 [55]. Hence, poorer energy resolution should be observed in



(a)



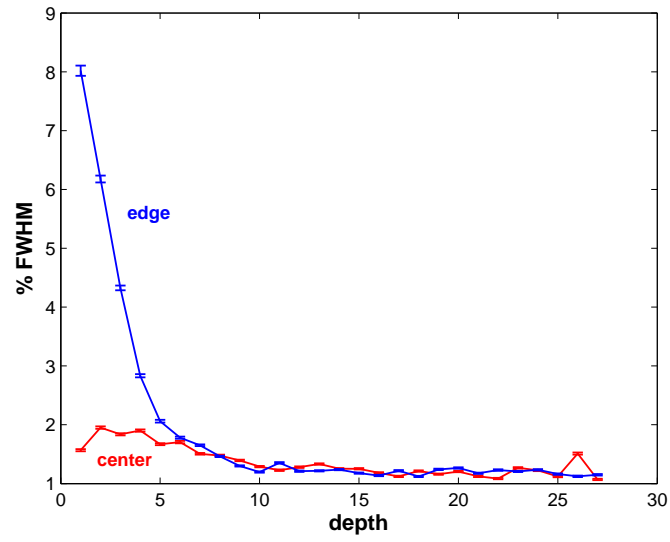
(b)

Figure 5.2: Simulated Cs-137 spectra for the coplanar grid detector, where (a) was acquired employing the depth sensing method with a relative gain of 1 and (b) was acquired employing the relative gain method with an optimized relative gain of 0.81.

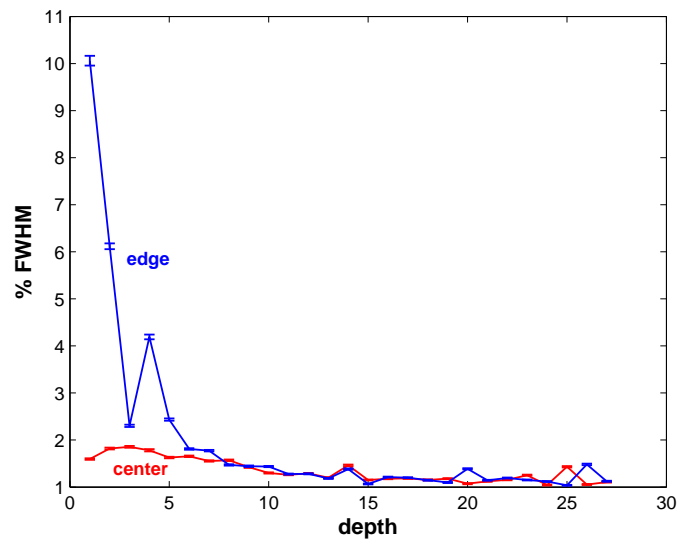
the relative gain method. However, according to the energy resolution versus depth data shown in Figure 5.3, no significant difference was observed. This result shows that applying a non-unity relative gain may not have as significant of an effect on the weighting potential nonuniformity as initially thought. Hence, the small discrepancy in energy resolution observed using either compensation technique is consistent with the simulated results in Figure 5.2. Note that these simulations do not include the effects of material nonuniformities, resulting in variations in the  $\mu_e\tau_e$ . This effect could give a further edge to the depth sensing method, if electron trapping varies only as a function of depth.

### 5.3 Surface effects of CZT

It is widely known that the surface properties of CZT can affect the transport of electrons through the crystal, ultimately resulting in variations in the spectroscopic performance [63,66]. Common crystal treatment practices include polishing, chemical etching, and surface passivation in order to result in a good working detector [67, 68]. A passivation layer will help to reduce surface leakage current, but it may adversely affect the electron collection. In this section we explore this effect further by simulating the electron drift for two different surface boundary conditions. In these simulations, we assume the passivation layer to be a thin film of 600 nm  $\text{TeO}_2$  located between the strips with a conductivity  $\sigma = 10^{-13} \text{ S/m}$  (4 orders of magnitude less than CZT) and electric permittivity  $\epsilon = 10$ . The two different surface boundary conditions modeled were (a) a linearly varying potential at the oxide layer between the strips, corresponding to the case when a relatively high leakage current could regulate the potential on the gap, and (b) the oxide layer was left floating such that no potential was assumed, corresponding to a high surface resistance. 2-D Maxwell



(a)



(b)

Figure 5.3: Resolution versus depth data separated by interaction location where (a) is for a relative gain of 1 and (b) is for a relative gain of 0.81. The differences observed between (a) and (b) are fairly minimal.

simulations of the weighting potential and electric field were done for both of these boundary conditions.

### 5.3.1 Modeling the electron trajectory

The charge carriers generated in the detector will always follow a trajectory dictated by the electric field lines. Hence, we can use the electric field data computed in Maxwell to determine the electron track. In Maxwell, we apply similar voltage potential parameters as were used in the experiment. That is  $V_{\text{cat}} = -1200\text{V}$  and  $V_{\text{be}} = V_{\text{ca}} = 0\text{V}$ , where  $V_{\text{cat}}$ ,  $V_{\text{be}}$ , and  $V_{\text{ca}}$  are the cathode, boundary electrode, and collecting anode potentials, respectively. The computed electron track for a noncollecting anode bias  $V_{\text{nca}} = -43\text{V}$  is shown in Figure 5.4. We observe that on the left side of the figure (linearly varying potential), a critical bias was achieved where electrons traveling underneath the noncollecting anode were steered away and not collected by the noncollecting anode. From this figure, it is clear that a large fraction of these electrons end in the gap between the strips. On the right side of the detector (floating potential), electrons were collected by the noncollecting anode which is nonideal. However, we found that the electrons are being focused to the collecting anode better for this case. The effects on the electron trajectory for an increased noncollecting anode bias are shown in Figure 5.5. This data is shown for  $V_{\text{nca}} = -86\text{V}$ . On the left side, we observe better electron collection at this bias, however some of the electrons still terminate in the gap region. For the right side, full collection of the electrons at the collecting anode is achieved. Therefore, the boundary conditions on the right side are better for proper steering of the electrons toward the collecting anode. The reason for this can be seen in Figure 5.6. Here we find that for the floating potential case, the potential has a convex shape. This feature will help to bend the electric field lines such that more of them terminate

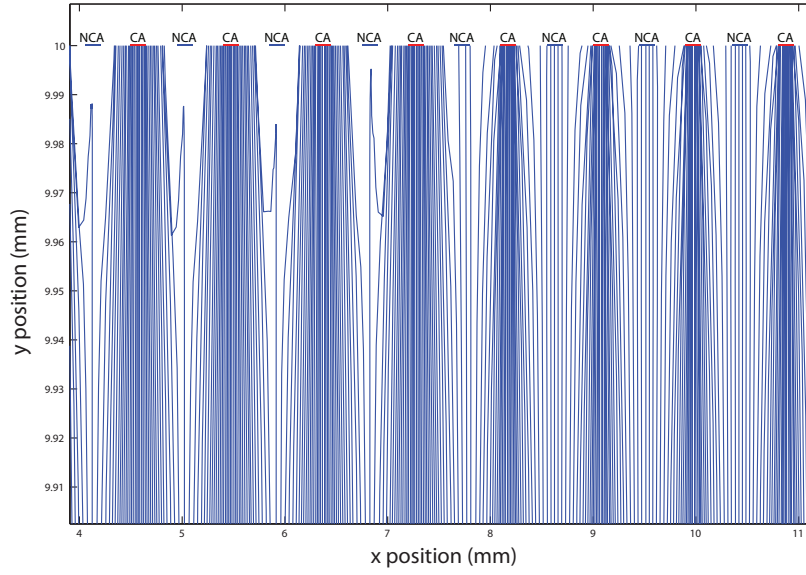


Figure 5.4: Illustration of the electron track for electrons originating at  $z = 8$  mm determined for a cathode bias of -1200 V and a coplanar anode bias of 43 V. The effects for two different boundary conditions are shown on the same plot. The left side was calculated for a linearly varying potential at the surface and the right side was calculated when no potential was applied at the surface (floating case). The right side shows better focusing of the electrons.

on the collecting anode than in the linearly varying case, since  $E = -\nabla V$  and the gradient of the potential increases in magnitude as we get closer to the collecting anode. Hence, better focusing of the electrons will result. This electron track data helps us to better understand the best surface boundary conditions for improved electron collection.

### 5.3.2 Modeling the spectrum

As discussed in Section 5.1, we can incorporate the electron track information with the weighting potential data to generate pulse waveforms in our device, which can then be employed in Geant4 to simulate the energy spectrum. With the MATLAB waveform generation program, the response in the detector was determined for every  $25 \mu\text{m}$  in the x-direction (the lateral direction). The fine spacing that was used

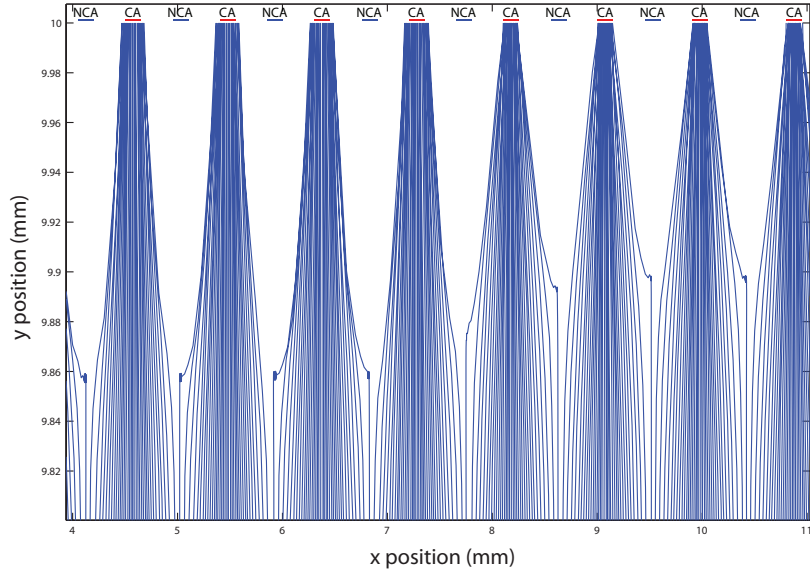


Figure 5.5: Illustration of the electron track determined for a cathode bias of -1200 V and a coplanar anode bias of 86 V. A critical bias was achieved for the right side (floating potential case) where full electron collection takes place.

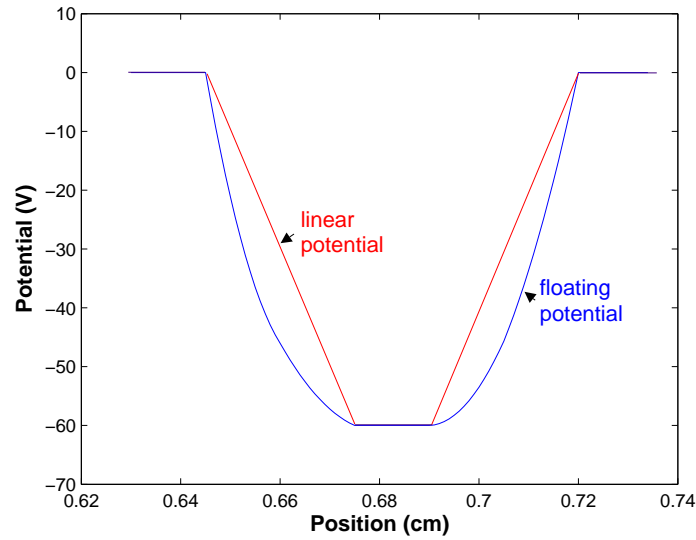


Figure 5.6: Plot of the potential at the surface of the detector, where the left and right sides are the positions of a collecting anode and the middle is the position of a noncollecting anode. The convex shape in the potential for the floating case helps to focus electrons better to the collecting anode than for the linearly varying case.

allowed us to incorporate the effects of the finite electron cloud size as well as charge diffusion into our model. In this model, the electron cloud parameters were chosen based on the simulation work done by Zhang [69]. For a 662 keV gamma-ray event, the electron cloud radius  $r_{\text{cloud}}$  has a mean value  $\overline{r_{\text{cloud}}} = 100 \mu\text{m}$  and a standard deviation  $\sigma_{r_{\text{cloud}}} = 32 \mu\text{m}$ . This data allows us to estimate the electron cloud radius for every interaction. An electron  $i$  is sampled within this cloud assuming a uniform distribution and then the effects of charge diffusion are factored in. Charge diffusion results in a spreading in the charge cloud as it drifts toward the anodes and this spread has a standard deviation  $\sigma_{\text{diff}}$  given by Equation 5.3

$$\sigma_{\text{diff}} = \sqrt{\frac{2kTd}{e\mathcal{E}}} \quad (5.3)$$

as discussed in Knoll [1], where  $kT/e$  is 0.0253V at 20°C, and  $d$  is the electron path length, and  $\mathcal{E}$  is the electric field magnitude. It is then relatively simple to determine the offset of the electron's arrival position  $\Omega_i$  due to diffusion by sampling from a Gaussian distribution and introducing a spread of  $\sigma_{\text{diff}}$ . The amount of offset then allows us to determine the response  $R_i$  due to the  $i$ -th electron, since we can estimate that

$$R_i = R(x_i, z)$$

where  $x_i = x + \Omega_i$  and  $(x, z)$  is the gamma-ray interaction location. If  $x_i$  falls between two grid points, then a simple linear interpolation is done to approximate the response. In these simulations, the response was calculated assuming 200 electrons in the starting electron cloud. Then, the process of determining the total anode and cathode signal is done the same way as discussed in Section 5.1. Finally, the energy spectrum can be determined.

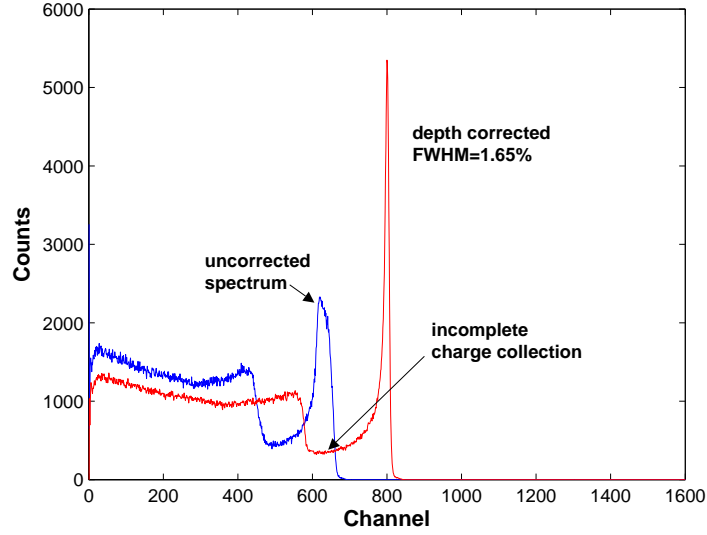
Energy spectra were determined for the surface boundary condition in which the



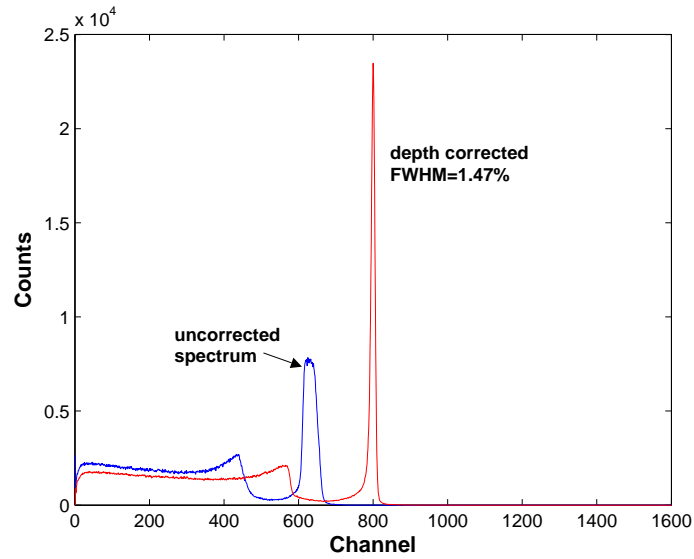
oxide layer was left floating, which are shown in Figure 5.7. The spectrum in Figure 5.7(a) represents the case in which  $V_{\text{nca}} = -43\text{V}$ . The effect of incomplete charge collection can be seen in this spectrum constituting counts within the gap region between the photopeak and the Compton edge. This effect also leads to low energy tailing. The spectrum in Figure 5.7(b) represents the critical bias of  $V_{\text{nca}} = -86\text{V}$  where full collection of the electrons take place.

To see how accurately the model represents our experimental observations, we include measurement results for the BSI CZT2-4-1 detector discussed in Section 4.3. Spectra for two different biases are shown in Figure 5.8. The first case is given in Figure 5.8(a) where  $V_{\text{nca}} = -20\text{V}$ . The second case is given in Figure 5.8(b) where  $V_{\text{nca}} = -50\text{V}$ . The best spectroscopic results were obtained for the higher bias, because of better electron collection. It is thought that once we achieve a bias near to the critical bias, where all electrons are steered toward the collecting anode, increasing the bias any further will be without benefit and will actually result in energy resolution degradation due to increased electronic noise. For the lower bias case, we can observe the effects of incomplete charge collection, which results in a significant low energy tail as well as counts in the Compton gap region. Because of these effects, significant energy resolution degradation was observed for the low bias case.

Comparing our model to the experimental data, we observe some similarities as well as some discrepancies. For both sets of data, the effects of incomplete charge collection can be seen in the lower bias case. For the higher bias case, both the modeled data and the experimental data display a more symmetric photopeak with a much less significant fraction of counts in the Compton gap. This indicates better charge collection. However, the modeled data shows an energy resolution degradation from



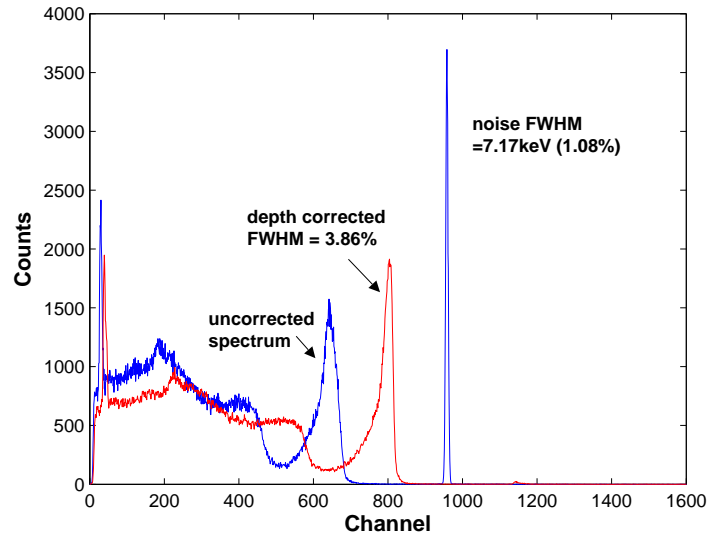
(a)



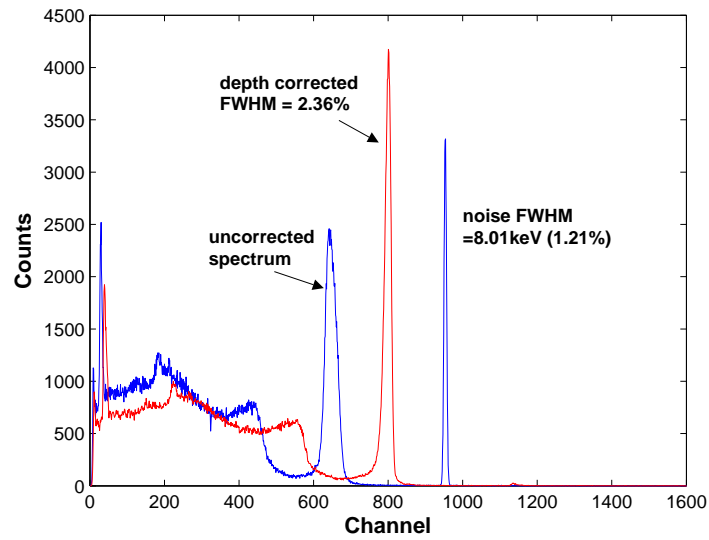
(b)

Figure 5.7: Simulated spectra for the case in which the oxide layer was left floating where (a) is with a coplanar bias of 43 V and (b) is with a coplanar bias of 86 V. For these simulations the cathode was set to -1200 V. The effects of incomplete charge collection are shown in (a).

1.47% to 1.65% FWHM at 662 keV due to decreasing bias. The degradation is much more severe for the experimental case, from 2.36% to 3.86% FWHM at 662 keV. Thus, it is apparent that our model is not entirely complete. For one, it is generally accepted that material nonuniformities, such as Te inclusions, can play a substantial role in spectroscopic performance. Hence, this effect should be incorporated into future models by assuming regions in the detector with high electron trapping probability. Secondly, electronic noise was assumed to be just one value for all operating conditions, which we know is only an approximation. Therefore, an analytical model of the noise as a function of biasing condition should also be included. Lastly, spectra were generated only for one case of the surface boundary conditions. Other cases should also be modeled and compared to the experimental data.



(a)



(b)

Figure 5.8: Experimental data taken with the BSI CZT2-4-1 detector using a cathode bias of -1200 V and a noncollecting anode bias of -20 V (a) and -50 V (b). The degradation in resolution observed in (a) was likely the result of incomplete charge collection.

## CHAPTER VI

### Multi-Pair Coplanar Grid Detector Design and Results

One drawback of the coplanar grid CZT detector has been its small size on a single crystal. That is, the efficiency for detecting gamma-rays using this type of detector is relatively low in comparison to NaI(Tl) scintillators or Ge semiconductor detectors because of its smaller volume. The crystal growth technology had limited the availability of single crystals to 2-3 cm<sup>3</sup> or smaller. However, recent advances in crystal growth technology have allowed the possibility for producing larger crystal sizes. In this study, a large volume crystal was purchased from Yinnel Tech with initial dimensions of 32 mm  $\times$  31 mm  $\times$  17 mm. The crystal was fabricated into a detector by BSI. The final detector size was 30 mm  $\times$  30.5 mm  $\times$  12 mm, which is a volume nearly a factor of 5 greater than any CZT detector developed by our group.

#### 6.1 Multi-pair coplanar grid concept

The multi-pair coplanar grid design was conceptualized as a means to employ the coplanar grid readout technique for a larger volume detector. A well known drawback to the coplanar grid system is the high degree of noise due to the leakage current and capacitance between the grids. Therefore, it is believed that scaling the grid electrodes to any arbitrarily large size would likely result in a poor performing detector, since the noise would also scale with the grid size. A solution to this

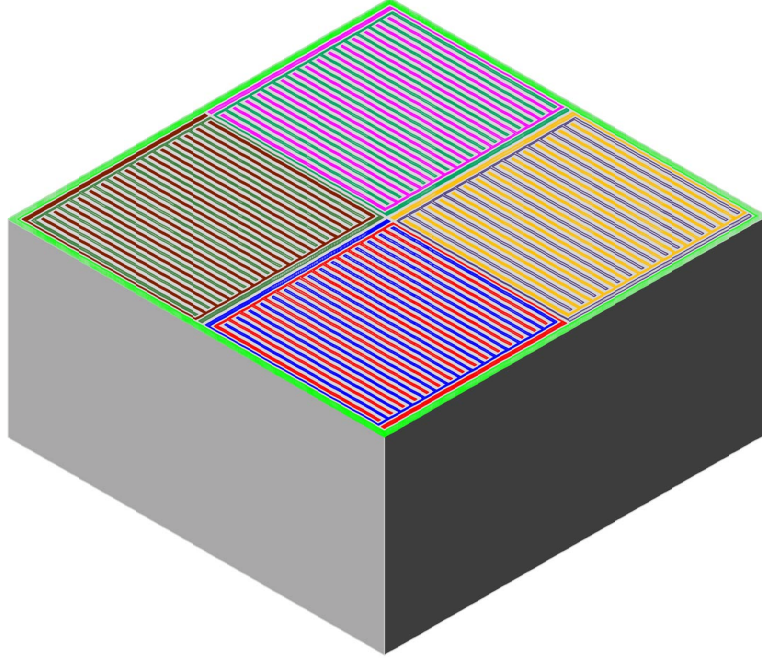


Figure 6.1: Illustration of the multi-pair coplanar grid design. This design consists of 4 sets of grid pairs surrounded by a single boundary electrode (shown in the green). The multi-pair coplanar electrodes were placed on both the top and bottom of the crystal. The anode surface area is  $30 \text{ mm} \times 30.5 \text{ mm}$  and the final crystal thickness was 12 mm.

problem is to employ 4 independent grids, divided into 4 quadrants, surrounded by a single boundary electrode as shown in Figure 6.1. By employing this configuration, signals can be read out from each grid separately and processed independently.

As mentioned, 4 coplanar grid pairs were used, as opposed to a single grid pair, because the noise performance should be better in the former case. This is because the capacitance between the electrodes will increase for the single coplanar grid case due to the surface area of the electrodes being 4 times greater. Increased capacitance will lead to larger series noise [1], and hence poorer spectroscopic performance. Another advantage of using 4 coplanar grid pairs is the reduced leakage current between each grid pair, since using a single grid pair will result in 4 times greater leakage current (summing the leakage currents from each of the 4 coplanar grids). Because of the very narrow spacing of coplanar grid detectors, leakage current can

be a dominant source of noise in the device. Larger leakage current will lead to greater parallel noise [1]. In addition, another unique aspect of this design is that we chose to surround all 4 coplanar grid pairs by a single boundary electrode. This was done rather than surrounding each grid pair by its own boundary electrode. As discussed in Chapter III, the purpose of the boundary electrode is two-fold. First, it helps to absorb excess leakage current from the sides of the detector. Second, it helps to make the weighting potentials of the collecting and noncollecting anodes more uniform, since the boundary conditions along the periphery of the device are forced to be consistent. Both of these conditions are met in the multi-pair coplanar grid design we chose. The boundary electrode in our design adjoins with the edge of the detector, hence side surface leakage current will be absorbed. In addition, if we consider any of the grid pairs in Figure 6.1, two sides will always border a boundary electrode. The other two sides will border the neighboring coplanar grid pairs. When calculating the weighting potential of either coplanar grid, the potential of the electrodes surrounding the coplanar grid will always be 0. Hence the neighboring coplanar grid pairs will act the same as the boundary electrode in the simple generation 3 coplanar grid design shown in Figure 3.2. Using a single boundary electrode has an added advantage. This is because the neighboring grid pairs can be used to sense transient signals. When processed properly, these signals can provide more uniform detector response. This effect will be discussed further in this section.

Using 4 coplanar grid pairs will result in some added complexity to the readout, since there will be 4 subtraction circuit signals to deal with. If a full energy deposition occurs under a single quadrant, it may be necessary to only read out the signal from the grid pair corresponding to this quadrant while the noise from the other 3 grid pairs can be ignored (Note: there is a caveat to this which will be discussed later

in this section). This would equate to better noise performance in comparison to employing a single coplanar grid pair on the anode surface. For the scenario in which interactions occur under multiple grid pairs, a different technique should be employed. In this case, the subtracted signal should be taken independently for each grid pair and then simply summed together. This will give the total charge induced on the 4 grid pairs, which will be a function of the total energy deposited. So, for this method to be realized, a signal threshold must be set in the readout software to indicate when an interaction occurs under a particular grid pair.

Another key feature of this detector is that only one single crystal of CZT was used, instead of 4 separate CZT crystals. We chose to use just one crystal because we have always observed that the best performance for all detectors occurs in the center of the device, where the weighting potential nonuniformity is a minimum. This was made evident in the radial spectrum in Figure 4.6(c). If the degradation of energy resolution due to nonuniform weighting potential can be limited only in the region very close to the periphery of the detector, a greater fraction of the detector volume will have better weighting potential uniformity rather than if 4 separate detectors are employed. By reading out signals from any of the grid pairs concurrently, and processing the signals properly, simulations showed that the effects of charge sharing, in which a portion of the electron cloud originally formed gets collected by multiple grid pairs, can be compensated. Charge sharing happens when an event occurs somewhere in the vicinity of the border region of two coplanar grid pairs, where the nonuniformity of the differential weighting potential of any single grid pair is worst. By just summing signals from neighboring pairs, the total signal can be nearly proportional to the total charge deposited. This is because the response of the detector in the border region is more uniform when summing the coplanar grid



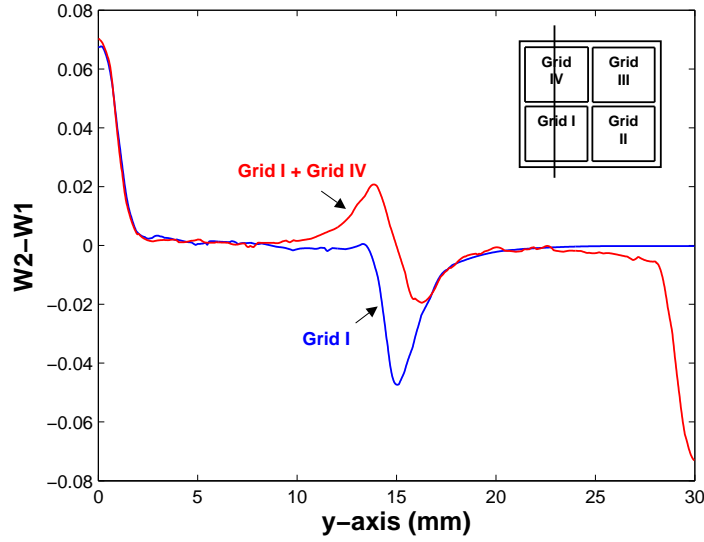


Figure 6.2: Plot of the weighting potential 1.25 mm from the anode surface along a line depicted in the inlaid figure. The grid I data (blue) is the weighting potential of the subtracted grid I signal. The grid I + grid IV data (red) is the resulting weighting potential when the subtracted signal from grids I and IV are added together. This plot illustrates that the weighting potential is more uniform in the border region ( $y = 10 \rightarrow 20$ ) for the summed grid case than it is for the single grid case.

signals together for neighboring grid pairs. This effect is illustrated by plotting the weighting potential data for the multi-pair detector in Figure 6.2. In addition, it is believed that this design can provide some radial position information. This is because we can utilize the signals from the neighboring grid pairs in addition to calculating the radial position of the interaction. By incorporating these two sets of information, we should be able to better characterize in which radial sector an event occurs. This position sensing algorithm may prove to be very useful, especially when trying to diagnose problem regions in the crystal.

The design of the multi-pair coplanar grid was carried out using Maxwell. Employing the 3rd-generation coplanar grid design and adapting it to the multi-pair concept, a variety of different designs were modeled. The optimum design was obtained by minimizing the weighting potential of the subtracted signal at a specific depth within the device where the weighting potential nonuniformity is generally

most severe, which was 1.25 mm from the anode surface. As a means to compare different designs, we used the same figure of merit (FOM) value as given in Equation 3.1. For these simulations, the subtracted signal weighting potential was calculated for only one grid pair at a time. That is, for one quadrant of the detector. Hence, the FOM was calculated only underneath the quadrant of interest. Our goal was to minimize this FOM in order to make the detector response as uniform as possible.

## 6.2 Detector evaluation

The large volume detector was made using a CZT crystal purchased from Yinnel Tech with initial dimensions of 32 mm  $\times$  31 mm  $\times$  17 mm. The crystal was then fabricated into a detector by BSI using our multi-pair coplanar grid design. Coplanar grids were fabricated on both sides of the detector because this would give us added flexibility to select which side of the detector is to be operated as the cathode and which side is to be operated as the anode. This is beneficial, because in Section 4.3.3, we found that the detector performed significantly better when one particular side was biased as the anode. The original goal for this detector was to construct a 15 mm thick device. However, due to early breakdown and low surface resistivity between coplanar grid anodes, multiple fabrication processes were carried out, each time resulting in some material loss. The final detector size was 30 mm  $\times$  30.5 mm  $\times$  12 mm. A picture of the actual detector without the aluminum housing cover is shown in Figure 6.3.

### 6.2.1 Low surface resistance and high voltage breakdown

The first measurement conducted was that of the inter-grid resistance. Just like the simple coplanar grid detectors discussed in Section 4.3, this detector was labeled as side ‘A’ and side ‘B’. The resistance between the grids on side ‘A’ was  $\sim 60$  M $\Omega$ s

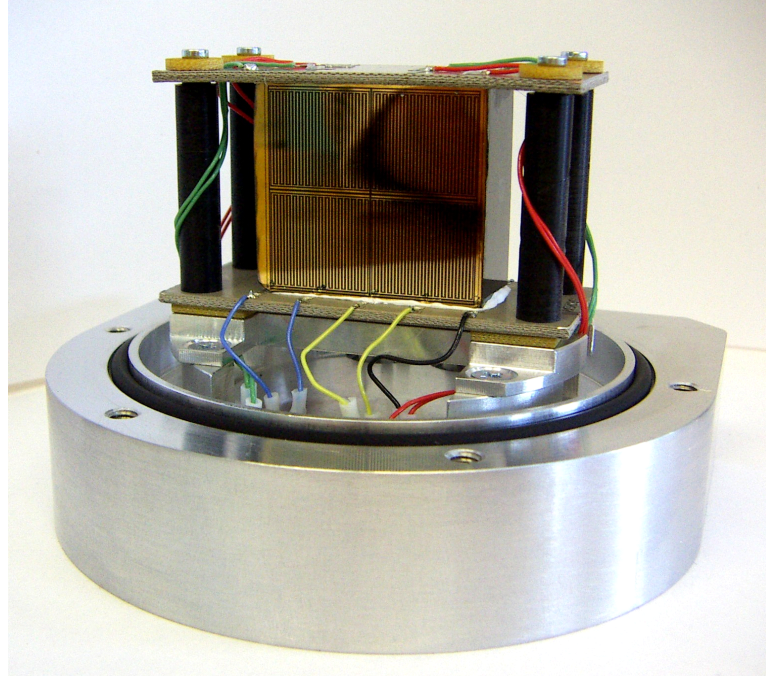


Figure 6.3: A view of one of the anode surfaces for the multi-pair coplanar grid detector. The electrodes are color coded to a particular color hook-up wire such that the electrodes can be distinguished properly biased.

and on side ‘B’ was  $\sim 110$  M $\Omega$ s. This is about a factor of 10 lower than that of the previous coplanar grid CdZnTe detectors, considering the area ( $15\text{ mm} \times 15\text{ mm}$ ) and pitch are almost the same on each grid pair. Side ‘B’ with the higher resistance was selected as the anode side. We then biased the detector to 1000 V, when breakdown was observed on the cathode. The phenomenon of breakdown includes anomalously large pulses and large fluctuations in the baseline of the preamplifier output. The gamma-ray signal was overwhelmed by large noise under breakdown conditions.

In order to isolate roughly where the poor region of the detector was located, we probed the signals from each of the grids individually on the cathode side. By doing this, it was found that the poor region was located under quadrants III and IV and also under a portion of the boundary electrode as illustrated in Figure 6.4. It was determined through further testing that grids I and II on the anode side could be safely operated at 1700 V. Hence, coplanar signals can be read out for grids I and II

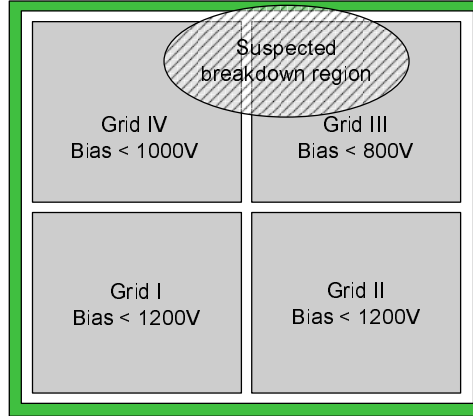


Figure 6.4: Illustration of the breakdown region relative to the grids on the cathode side. Operation of the detector was limited to 1200 V for grids I and II on the cathode side due to the large noise. However, the corresponding grids I and II on the anode side could be operated at 1700 V with stable behavior. This indicates that the breakdown region may be located closer to the cathode side.

at this bias without excessively large noise.

### 6.2.2 Biasing configuration and signal readout method

The multi-pair coplanar grid detector should be biased in a methodical fashion in order to achieve the best possible operating conditions. Namely, the anode strips should always be alternating between collecting anode and noncollecting anode. By nature of the single coplanar grid design, this is trivial to achieve. However, when biasing 4 separate coplanar grids, then care must be taken to ensure that neighboring strips never have the same potential. The proper biasing configuration is shown in Figure 6.5. There are two main reasons why we want to operate the detector in such a fashion. First, it will help to limit the effects of charge sharing in the border region between two adjacent sets of coplanar grid pairs. This is because the electrons that are formed in the vicinity of the border region will tend to get steered toward the collecting anode at the periphery, which will correspond to either of the grid pairs. Second, in order to properly compensate for edge effects, as discussed in Section 6.1, it is necessary that the subtracted signal weighting potentials compensate themselves

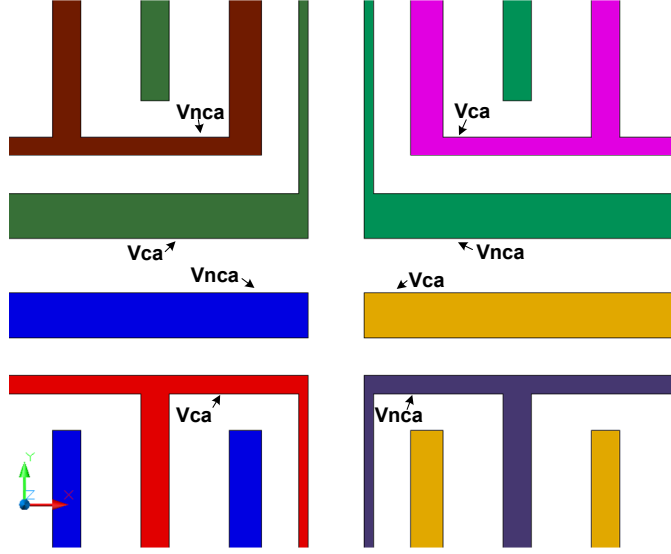


Figure 6.5: A cut-out illustration of the multi-pair detector in the center of the device. This indicates the proper biasing of the detector such that the strips alternate between the collecting anode bias ( $V_{ca}$ ) and the noncollecting anode bias ( $V_{nca}$ ).

when summed together. This effect was illustrated in Figure 6.2. This can only be achieved when the two periphery strips in the border act as dissimilar electrodes. That is, one is a collecting anode and the other is a noncollecting anode.

Depth sensing is usually achieved on a coplanar grid detector by reading out the signals from the cathode  $C$  and anode  $A$ . By taking  $C/A$ , the depth of the interaction can be determined. However, for this detector the cathode signal becomes excessively noisy even at 1000 V due to high voltage breakdown on the cathode side. In order to resolve this limiting factor for detector operation, we used the sum anode signal. That is, by taking the sum of the collecting anode and noncollecting anode signals, an alternative depth sensing can be achieved. This new depth ratio is therefore determined by employing Equation 6.1

$$d = \frac{A_{ca} + A_{nca}}{A_{ca} - A_{nca}} \quad (6.1)$$

where  $A_{ca}$  and  $A_{nca}$  are the collecting anode signal and noncollecting anode signal, respectively.

A caveat to this depth sensing algorithm is that when reading out the sum signal for one grid pair only, edge effects will alter the induced charge on the sum signal. This effect will be more pronounced near the anode side of the detector and will cause events occurring at the same interaction depth to result in a larger sum signal if they occur along the periphery than if they occur in the center. Hence, events from the same depth may actually be placed in different depths in the spectrum, which would degrade the spectroscopic performance. Employing the sum signal as an alternative to the cathode signal will be evaluated further in Section 7.2. This effect can be reduced by using the sum signal for all the grid pairs and the boundary electrode. However, due to the excessively large noise for grids III and IV and the boundary electrode, this was not practical.

### 6.2.3 Spectroscopic performance

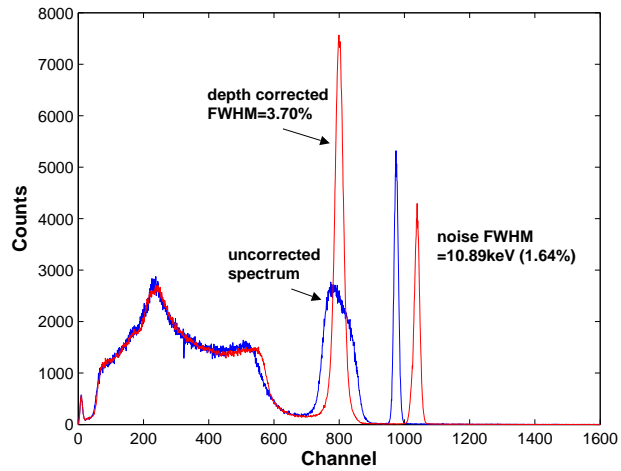
Some preliminary results for the large volume detector have been obtained. In the first measurement, the detector was biased at -1700 V on the cathode and 35 V intergrid. The signals were then read out from grid I. In the second measurement we used the same bias and read out the signals from grid II. For grid I, a depth corrected FWHM of 3.7% for 662 keV gamma-rays was achieved. The depth corrected spectrum along with the uncorrected spectrum is shown in Figure 6.6(a). For grid II the results were very similar; 3.74% FWHM. The depth sensing method helps to provide clues related to the properties of the detector, since we can obtain spectroscopic information versus the depth of the interaction. Figure 6.6(b) shows the relationship of energy resolution versus the depth number, where the detector was divided into about 30 total depth slices. We find that the resolution is worst in the middle of the device, ranging from depth index 12 to 23. This effect is not yet fully understood, but it is thought that this could be partially the result of Compton scattering in-

teractions. For Compton scatter events, the measured depth index is actually the centroid depth, weighted by the amount of energy deposited per interaction. Hence, the centroid depth tends to be near the middle of the detector and is very unlikely to be near either the cathode or anode surfaces. If the detector performance changes as a function of depth interaction, the performance as a result of multiple-interaction events could be degraded more significantly. The 3-D plot in Figure 6.6(c) shows the spectrum for each of the 30 individual slices of the detector with the source placed on the cathode side.

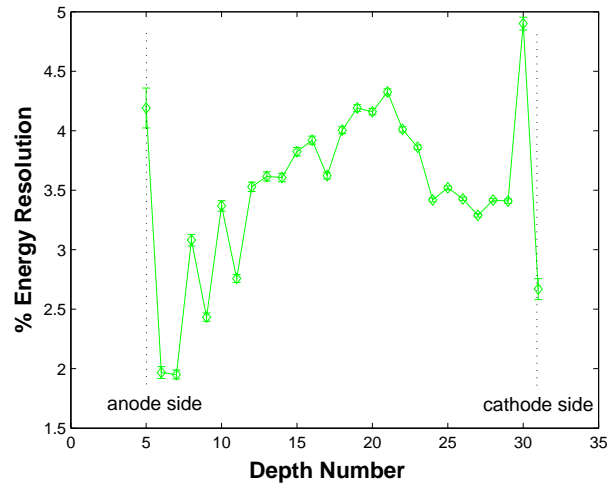
An important property for characterizing the transport of electrons in semiconductor materials is the  $\mu_e\tau_e$ . Measurements of the  $\mu_e\tau_e$  were taken using the method for single polarity charge sensing devices described in Section 4.3.2. Measuring the shift in the photopeak at two different bias voltages for 59.5 keV gamma-rays irradiated on the cathode side, it was determined from grid I that  $\mu_e\tau_e = 3.7 \times 10^{-3} \text{ cm}^2/\text{V}$  and from grid II  $\mu_e\tau_e = 3.8 \times 10^{-3} \text{ cm}^2/\text{V}$ . With these  $\mu_e\tau_e$  values, operating the detector at 1700 V bias would result in 20% electron trapping for cathode side events. The large amount of charge trapping in this device causes more statistical fluctuation in the signal and hence degraded resolution. As a general rule of thumb, we find that a good working coplanar grid detector requires charge trapping of less than 10%. Charge trapping could be reduced by increasing the bias. However, it is not possible on this detector due to high voltage breakdown.

#### 6.2.4 Further discussion

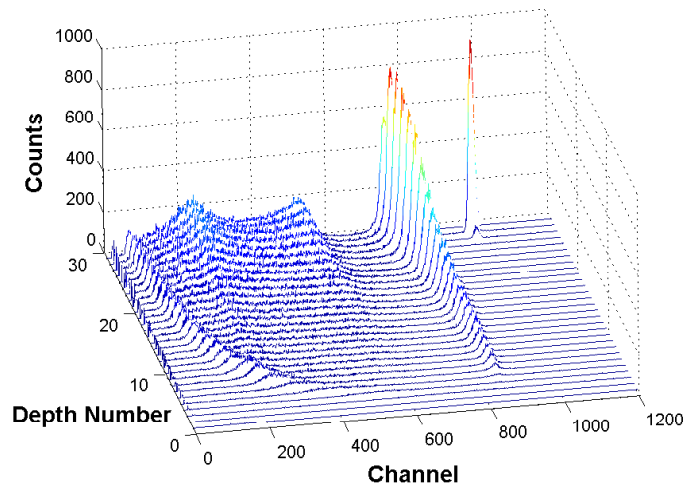
The results from the multi-pair detector fell well below our goal of  $< 2\%$  energy resolution at 662 keV. Only 2 out of the 4 coplanar grids could even register a spectrum due to excessively large noise caused by detector breakdown. Of the 2 working regions, the spectroscopic performance was deemed to be less than ideal.



(a) The blue data is the uncorrected spectrum and the red data is the depth corrected spectrum.



(b) Energy resolution as a function of the gamma-ray interaction depth.



(c) Spectrum at each depth slice.

Figure 6.6: Large volume detector data from grid I only using a 662 keV gamma-ray source. This data was acquired with a cathode bias of -1700 V and a noncollecting anode bias of -35 V. The data indicates that the energy resolution is poorest near the middle of the device.



However, from the discussion in Section 6.2 one can reasonably conclude that the limitation for this detector is not caused by the multi-pair coplanar grid design itself. The effects of low intergrid resistance, detector breakdown on the cathode and anode sides, and low  $\mu_e\tau_e$  all suggest that the limiting factor can be traced to the material properties and/or the detector fabrication. These results are in fact promising, since we feel that the the multi-pair coplanar grid design concept is still very much valid. In fact, it is strongly believed that if we could build a detector using a crystal with similar properties to that used in the BSI CZT2-4-2 detector (Section 4.3), our goal of  $< 2\%$  energy resolution, with much greater detection efficiency, could be achieved. Currently, it appears that the CZT crystal growth technology has not yet caught up with the demands set by the users.

## CHAPTER VII

### Other Factors Affecting Performance

Much of the emphasis so far in this dissertation has been placed on the proper readout of signals as well as optimization of the coplanar grid design. It has been made evident that these factors play a large role in determining the coplanar grid CZT detector performance. However, in addition to these, there are a number of other factors that play an important role in determining the performance characteristics of these detectors. One such factor that has lead to some interesting ramifications is the temperature effects on CZT. Yet another which can affect performance is the method by which depth sensing is accomplished. In addition, simulation tools can be used to quantify performance degrading effects such as weighting potential nonuniformity and electron trapping. Of course, this list is a somewhat limited view of all the factors affecting performance, since crystal growth and detector fabrication techniques have shown to greatly alter, for better or for worse, the detector characteristics. However, consistent with the rest of this dissertation, we focus on the observations that were made, through experimentation and simulation, of these detectors and attempt to elucidate these observations.

## 7.1 Temperature effects on CZT

There is wide-spread interest in the scientific community to characterize the performance of CZT detectors for low temperature environments such as those found on Mars. Surprisingly, little study has been done on the temperature effects of CZT [70,71]. To accomplish this, we used a temperature chamber that could easily reach temperatures down to  $-30^{\circ}\text{C}$ . The detector box, which includes the detector, preamplifier electronics, and the subtraction circuit, was placed inside the chamber. The biasing and signal cables were fed through a hole on the side of the chamber. Care was taken to reduce the concentration of water vapor surrounding the detector box which could possibly lead to water condensation on the electronics. This was done by supplying a flow of dry  $\text{N}_2$  gas into the chamber as well as placing containers of desiccant inside the chamber. Energy spectra were taken during the cooling cycle for temperatures of  $20^{\circ}\text{C}$ ,  $10^{\circ}\text{C}$ ,  $5^{\circ}\text{C}$ ,  $-5^{\circ}\text{C}$ ,  $-10^{\circ}\text{C}$ ,  $-20^{\circ}\text{C}$ , and  $-30^{\circ}\text{C}$ . Spectra were also taken during the warming cycle. In addition, we conducted measurements of the  $\mu_e\tau_e$  product for each temperature setting. An independent set of measurements were performed, which were taken at a later time, to characterize the  $\mu_e$  value at each temperature setting.

### 7.1.1 Results and evaluation for temperature study

The temperature study was carried out for both the eV Products detector MO2 2-2 square and the BSI detector CZT2-4-2. Using the depth sensing method for electron trapping compensation, we acquired energy spectra at each temperature setting. The results for the eV Products detector are displayed in Figure 7.1 and that for the BSI detector are displayed in Figure 7.2 [62]. For the eV Products detector, we observed the best energy resolution at  $5^{\circ}\text{C}$  of 2.1%. Below this temperature, continuously

degrading energy resolution was observed down to  $-20^{\circ}\text{C}$  with a value of 5.5%. A complete loss of spectral information was observed at  $-30^{\circ}\text{C}$ . The electronic noise was determined by the pulser FWHM and it was found that the noise reduced as a function of decreasing temperature, even at  $-30^{\circ}\text{C}$ . For the BSI detector, we observed the best energy resolution at  $20^{\circ}\text{C}$  of 2.4%. The poorer energy resolution observed at room temperature ( $20^{\circ}\text{C}$ ) during this study, in comparison to previous room-temperature measurements, was most likely a cause of the vibrational effects of the temperature chamber. Worsening spectral performance was observed as a function of decreasing temperature with a resolution of 7.0% at  $-20^{\circ}\text{C}$ . This detector also resulted in a breakdown in performance at  $-30^{\circ}\text{C}$ .

In addition to the spectral performance of the detectors, an evaluation of the detector  $\mu_e\tau_e$  product as a function of temperature was carried out [62]. In this method, we determined the  $\mu_e\tau_e$  product values based on the photopeak shift observed between cathode side events and anode side events. This method is subject to some factors that could affect the precision of the measurement, including the possibility of a relative gain not exactly equal to 1. However, the relative change in the observed  $\mu_e\tau_e$  should still be valid. Hence, we applied this method at all operating temperatures and normalized it to the known room temperature  $\mu_e\tau_e$  product value. The data for both the eV Products detector and the BSI detector is displayed in Figure 7.3. For the eV Products detector we find that the  $\mu_e\tau_e$  achieves its maximum value at  $5^{\circ}\text{C}$ , where the energy resolution was observed to be the best, and then it falls off for decreasing temperature. For the BSI detector we find that the  $\mu_e\tau_e$  is the highest at  $20^{\circ}\text{C}$  and higher than that of the eV Products detector. However, there is a sharp fall-off in this value with reduced temperature such that it falls well below the eV Products detector at  $-20^{\circ}\text{C}$ . These findings are in good agreement with the spectral

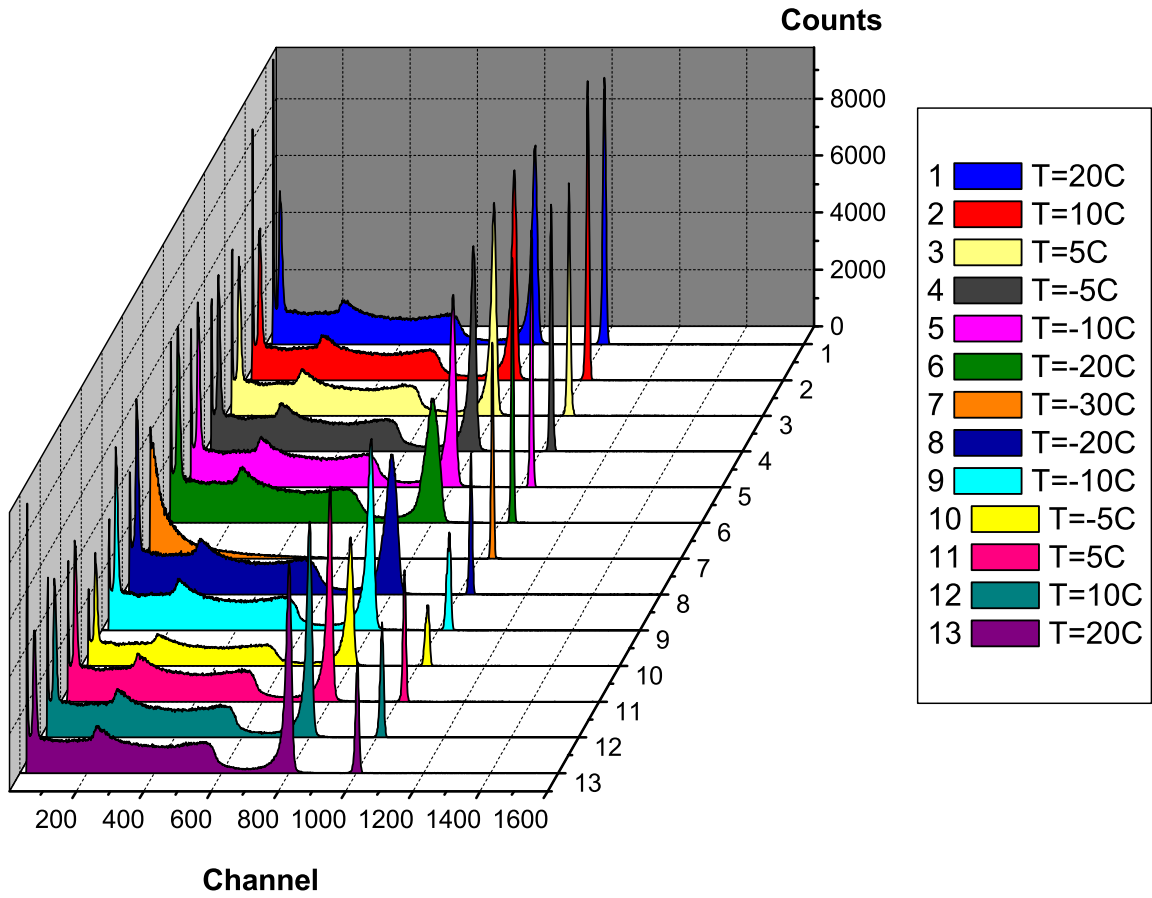


Figure 7.1: Spectrum taken with the eV Products detector MO2 2-2 square for each temperature setting using a 662 keV  $\gamma$ -ray source. Spectrum 1 (blue) is the initial temperature setting and spectrum 13 (purple) is the final measurement. The spectrum at -30°C is characterized as a low energy continuum.

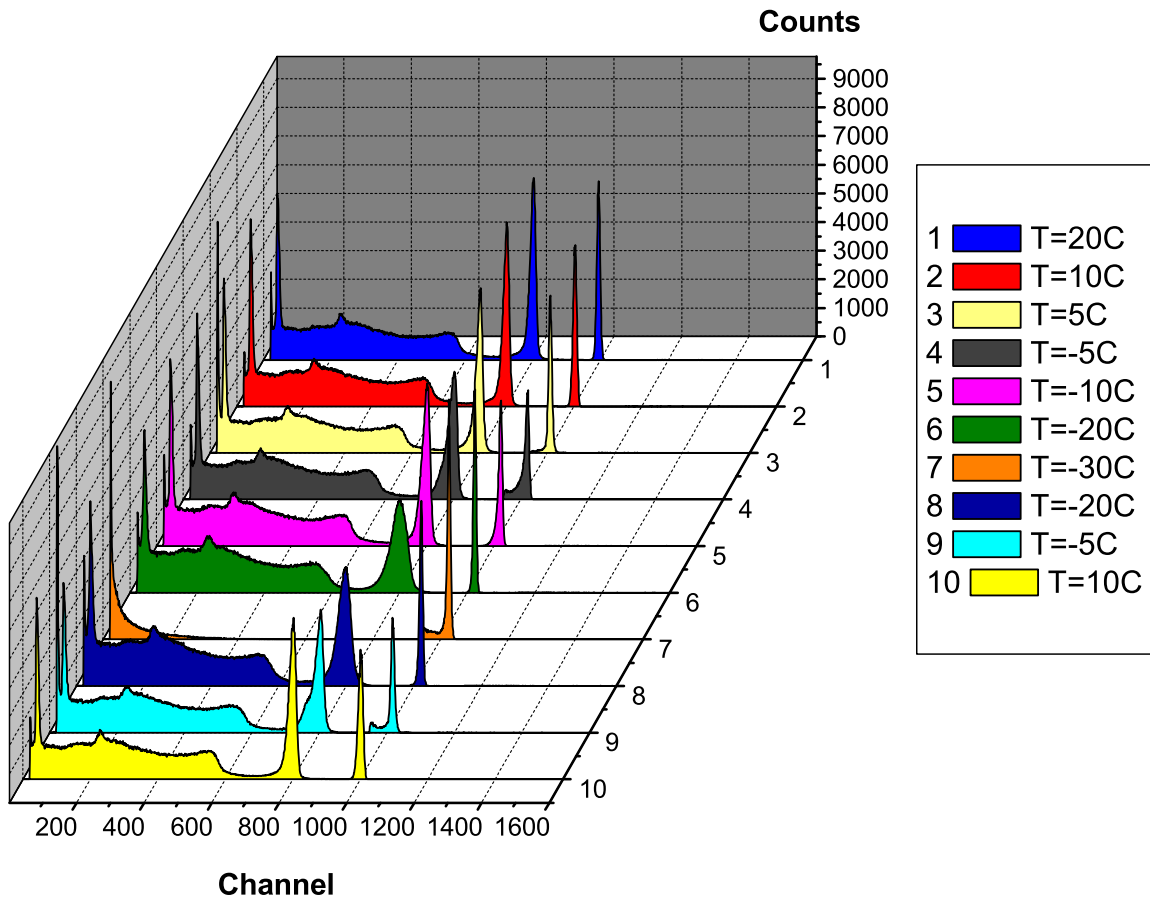


Figure 7.2: Ynnel Tech/BSI CZT2-4-2 detector spectrum taken at each temperature setting. For this case, spectrum 1 (blue) was the initial temperature setting and spectrum 10 (yellow) was the final one. The behavior is similar to the other detector, which also resulted in a low energy continuum for the -30°C temperature setting.

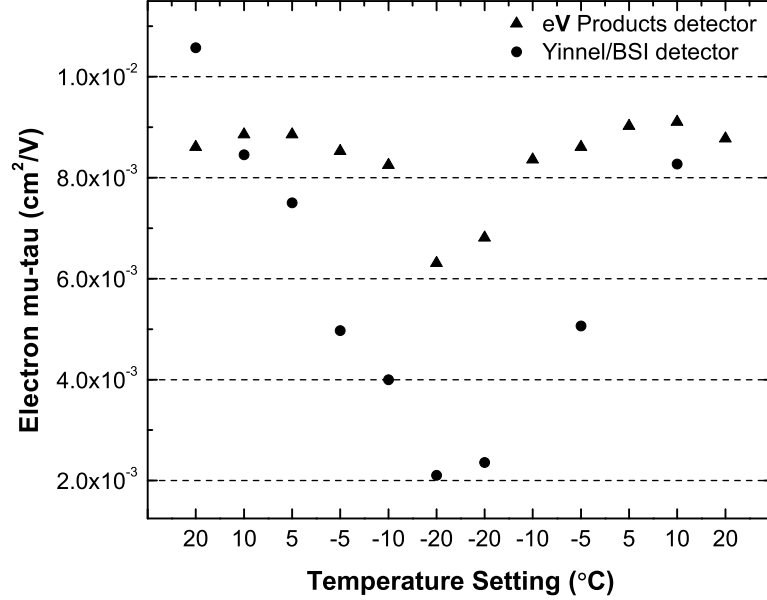


Figure 7.3:  $\mu_e \tau_e$  product values for two detectors as a function of operating temperature ( $20^\circ\text{C} \rightarrow 10^\circ\text{C} \rightarrow 5^\circ\text{C} \rightarrow -5^\circ\text{C} \rightarrow -10^\circ\text{C} \rightarrow -20^\circ\text{C}$ ). Measurements were repeated at each temperature for the eV Products detector while heating. Only three measurements were performed for the BSI detector during the heating cycle ( $-20^\circ\text{C} \rightarrow -5^\circ\text{C} \rightarrow 10^\circ\text{C}$ ).

behavior of the detectors as a function of temperature.

A separate set of measurements were carried out to determine the electron mobility value  $\mu_e$  for the BSI detector as a function of changing temperature. In this measurement, we acquired pulse waveforms for events originating near the cathode surface of the detector. By taking the rise time of such events we can determine the  $\mu_e$  value. Twenty measurements were taken at each temperature setting to determine the uncertainty of the measured value. The results are shown in Figure 7.4. We find that while cooling the detector the  $\mu_e$  increases about 14% from  $20^\circ\text{C}$  to  $-10^\circ\text{C}$ , which is what we would anticipate since the effect of reduced temperature would be a reduction in the crystalline lattice vibrations resulting in greater mobility because there would be fewer scatterings of the electron. However, we then observe a significant drop in the  $\mu_e$  at  $-20^\circ\text{C}$  in addition to greater uncertainty in the measurement. What we observed was that the pulse waveforms at  $-20^\circ\text{C}$  were either of two

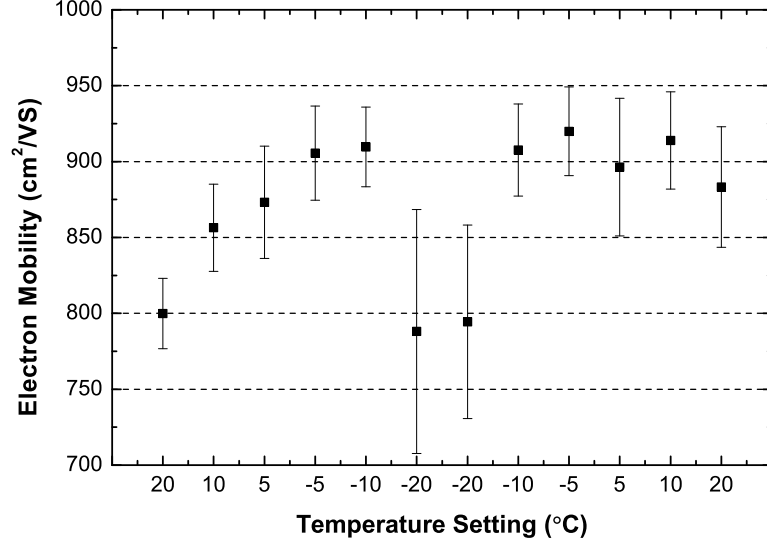
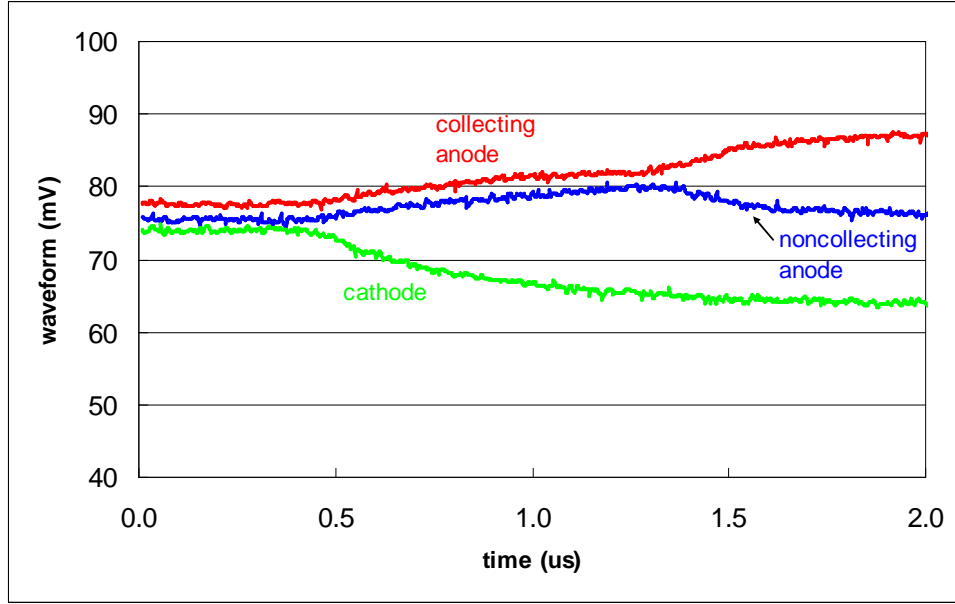


Figure 7.4: BSI CZT2-4-2 detector  $\mu_e$  values for changing temperature where the leftmost point is the initial measurement and the rightmost point is the final measurement.

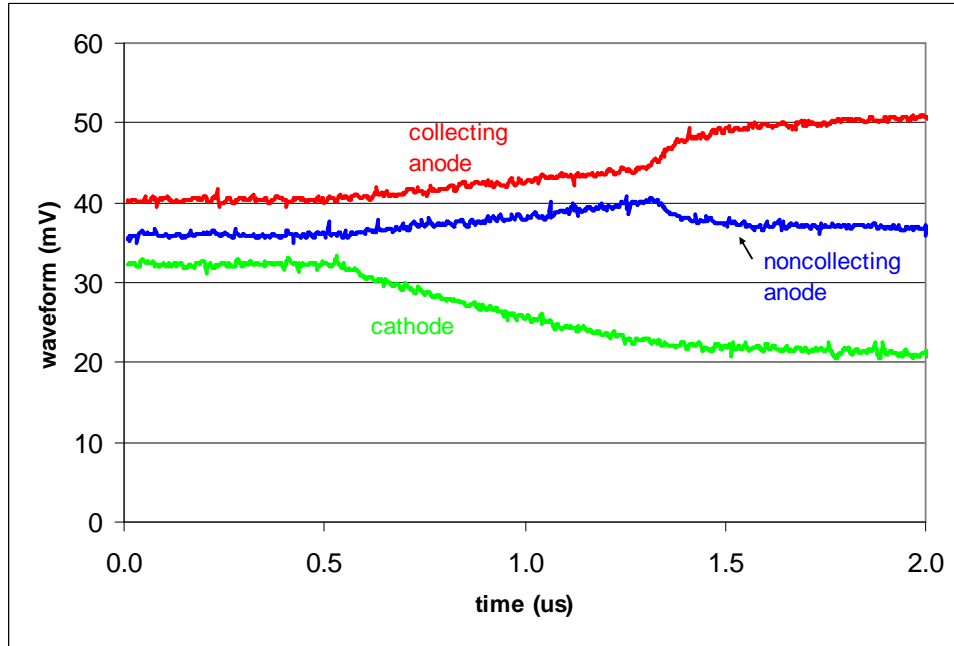
categories. The first category shown in Figure 7.5(a) consisted of pulses that had a rounding-off feature during the signal rise, resulting in pulses of longer duration with typical rise times of  $\sim 1\mu s$ . The second category shown in Figure 7.5(b) consisted of normal pulse waveforms with typical rise times of  $\sim 0.85\mu s$ . The distribution of waveforms at  $-20^\circ C$  was divided among these two categories fairly evenly, which gave way to a large uncertainty in the mean of the  $\mu_e$  value. During the heating cycle we observe a similar trend in the  $\mu_e$  from  $-20^\circ C$  to about  $5^\circ C$ . At  $10^\circ C$  and  $20^\circ C$  the  $\mu_e$  remains fairly constant, which could either be a result of the error associated with the measurement or the possibility that the chamber temperature was not held long enough such that the detector did not fully assume the operating conditions.

The effect of poorer spectral performance for temperatures below  $0^\circ C$  and a complete loss in spectral information at  $-30^\circ C$  is not yet fully understood. Examining the BSI detector data we find that the  $\mu_e \tau_e$  product reduces by a factor of  $\sim 5$  from  $20^\circ C$  to  $-20^\circ C$  and the  $\mu_e$  increases only slightly over the same temperature range. Hence, the electron lifetime  $\tau_e$  must also reduce by a factor of  $\sim 5$  over this temperature





(a) Anomalous waveform with a  $> 1\mu\text{s}$  risetime and a rounding-off feature.



(b) Normal waveform with  $\sim 0.85\mu\text{s}$  risetime.

Figure 7.5: Pulse waveforms obtained with the BSI CZT2-4-2 detector at  $-20^\circ\text{C}$ .

range. One possible theory to explain this observation is that the charge trapping levels become deeper with reduced temperature. That is, trapped charges are less likely to detrapp, resulting in a shorter lifetime. Another clue to help us understand the physical effects occurring in CZT at reduced temperature can be obtained from the pulse waveforms. At  $-20^{\circ}\text{C}$ , the previously mentioned first category pulse waveforms had a rounding-off effect in addition to longer rise times. This may be the result of longer electron detrapping times, since this would result in an elongated electron cloud giving way to the types of pulse waveforms we observed. The coplanar signal for events originating near the anode surface did not result in longer rise times at  $-20^{\circ}\text{C}$  since the electron drift distance would be reduced and hence would not be as affected by trapping and detrapping. At  $-30^{\circ}\text{C}$ , the anode pulses were much smaller in amplitude than what was observed for warmer temperature conditions. In many cases, the collecting and noncollecting anode signals were of the same polarity while the cathode signal was of the opposite polarity. This indicates to us that the electrons travel only a short distance within the bulk of the detector before becoming trapped.

Results from our temperature study agree very well with those obtained in a study done by Murray *et al.* [70]. In this study, two different crystals were tested and both were shown to have a complete loss of spectral information at temperatures below  $-20^{\circ}\text{C}$ . It was postulated that the reduced performance at low temperature was caused by space charge build-up, although no further analysis was done to verify this. In a more recent study by Amman *et al.* [72], detectors were tested at reduced temperature with crystals obtained from eV Products. These detectors all displayed better energy resolution with reduced temperature. One such detector resulted in more than 40% improvement in energy resolution, with 1.6% FWHM at 662 keV obtained

at 20°C and 0.9% FWHM obtained at -20°C. The improved resolution observed at reduced temperature was largely credited to reduced parallel noise, allowing for higher detector biasing and thus improved charge collection efficiency. In this study, a failure mode was also observed at -30°C. Pulse waveforms were recorded at this temperature and it was found that electron drift slowed considerably at a certain depth in the detector, which was linked to the existence of a weak electric field region. The authors stated that this effect most likely is the result of charge accumulation near the grid due to hole trapping. The observations from these studies, as well as in ours, are likely dependent on the particular CZT material used and the detector fabrication process. Hence, variations in detector performance for changing temperature between these studies are reasonable to find.

## 7.2 Depth sensing using summation signal

In this dissertation we have focused mainly on using the  $C/A$  ratio to calculate the depth of the gamma-ray interaction, where  $C$  is the cathode signal and  $A$  is the anode signal. However, other methods can also be used to accomplish depth sensing. One method involves using the timing information between the initial formation of the charge to the collection of the charge at the anodes to deduce the depth of interaction [26, 73]. Another method discussed in Section 6.2.2 involves using the sum anode signal as an alternative to the cathode signal. In this method, we used the sum of the collecting anode and noncollecting anode signals to calculate the interaction depth as done via Equation 6.1. This method proved to be very useful for the multi-pair coplanar grid detector because the cathode signal was excessively noisy for this device and could not be used. Therefore, the anode signals were instead used to achieve depth sensing. We observed, however, a reduction in the photopeak

area for decreasing depth number when using this method. This effect was studied further by conducting simulations and comparing to experimental data.

Two different methods for depth sensing were investigated in this study. One method involved using  $C/A$  and the other method involved using  $Sum/A$  where  $Sum = A_{ca} + A_{nca}$ . Experimental data using the BSI CZT2-4-1 detector is shown in Figure 7.6. The 3-D spectrum shown in Figure 7.6(a) was obtained by taking  $Sum/A$  to achieve depth sensing. The data shown in Figure 7.6(b) is a comparison of the photopeak area between the two different methods for depth sensing. It is clear that there was a reduction in the photopeak area near the anode side when employing  $Sum/A$  to determine the depth. Much more uniform response was obtained using  $C/A$ . We then used simulation techniques to simulate the detector response using both methods for depth sensing. Results from these simulations are shown in Figure 7.7. It is clear that the simulated data agrees with the experimental data very well. From this, we verified that the reduction in the photopeak area is due to edge effects in the  $Sum$  weighting potential as a result of the boundary electrode. The boundary electrode shown in Figure 3.2 surrounds the two inner coplanar anodes and will cause the weighting potential of  $Sum$  to decrease around the periphery. This is because the induced charge will be shared between the boundary electrode and the coplanar anodes. The reduced  $Sum$  weighting potential around the edge will cause the actual  $Sum$  signal to be greater around the periphery than in the center. This effect will become more severe near to the anodes, resulting in a significant portion of anode side events to have a greater depth value when using  $Sum/A$  than the true depth of the gamma-ray interaction. Hence, many events will be pushed toward the cathode side. The cathode signal, however, will be much more uniform as a function of lateral position for a given depth, because all of the electrodes on the cathode side are being

used. Hence, edge effects aren't as significant of a factor in this case, causing the photopeak area to be much more uniform as a function of depth.

### 7.3 Factors contributing to peak broadening

Any gamma-ray spectrum has a number of factors associated with it that lead to broadening of the photopeak. Many such factors related to the coplanar grid CZT detector have already been discussed in this dissertation. These include weighting potential nonuniformity, material nonuniformity, electronic noise, incomplete charge collection, Fano statistics leading to variations in the number of charge carriers produced, and electron trapping. Understanding each of these sources of peak broadening, ultimately resulting in energy resolution degradation, can be helpful in understanding which factors have the largest influence on detector performance.

The simulation techniques discussed in Chapter V were employed in order to quantify these sources of peak broadening. Each of the peak broadening factors included in our simulations can be added in one at a time in order to determine the contribution that each factor makes to the overall spectrum. We began by modeling the spectrum only including the effects of weighting potential. This was achieved by generating pulse waveforms in the MATLAB program without including the effects of electron trapping. A gamma-ray spectrum was then generated using Geant4 incorporating this waveform data. The FWHM of just the weighting potential component was determined to be 0.18% at 662 keV. The next step involved including electron trapping into the model, which is factored into the MATLAB waveform generation program. In order to completely model the effects of electron trapping, it is also necessary to include trapping statistics. This is included into the Geant4 program as discussed in Section 5.1. The total FWHM of the resulting spectrum

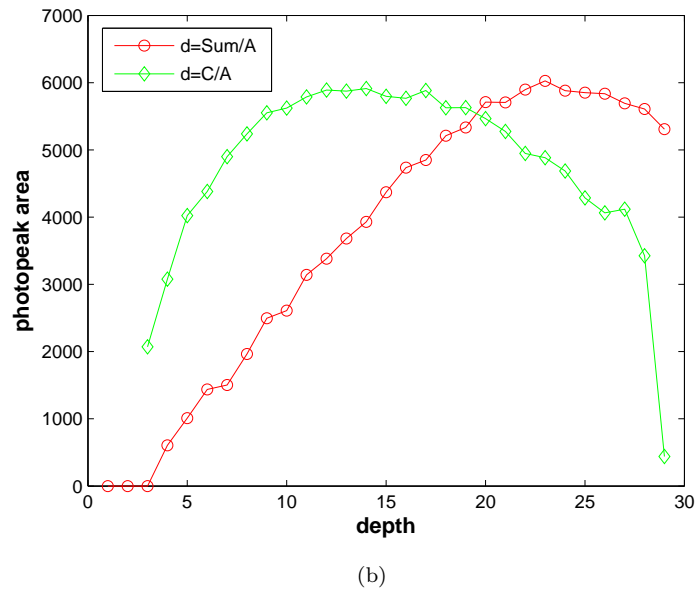
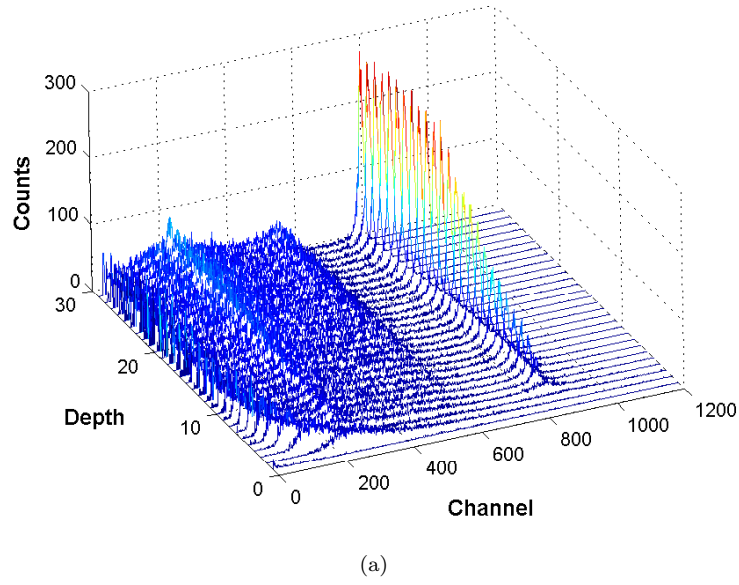
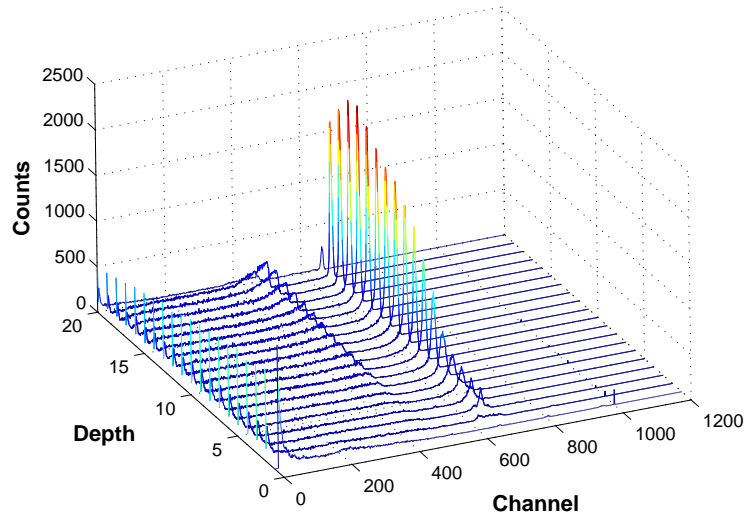
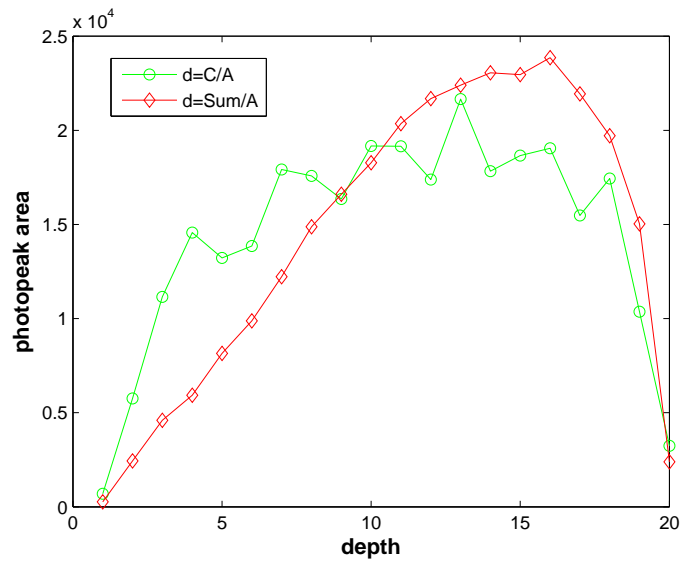


Figure 7.6: Experimental results for the BSI CZT2-4-1 detector where (a) is the 3-D depth spectrum obtained using  $d = \text{Sum}/A$  and (b) gives a comparison in the photopeak area for both depth sensing methods.



(a)



(b)

Figure 7.7: Simulation results where (a) is the 3-D depth spectrum obtained by taking  $d=Sum/A$  and (b) gives a comparison of the peak area. The simulation data agrees with the experimental data very well.

Table 7.1: Results quantifying each component of peak broadening included into the model. The data in the middle shows the total spectrum % FWHM at 662 keV after adding in each component listed in sequential order. The data along the right details the % FWHM for each of these components individually.

<b>peak broadening factors</b>	<b>% FWHM for total spectrum</b>	<b>% FWHM for each component</b>
weighting potential	0.18	0.18
electron trapping	0.63	0.60
Fano statistics	0.67	0.22
electronic noise	1.37	1.19

is 0.63% at 662 keV. If we assume this source of peak broadening to be symmetric and independent from all other sources, it follows that the FWHM contribution due to electron trapping is  $\sqrt{(0.63\%)^2 - (0.18\%)^2} = 0.60\%$ . The next factor included into the model was Fano statistics, which was included in the Geant4 code. By a similar calculation as was done above, it was determined that this source contributed a FWHM of 0.22% at 662 keV to the overall spectrum. The final cause of peak broadening that was included into the simulation was that due to electronic noise. The FWHM due to the electronic noise component was found again by taking the difference in quadrature, which was determined to be 1.19%. A summary of these results is given in Table 7.1.

The data given in Table 7.1 is useful in determining which factors have the greatest influence toward the detector spectroscopic performance. We find that the weighting potential for our particular design has just a small effect on the overall performance, which provides further affirmation that our design is a favorable one. If, instead, we conducted these simulations using a generation 1 or 2 design, this component would be much larger. It can be seen that electron trapping has a significant impact on the energy resolution. This is because electron trapping will lead to variations in the amount of charge arriving on the anode due to varying path lengths. The path length of the electron not only varies as a function of depth, but also as a function of lateral



position. That is, electrons formed directly underneath a noncollecting anode will have a greater distance to travel as they drift toward the collecting anode than those electrons formed directly underneath the collecting anode. This will then lead to greater electron trapping for those electrons generated underneath the noncollecting anode, ultimately resulting in variations in the charge induction efficiency, and hence a source of energy resolution degradation. Another effect associated with electron trapping is the variation in the number of electrons trapped, which we can assume to be governed by Poisson statistics. However, this effect will be quite small, resulting in a contribution of  $\sim 0.2\%$  FWHM at 662 keV. The effect of Fano statistics is more important for HPGe detectors than it is for coplanar grid CZT detectors. However, it still adds to the overall energy resolution of the device. We find that electronic noise has the greatest influence in our model on spectroscopic performance. Interestingly, the noise that was set in the simulation was  $7 \text{ keV} = 1.06\%$  FWHM at 662 keV, while the noise determined in the simulation was  $1.19\%$ . This discrepancy exists because the noise included into our model is Gaussian. However, because of factors leading to low energy tailing, such as incomplete charge collection, the original spectrum to which we are adding the noise is not truly Gaussian. Hence, the noise component does not get perfectly added in quadrature. In these calculations we assumed each factor adds in quadrature to all other factors, which is an approximation. Hence, discrepancies in the measured FWHM and the true FWHM will exist.

## CHAPTER VIII

### Summary and Future Work

Gamma-ray spectroscopy has undergone many advancements in the last two decades, many of which have been in the field of room-temperature semiconductor detectors. The breakthroughs that have been made in this technology have coincided extremely well with the demands of the users. That is, the emphasis is now being placed on portable instrumentation with good gamma-ray detection efficiency and good energy resolution. When imaging capabilities are not required, coplanar grid CZT can accomplish these tasks very nicely. The key advantage of this detection method is the simplicity by which coplanar grid signals can be read out and processed. In the simplest configuration, one can achieve all of these requirements with just a power supply, 2 charge sensitive preamplifiers, a subtraction circuit with a relative gain adjustment, an amplifier, and a multichannel analyzer. Slightly more complex arrangements involving a peak-hold circuit, a DAQ card, and custom programmed LabVIEW software are required for more sophisticated sensing algorithms, but are still relatively simple to implement. Because of its simple readout approach, in combination with the good gamma-ray detection properties of CZT, coplanar grid CZT has become a very attractive contender in the field of gamma-ray spectroscopy. Users whose detection applications require near to, or less than, 2% energy resolution

at 662 keV in a room temperature device should consider employment of this type of detector.

## 8.1 Summary of results

Coplanar grid CZT detectors have a fairly recent history dating back to 1994 [22]. Although the foundation for this technology was well grounded before this dissertation work began, we have gained more knowledge and have made significant progress for ultimately rendering detectors with good spectroscopic performance. This research work began with a study to characterize the performance of two  $1.5 \times 1.5 \times 1.0 \text{ cm}^3$  detectors and one cylindrical detector 1.5 cm in diameter and 1.0 cm in length, all of which were manufactured by eV Products. These detectors were fabricated using a previously developed generation 3 coplanar grid design. Then, two different electron trapping compensation methods were compared, the relative gain method and the depth sensing method. As predicted, the best results were achieved using the depth sensing method, which resulted in energy resolutions between 2.0% and 2.1% FWHM at 662 keV for one of the detectors. Using the depth sensing method, we found that the energy resolution as a function of interaction depth was much more uniform on the generation 3 detector than it had been on the generation 2 detector. This is because the generation 3 coplanar grid design was optimized for improved weighting potential uniformity near the anode surface. Another means by which to assess the performance of coplanar grid detectors is through radial sensing. Using this sensing technique, we can plot the spectra as a function of radial position at a given depth within the device. This method can be used as a diagnostic tool to compare the uniformity in response for different coplanar grid designs. It was found that the resolution degraded much less severely as a function of radial position

employing the generation 3 design, which was further testament that the generation 3 design is superior to the generation 2 design.

Two new detectors were then produced using Yinnel Tech, Inc., crystals and fabricated by BSI, Ltd., with a size of  $1.5 \times 1.5 \times 0.9 \text{ cm}^3$  and  $1.5 \times 1.5 \times 0.95 \text{ cm}^3$ . These detectors were constructed employing a new generation 3 coplanar grid design. The design was optimized with the Maxwell electrostatic finite element analysis software package under a certain set of design restrictions specified by BSI. The final design was chosen by balancing the effects of detector capacitance with weighting potential uniformity, both of which play a significant role in determining the final detector performance. For these detectors, coplanar grids were constructed on both sides of the crystal, allowing one the flexibility to select which of these sides is to be operated as the anode. Using the relative gain method, an energy resolution of 1.65% FWHM at 662 keV was recorded for one of the detectors. The  $\mu_e \tau_e$  product for this detector was  $1.13 \times 10^{-2} \text{ cm}^2/\text{V}$ , which is traditionally a high value for  $\mu_e \tau_e$  and helping to account for the very good spectroscopic performance that was measured. The results were slightly poorer using the depth sensing method with a FWHM of 1.75% at 662 keV, which was counter to expectations that the depth sensing method should be the superior method for electron trapping compensation. However, for the second detector, the best energy resolution result of 1.86% at 662 keV was achieved using the depth sensing method. Employing the relative gain method, the resolution was measured to be 1.99% at 662 keV. Measurements for these detectors were also taken for opposite biasing polarities, such that the cathode and anode biases were reversed. Under this condition, the best resolution achieved was 6.8% at 662 keV. The dramatic degradation observed when the biasing was reversed indicates that the material properties are asymmetric. In general, these findings reveal that it is

very important to determine the best side for anode operation to achieve optimal performance.

Results from a new large volume coplanar grid detector with size  $30 \times 30.5 \times 12 \text{ mm}^3$  were reported. With this detector, the motivation was to improve the gamma-ray detection efficiency while maintaining the good energy resolution observed in the smaller volume detectors. A novel coplanar grid design was employed, called the multi-pair coplanar grid design, consisting of an array of 4 coplanar grid anodes on a single CZT crystal. This design was used rather than just one coplanar grid, because it is believed that the noise performance should be significantly better for the 4-grid case due to smaller capacitance and leakage current. Testing of this detector was carried out and significant breakdown was observed for the cathode signals at a low bias voltage. On the anode side, it was determined that two of the four grids remained stable until 1700 V. Hence, only the anode side could be used to acquire spectra. Depth information was determined using the sum anode signal as an alternative to the cathode signal, such that  $d = \text{Sum}/A$ . Employing this depth sensing method, spectra were recorded under grid I and grid II. The energy resolution was approximately the same value for both grids of 3.7% FWHM at 662 keV. Measurements of the  $\mu_e \tau_e$  were also taken and found to be a low value of  $3.7 - 3.8 \times 10^{-3} \text{ cm}^2/\text{V}$ . The relatively low  $\mu_e \tau_e$  value, in combination with a small electric field due to biasing restrictions, results in  $\sim 20\%$  electron trapping for cathode side events. The large percentage of electron trapping causes more statistical fluctuations in the signal and hence degraded resolution. In general, it was determined that the most significant factors limiting the performance for the multi-pair coplanar grid detector were due to material and/or fabrication flaws. Therefore, it is believed that the design concept is still valid and could give rise to good performing

detectors with much larger detection efficiency.

Modeling of the coplanar grid CZT detector was conducted to better analyze questions that would be difficult to answer through experimentation alone. The simulation packages used in this study were Maxwell for modeling the signal induction process and Geant4 for modeling the physics of gamma-ray interactions. A  $1.5 \times 1.5 \times 1.0 \text{ cm}^3$  CZT detector employing the generation 3 coplanar grid design was modeled. A comparison study between the depth sensing method and the relative gain method for electron trapping compensation was done and it was determined that the depth sensing method resulted in better overall spectroscopic performance with a FWHM of 1.34% at 662 keV. However, the difference in energy resolution between these two methods was a small value of 0.06%. This observation was confirmed by just recording events within the periphery region of the detector and comparing results using both unity and non-unity relative gain values. No significant difference in energy resolution was observed between these two cases. These results correlate to a certain degree with experimental findings, since for the BSI detectors differences in energy resolution between the two electron trapping compensation methods were  $\sim 0.1\%$ . However, it is not yet evident why one detector in the experiment (BSI CZT2-4-2) resulted in better spectroscopic performance using the relative gain method.

Using these simulation tools, a study of the CZT surface effects was conducted. Two different surface boundary conditions were modeled, both employing a 600 nm oxide layer, one assuming a linearly varying potential difference between the anodes and the other allowing the oxide potential to remain floating, where no potential was assumed. A comparison was made between these two surface boundary conditions and it was observed that better electron collection resulted when the oxide layer was left floating. The floating case is analogous to a high surface resistance between the

anodes. It was found for this case that the potential at the surface has a convex shape, causing the electric field lines to focus toward the collecting anode. For this case, the critical bias at which complete electron collection takes place was found to be at a coplanar bias of 86 V. Simulated energy spectra were recorded, assuming a floating oxide layer, for two different coplanar biases of 43 V and 86 V. The effects of incomplete charge collection could be seen at 43 V, since this is below the critical bias. Comparisons were made to experimental data and similarities were observed, however discrepancies were also observed largely because these models did not include other important effects which could lead to peak broadening. These effects include material nonuniformities in addition to an oversimplified model of the noise, which did not account for changing bias. In addition, discrepancies may also exist because the surface boundary conditions may not be entirely accurate. Hence, other models should also be examined.

In this dissertation work, other factors affecting coplanar grid CZT detector performance were also explored, such as the temperature effects on CZT. This was an important study to conduct due to the increasing popularity of CZT and its potential uses in extreme temperature environments, such as those found on Mars. In this study, the spectroscopic performance of CZT in a low-temperature environment was evaluated. Two different detectors were tested, one from eV Products and the other from Yinnel Tech/BSI. The detectors were tested over a range of temperatures from 20°C down to -30°C. For the eV Products detector, the best energy resolution was observed at 5°C, corresponding to the temperature at which the  $\mu_e\tau_e$  product was measured to be the greatest. For the BSI detector, the best energy resolution was observed to be at 20°C, which also coincided with the largest  $\mu_e\tau_e$ . Both of these detectors resulted in a complete loss of spectral information at -30°C. A very

interesting observation in this study was that for the BSI detector, the  $\mu_e\tau_e$  product reduced by a factor of  $\sim 5$  from  $20^\circ\text{C}$  to  $-20^\circ\text{C}$  and the  $\mu_e$  increased only slightly over this temperature range. Hence, the electron lifetime must also reduce by a factor of  $\sim 5$  over this temperature range. It is thought that this is the result of deeper charge trapping levels with reducing temperature. The breakdown in performance observed for these detectors in low temperature environments has definite ramifications when considering CZT for such environments. Interestingly, whereas other detectors such as HPGe or Si(Li) must be operated in low temperature environments, this study indicates that CZT is truly a room temperature detection material, best operated at or near room temperature.

Another factor affecting spectroscopic performance is the manner by which depth sensing is achieved. Two different methods for depth sensing were compared, one using  $C/A$  and the other using  $Sum/A$ , where  $Sum$  is the summation of the collecting and noncollecting anode signals. Using the summation signal for depth sensing, a reduction in the photopeak area was observed in our experiment for decreasing depth indices (near to the anode side). This observation was confirmed through simulation techniques. When employing the cathode signal for depth sensing, the photopeak area remained much more uniform as a function of depth. It was determined that the effect observed using the summation signal was caused by edge effects in the weighting potential resulting in events from the same actual depth to be placed in different depths. Hence, the preferred method for depth sensing is through utilization of the cathode signal.

Finally, a study was conducted to determine the contribution that each source of peak broadening has on the overall spectrum. This information provides insight into the major causes of energy resolution degradation. Simulations were performed



by adding each source of peak broadening individually, which included weighting potential nonuniformity, electron trapping, Fano statistics, and electronic noise. It was found that weighting potential nonuniformity only contributes 0.18% FWHM at 662 keV to the spectrum. This is a testament to the well-done coplanar grid design employed in this study. The effect of electron trapping was found to have a significant influence on the overall detector energy resolution, with a FWHM contribution of 0.60%. This source of peak broadening is largely due to variations in the electron path length, both as a function of depth and as a function of lateral position, causing variations in charge collection. The largest source of peak broadening in our model is that due to electronic noise, which was determined to be 1.19% FWHM. This is an effect that is inherent to all coplanar grid detectors. However, this effect can be reduced through consideration of detector capacitance in the design as well as through better material surface passivation techniques to limit leakage current. Other factors will also have an influence on detector energy resolution, such as material nonuniformity, and should be included in future models.

## 8.2 Recommendations for future work

In this dissertation, spectroscopic results from a variety of coplanar grid CZT detectors were reported. From all the detectors tested, the best energy resolution recorded was 1.65% FWHM at 662 keV. The next best detector resulted in 1.86% FWHM at 662 keV. These results were impressive for the coplanar grid readout method, however they still lag well behind the performance observed for pixellated detectors. Using the 3-D readout technique on a pixellated CZT detector, an energy resolution of 0.93% at 662 keV has been reported [74]. Hence, a significant discrepancy exists in terms of spectroscopic performance between these two meth-

ods. One factor that helps to account for this discrepancy is the larger electronic noise for the coplanar grid readout technique. The lowest noise recorded for coplanar grid CZT was  $\sim 7$  keV FWHM, whereas the noise estimated for the pixellated detector was less than 4.5 keV FWHM. Hence, if we subtract the noise component from the original peak and recalculate the FWHM, we find that the intrinsic FWHM is  $\sqrt{(1.65\%)^2 - (1.06\%)^2} = 1.26\%$  for the coplanar grid detector, which is still well above the energy resolution of the pixellated detector. Therefore, differences in spectroscopic performance cannot be accounted for through noise alone. Another factor that could help to account for this discrepancy is the effect of material nonuniformities. It is well known that CZT crystals can suffer from defects, such as grain boundaries or Te-inclusions, such that the trapping probability can be significantly higher in certain regions of the detector [75]. Such defects will not only result in a variation in charge trapping as a function of depth, but also as a function of the lateral position. With the pixellated readout technique this variation can be accounted for to a large degree because of 3-D position sensitivity [76]. With the coplanar grid readout technique, compensation can only be done in 1-D. This limitation gives further advantage to the pixellated readout technique.

More analysis should be done to understand the aforementioned differences in performance between the pixellated readout technique and the coplanar grid readout technique. A study of this nature may help to provide further insight into the limitations of the coplanar grid readout method. The most accurate way to compare the performance of these methods would be to test both readout techniques on the same CZT crystal. This would entail two iterations of detector fabrications, one with coplanar grid anodes and the other with pixellated anodes. By allowing the crystal to remain consistent, this then will make for a much better comparison study.

Further insight can also be gained about these detectors by running better, more accurate, simulations. One effect that was neglected in the models discussed in this dissertation are material nonuniformities. This effect should be included in future simulations, since it was determined that this can have a significant impact on detector performance. This is not a trivial effect to include, however, since the physics of such defects are not yet well understood. For instance, studies have shown that Te-inclusions can have a diameter of  $\sim 20 \mu m$ , but their effects of increased electron trapping can extend well beyond their actual physical volume [75]. A good first approximation would be to assume a random distribution of these Te-inclusion sites with a density similar to that found in a typical CZT crystal. Any electrons that pass within  $25 \mu m$  of these sites will be permanently trapped. Such modeling would be done in the waveform generation program, in which the electron trajectory is calculated. Here, one would need to model an electron cloud drifting through the crystal. A conditional statement would be included into the code which states that if an electron is within a certain distance from a Te-inclusion, then that electron should be trapped. These calculations would need to be done for every electron within the cloud, which will be quite computationally intensive. Hence, such simulations could benefit greatly by employing the most powerful computers available to the user.

Future studies of the coplanar grid CZT detector could benefit by employing digital readout techniques for signal postprocessing. This would allow the user to have greater flexibility in how the signals are processed after the preamplifier stage. Hence, filtering could be done using a wide variety of digital filters and one wouldn't be limited by the filtering choices on the NIM shaping filter as used in this study. However, possibly a greater advantage to using digital readout techniques would be the ability to select and study particular types of events that occur in the detector.

For example, because of trapping sites in specific regions of the detector, one may observe a change in slope for the cathode signal due to significant trapping. These types of events would lead to energy resolution degradation and could be filtered out when using digital pulse processing techniques. Another advantage in using digital readout is that it would provide a much easier method to determine the electron mobility  $\mu_e$ . Previously, to measure the  $\mu_e$  it was necessary to record many pulse waveforms using an oscilloscope and selecting the waveforms with the longest rise times. Using digital techniques, this could be done in a more automated fashion, resulting in less error due to inconsistencies by the user in proper event selections.

Results from the multi-pair coplanar grid detector fell short of the goals that were set. However, it was established that the chief cause for the poor performance that was observed was not because of the design concept itself, but rather because of limitations in the crystal material or the detector fabrication process. As crystal growth methods and detector fabrication techniques mature, more consistent large volume detectors can be anticipated. Thus, another iteration of the multi-pair detector would be recommended when crystals of this size can be grown with suitable performance.

The multi-pair coplanar grid design used in our study consisted of 4 coplanar grid pairs in a  $2 \times 2$  array. This design was chosen based on the size of CZT crystal that was acquired. In theory, there should be no limit to the number of coplanar grid pairs used, since each pair can operate independently from all other pairs, similar to a pixellated detector. Therefore, the size of the detector is only limited to the size of good-quality CZT crystal that can be grown. Future studies should consider this fact into the design. Once a  $2 \times 2$  array detector is successfully fabricated and good results are demonstrated, then a  $3 \times 2$  or a  $3 \times 3$  array should be constructed.

One important drawback to a larger arrayed detector is the increased complexity that will result. For every grid pair that is added to the design, 2 more readout channels will be necessary. Although this can be done relatively simply, it will be at a cost which may be deviating away from the original intent of this readout system. However, in the end it will be up to the user to determine if the benefits of good spectroscopic performance and good detection efficiency outweigh the disadvantages of greater complexity.

Lastly, advanced ASIC technology has recently been developed for coplanar grid detectors [73]. This technology allows for all of the capabilities from the detector box shown in Figure 3.6, which includes 3 charge sensitive preamplifiers and a variable gain subtraction circuit, to be shrunk down to an ASIC chip which can fit onto one's fingertip. In addition, timing information is also available on this chip, which can be used as another tool for depth sensing. More testing of this ASIC should be conducted so that eventually this technology can be implemented with future coplanar grid detectors. Detectors employing the multi-pair coplanar grid design could greatly benefit by this technology, since the readout electronics could be fit into a much smaller package than by using traditional discrete readout electronics. Such technology will ultimately allow for more portable gamma-ray detectors, making the coplanar grid detector an even more appealing gamma-ray detection device.

## BIBLIOGRAPHY

## BIBLIOGRAPHY

- [1] G. F. Knoll, *Radiation Detection and Measurement*, 3rd ed. New York: John Wiley and Sons, Inc., 2000.
- [2] D. S. McGregor and H. Hermon, "Room-temperature compound semiconductor radiation detectors," *Nuclear Instruments and Methods in Physics Research Section A*, vol. 395, no. 1, pp. 101–124, 1997.
- [3] E. Sakai, "Present Status of Room Temperature Semiconductor Detectors," *Nuclear Instruments and Methods in Physics Research*, vol. 196, pp. 121–130, 1982.
- [4] W. Akutagawa, K. Zanio, and J. Mayer, "CdTe as a gamma detector," *Nuclear Instruments and Methods in Physics Research*, vol. 55, pp. 383–385, 1967.
- [5] A. Cornet, P. Siffert, and A. Coche, "Cadmium telluride surface barrier detectors," *Applied Physics Letters*, pp. 432–6, 1970.
- [6] M. Cuzin, "Some new developments in the field of high atomic number materials," *Nuclear Instruments and Methods in Physics Research Section A: Accelerators, Spectrometers, Detectors and Associated Equipment*, vol. 253, pp. 407–417, 1987.
- [7] R. Bell, G. Entine, and H. Serreze, "Time-dependent polarization of CdTe gamma-ray detectors," *Nuclear Instruments and Methods in Physics Research*, vol. 117, pp. 267–271, 1974.
- [8] P. Siffert, J. Berger, C. Scharager, A. Cornet, R. Stuck, R. Bell, H. Serreze, and F. Wald, "Polarization in cadmium telluride nuclear radiation detectors," *IEEE Transactions on Nuclear Science*, vol. 23, no. 1, pp. 159–170, 1976.
- [9] W. Willig, "Mercury iodide as a gamma spectrometer," *Nuclear Instruments and Methods*, vol. 96, no. 4, pp. 615–16, 1971.
- [10] —, "Large bandgap mercury and lead compounds for nuclear particle detection," *Nuclear Instruments and Methods*, vol. 101, no. 1, pp. 23–4, 1972.
- [11] S. Swierkowski, G. Armantrout, and R. Wichner, "High-resolution HgI<sub>2</sub> X-ray spectrometers," *Applied Physics Letters*, vol. 23, no. 5, pp. 281–2, 1973.
- [12] K. Hull, A. Beyerle, B. Lopez, J. Markakis, C. Ortale, W. Schnepple, and L. van den Berg, "Recent developments in thick mercuric iodide spectrometers," *IEEE Transactions on Nuclear Science*, vol. 30, no. 1, pp. 402–404, 1983.
- [13] J. Baciak and Z. He, "Spectroscopy on thick HgI<sub>2</sub> detectors: a comparison between planar and pixelated electrodes," *Nuclear Science, IEEE Transactions on*, vol. 50, no. 4, pp. 1220–1224, 2003.
- [14] T. Mohammed-Brahim, A. Friant, and J. Mellet, "Structure MIS effects on polarization of HgI<sub>2</sub> crystals used for gamma-ray detection," *IEEE Transactions on Nuclear Science*, vol. 32, no. 1, pp. 581–584, 1985.

- [15] V. Gerrish, "Polarization and gain in mercuric iodide gamma-ray spectrometers," *Nuclear Instruments and Methods in Physics Research Section A*, vol. 322, no. 3, pp. 402–413, 1992.
- [16] J. Butler, C. Lingren, and F. Doty, "Cd<sub>1-x</sub>Zn<sub>x</sub>Te gamma ray detectors," *Nuclear Science, IEEE Transactions on*, vol. 39, no. 4, pp. 605–609, 1992.
- [17] J. Toney, B. Brunett, T. Schlesinger, J. van Scyoc, R. James, M. Schieber, M. Goorsky, H. Yoon, E. Eissler, and C. Johnson, "Uniformity of Cd<sub>1-x</sub>Zn<sub>x</sub>Te grown by high-pressure Bridgman," *Nuclear Instruments and Methods in Physics Research Section A: Accelerators, Spectrometers, Detectors and Associated Equipment*, vol. 380, no. 1-2, pp. 132–135, 1996.
- [18] L. Jones and P. Woodlam, "Resolution Improvement in CdTe Gamma Detectors Using Pulse-Shape Discrimination," *Nuclear Instruments and Methods in Physics Research*, vol. 124, pp. 591–595, 1975.
- [19] M. Richter and P. Siffert, "High resolution gamma ray spectroscopy with CdTe detector systems," *Nuclear Instruments and Methods in Physics Research Section A: Accelerators, Spectrometers, Detectors and Associated Equipment*, vol. 322, no. 3, pp. 529–537, 1992.
- [20] O. Frisch, *British Atomic Energy Report*, vol. BR-49, 1944.
- [21] A. Bolotnikov and B. Ramsey, "Improving the energy resolution of high-pressure Xe cylindrical ionization chambers," *Nuclear Science, IEEE Transactions on*, vol. 44, no. 3, pp. 1006–1010, 1997.
- [22] P. N. Luke, "Single-polarity charge sensing in ionization detectors using coplanar electrodes," *Applied Physics Letters*, vol. 65, no. 22, pp. 2884–2886, 1994.
- [23] H. H. Barrett, J. D. Eskin, and H. B. Barber, "Charge Transport in Arrays of Semiconductor Gamma-Ray Detectors," *Physical Review Letters*, vol. 75, no. 1, pp. 156 LP – 159, 1995.
- [24] H. B. Barber, D. G. Marks, B. A. Apotovsky, F. L. Augustine, H. H. Barrett, J. F. Butler, E. L. Dereniak, F. P. Doty, J. D. Eskin, and W. J. Hamilton, "Progress in developing focal-plane-multiplexer readout for large CdZnTe arrays for nuclear medicine applications," *Nuclear Instruments and Methods in Physics Research Section A: Accelerators, Spectrometers, Detectors and Associated Equipment*, vol. 380, no. 1-2, pp. 262–265, 1996.
- [25] D. Marks, H. Barber, H. Barrett, E. Dereniak, J. Eskin, K. Matherson, J. Woolfenden, E. Young, F. Augustine, W. Hamilton, J. Venzon, B. Apotovsky, and F. Doty, "A 48 × 48 CdZnTe array with multiplexer readout," *Nuclear Science, IEEE Transactions on*, vol. 43, no. 3, pp. 1253–1259, 1996.
- [26] Z. He, W. Li, G. F. Knoll, D. K. Wehe, J. Berry, and C. M. Stahle, "3-D position sensitive CdZnTe gamma-ray spectrometers," *Nuclear Instruments and Methods in Physics Research Section A: Accelerators, Spectrometers, Detectors and Associated Equipment*, vol. 422, no. 1-3, pp. 173–178, 1999.
- [27] M. Hage-Ali, J. M. Koebel, R. Regal, P. Siffert, V. Prat, and H. Simon, "Cadmium telluride small probes for gamma-ray spectrometry," *Nuclear Instruments and Methods in Physics Research Section A: Accelerators, Spectrometers, Detectors and Associated Equipment Proceedings of the 9th International Workshop on Room Temperature Semiconductor X- and  $\gamma$ -Ray Detectors, Associated Electronics and Applications*, vol. 380, no. 1-2, pp. 427–430, 1996.
- [28] D. McGregor, Z. He, H. Seifert, R. Rojeski, and D. Wehe, "CdZnTe semiconductor parallel strip Frisch grid radiation detectors," *Nuclear Science, IEEE Transactions on*, vol. 45, no. 3, pp. 443–449, 1998.



- [29] D. S. McGregor, R. A. Rojeski, Z. He, D. K. Wehe, M. Driver, and M. Blakely, "Geometrically weighted semiconductor Frisch grid radiation spectrometers," *Nuclear Instruments and Methods in Physics Research Section A: Accelerators, Spectrometers, Detectors and Associated Equipment*, vol. 422, no. 1-3, pp. 164–168, 1999.
- [30] E. Y. Lee and R. B. James, "Device simulation and optimization of laterally-contacted-unipolar-nuclear detector," *Nuclear Instruments and Methods in Physics Research Section A: Accelerators, Spectrometers, Detectors and Associated Equipment*, vol. 428, no. 1, pp. 66–71, 1999.
- [31] J. F. Butler, "Novel electrode design for single-carrier charge collection in semiconductor nuclear radiation detectors," *Nuclear Instruments and Methods in Physics Research Section A: Accelerators, Spectrometers, Detectors and Associated Equipment*, vol. 396, no. 3, pp. 427–430, 1997.
- [32] G. Montemont, M. Arques, L. Verger, and J. Rustique, "A capacitive Frisch grid structure for CdZnTe detectors," *Nuclear Science, IEEE Transactions on*, vol. 48, no. 3, pp. 278–281, 2001.
- [33] Z. He, "Review of the Shockley-Ramo theorem and its application in semiconductor gamma-ray detectors," *Nuclear Instruments and Methods in Physics Research Section A: Accelerators, Spectrometers, Detectors and Associated Equipment*, vol. 463, no. 1-2, pp. 250–267, 2001.
- [34] P. Luke, "Unipolar charge sensing with coplanar electrodes-application to semiconductor detectors," *Nuclear Science, IEEE Transactions on*, vol. 42, no. 4, pp. 207–213, 1995.
- [35] P. Luke and E. Eissler, "Performance of CdZnTe coplanar-grid gamma-ray detectors," *Nuclear Science, IEEE Transactions on*, vol. 43, no. 3, pp. 1481–1486, 1996.
- [36] P. N. Luke, "Electrode configuration and energy resolution in gamma-ray detectors," *Nuclear Instruments and Methods in Physics Research Section A: Accelerators, Spectrometers, Detectors and Associated Equipment*, vol. 380, no. 1-2, pp. 232–237, 1996.
- [37] Z. He, "Potential distribution within semiconductor detectors using coplanar electrodes," *Nuclear Instruments and Methods in Physics Research Section A: Accelerators, Spectrometers, Detectors and Associated Equipment*, vol. 365, no. 2-3, pp. 572–575, 1995.
- [38] Z. He, G. F. Knoll, D. K. Wehe, R. Rojeski, C. H. Mastrangelo, M. Hammig, C. Barrett, and A. Uritani, "1-D position sensitive single carrier semiconductor detectors," *Nuclear Instruments and Methods in Physics Research Section A: Accelerators, Spectrometers, Detectors and Associated Equipment*, vol. 380, no. 1-2, pp. 228–231, 1996.
- [39] Z. He, G. F. Knoll, D. K. Wehe, and J. Miyamoto, "Position-sensitive single carrier CdZnTe detectors," *Nuclear Instruments and Methods in Physics Research Section A: Accelerators, Spectrometers, Detectors and Associated Equipment*, vol. 388, no. 1-2, pp. 180–185, 1997.
- [40] Z. He, G. F. Knoll, D. K. Wehe, and Y. F. Du, "Coplanar grid patterns and their effect on energy resolution of CdZnTe detectors," *Nuclear Instruments and Methods in Physics Research Section A: Accelerators, Spectrometers, Detectors and Associated Equipment*, vol. 411, no. 1, pp. 107–113, 1998.
- [41] P. Luke, M. Amman, T. Prettyman, P. Russo, and D. Close, "Electrode design for coplanar-grid detectors," *Nuclear Science, IEEE Transactions on*, vol. 44, no. 3, pp. 713–720, 1997.
- [42] W. Shockley, "Currents to conductors induced by a moving point charge," *Journal of Applied Physics*, vol. 9, p. 635, 1938.
- [43] S. Ramo, "Currents induced by electron motion," *Proceedings of the I.R.E.*, vol. 27, p. 584, 1939.

- [44] C. Jen, "On the induced current and energy balance in electronics," *Proceedings of the I.R.E.*, p. 345, 1941.
- [45] G. Cavalleri, et al., "Extension of Ramo's theorem as applied to induced charge in semiconductor detectors," *Nuclear Instruments and Methods in Physics Research*, vol. 92, p. 137, 1971.
- [46] D. Griffiths, *Introduction to Electrodynamics*, 2nd ed. Upper Saddle River, New Jersey: Prentice Hall, 1989.
- [47] T. Schlesinger and R. James, Eds., *Semiconductors for Room Temperature Nuclear Detector Applications*, ser. Semiconductors and Semimetals, 1995, vol. 43.
- [48] Ansoft, *Maxwell 3D*, Ansoft, Four Station Square, Suite 200, Pittsburgh, PA 15219, USA.
- [49] National Instruments Corporation, 11500 N Mopac Expwy, Austin, TX 78759-3504, USA.
- [50] eV Products, 375 Saxonburg Boulevard, Saxonburg, PA 16056, USA.
- [51] Yinnel Tech, 3702 West Sample St., Suite 1109, South Bend, IN 46619, USA.
- [52] BSI Ltd., 26 Ganibu dambis, P.O. Box 33, Riga, LV-1005, Latvia.
- [53] J. Pérez, Z. He, D. Wehe, and Y. Du, "Estimate of large CZT detector absolute efficiency," *Nuclear Science, IEEE Transactions on*, vol. 49, no. 4, pp. 2010–2018, 2002.
- [54] Z. He and B. W. Sturm, "Characteristics of depth-sensing coplanar grid CdZnTe detectors," *Nuclear Instruments and Methods in Physics Research Section A: Accelerators, Spectrometers, Detectors and Associated Equipment*, vol. 554, no. 1-3, pp. 291–299, 2005.
- [55] M. Amman and P. Luke, "Optimization criteria for coplanar-grid detectors," *Nuclear Science, IEEE Transactions on*, vol. 46, no. 3, pp. 205–212, 1999.
- [56] L. Li, F. Lu, K. Shah, M. Squillante, L. Cirignano, W. Yao, R. Olson, P. Luke, Y. Nemirovsky, A. Burger, G. Wright, and R. James, "A new method for growing detector-grade cadmium zinc telluride crystals," *Nuclear Science Symposium Conference Record, 2001 IEEE*, vol. 4, pp. 2396–2400, 2001.
- [57] K. Hecht, "Zum Mechanismus des lichtelektrischen Primärstromes in isolierenden Kristallen," *Zeitschrift für Physik A, Hadrons and Nuclei*, vol. 77, no. 3, pp. 235–245, 1932.
- [58] Z. Burshtein, H. N. Jayathirtha, A. Burger, J. F. Butler, B. Apotovsky, and F. P. Doty, "Charge-carrier mobilities in  $\text{Cd}_{0.8}\text{Zn}_{0.2}\text{Te}$  single crystals used as nuclear radiation detectors," *Applied Physics Letters*, vol. 63, no. 1, pp. 102–104, 1993.
- [59] A. Davies, A. Lohstroh, M. Ozsan, and P. Sellin, "Spatial uniformity of electron charge transport in high resistivity CdTe," *Nuclear Instruments and Methods in Physics Research, Section A: Accelerators, Spectrometers, Detectors and Associated Equipment*, vol. 546, no. 1-2, pp. 192–199, 2005.
- [60] V. Gostilo, I. Lisjutin, A. Loupilov, and V. Ivanov, "Performance improvement of large volume CdZnTe detectors," in *2004 IEEE Nuclear Science Symposium Conference Record*, vol. Vol. 7, 2004, pp. 4590–5.
- [61] Z. He, G. F. Knoll, and D. K. Wehe, "Direct measurement of product of the electron mobility and mean free drift time of CdZnTe semiconductors using position sensitive single polarity charge sensing detectors," *Journal of Applied Physics*, vol. 84, no. 10, pp. 5566–5569, 1998.
- [62] B. Sturm, Z. He, T. Zurbuchen, and P. Koehn, "Investigation of the asymmetric characteristics and temperature effects of CdZnTe detectors," *Nuclear Science, IEEE Transactions on*, vol. 52, no. 5, pp. 2068–2075, 2005.

- [63] G. Wright, Y. Cui, U. Roy, C. Barnett, K. Reed, A. Burger, F. Lu, L. Li, and R. James, "The effects of chemical etching on the charge collection efficiency of 111 oriented  $\text{Cd}_{0.9}\text{Zn}_{0.1}\text{Te}$  nuclear radiation detectors," *Nuclear Science, IEEE Transactions on*, vol. 49, no. 5, pp. 2521–2525, 2002.
- [64] S. Agostinelli, J. Allison, K. Amako, J. Apostolakis, H. Araujo, P. Arce, M. Asai, D. Axen, S. Banerjee, and G. Barrand, "G4—a simulation toolkit," *Nuclear Instruments and Methods in Physics Research Section A: Accelerators, Spectrometers, Detectors and Associated Equipment*, vol. 506, no. 3, pp. 250–303, 2003.
- [65] S. Kiff, Z. He, and G. Tepper, "Radial position sensing in a coplanar-grid high-pressure xenon gamma-ray spectrometer," *Nuclear Science, IEEE Transactions on*, vol. 53, no. 3, pp. 1380–1384, 2006.
- [66] G. Carini, A. Bolotnikov, G. Camarda, G. Wright, G. De Geronimo, D. Siddons, and R. James, "Synchrotron radiation response characterization of coplanar grid CZT detectors," *Nuclear Science, IEEE Transactions on*, vol. 52, no. 5, pp. 1941–1944, 2005.
- [67] L. Qiang and J. Wanqi, "Surface passivation and electrical properties of  $p\text{-CdZnTe}$  crystal," *Semiconductor Science and Technology*, vol. 21, no. 1, p. 72, 2006.
- [68] G. W. Wright, D. Chinn, B. A. Brunett, M. J. Mescher, J. C. Lund, R. W. Olsen, F. P. Doty, T. E. Schlesinger, R. B. James, K. Chattopadhyay, R. C. Wingfield, and A. Burger, "Exploratory search for improved oxidizing agents used in the reduction of surface leakage currents of  $\text{CdZnTe}$  detectors," in *Hard X-Ray, Gamma-Ray, and Neutron Detector Physics*, R. B. James and R. C. Schirato, Eds., vol. 3768. SPIE, 1999, pp. 481–485.
- [69] F. Zhang, "Events Reconstruction in 3-D Position Sensitive  $\text{CdZnTe}$  Gamma Ray Spectrometers," Ph.D. dissertation, University of Michigan, 2005.
- [70] W. Murray, K. Krueger, M. Rawool-Sullivan, L. Ussery, and C. Whitley, "Temperature effects on  $\text{CdZnTe}$  detector performance," in *1998 IEEE Nuclear Science Symposium Conference Record, 8-14 Nov. 1998*, vol. vol.1, 1998, pp. 643–5.
- [71] A. Niemelä and H. Sipilä, "Performance of a cooled  $\text{CdZnTe}$  X-ray detector," in *Nuclear Science Symposium and Medical Imaging Conference, 1994., 1994 IEEE Conference Record*, vol. 1, 1994, pp. 139–142.
- [72] M. Amman, J. Lee, and P. Luke, "Temperature Study of  $\text{CdZnTe}$  Coplanar-Grid Detectors," *Nuclear Science, IEEE Transactions on*, vol. 53, no. 5, pp. 3035–3040, 2006.
- [73] G. De Geronimo, G. Carini, W. Murray, and P. O'Connor, "Front-end ASIC for Co-Planar grid sensors," *IEEE Transactions on Nuclear Science*, vol. 52, no. 5, pp. 2003–8, 2005.
- [74] F. Zhang, Z. He, G. Knoll, D. Wehe, and J. Berry, "3-D position sensitive  $\text{CdZnTe}$  spectrometer performance using third generation VAS/TAT readout electronics," *Nuclear Science, IEEE Transactions on*, vol. 52, no. 5, pp. 2009–2016, 2005.
- [75] M. Amman, J. S. Lee, and P. N. Luke, "Electron trapping nonuniformity in high-pressure-Bridgman-grown  $\text{CdZnTe}$ ," *Journal of Applied Physics*, vol. 92, no. 6, p. 3198, 2002.
- [76] Z. He, W. Li, G. F. Knoll, D. K. Wehe, and C. M. Stahle, "Measurement of material uniformity using 3-D position sensitive  $\text{CdZnTe}$  gamma-ray spectrometers," *Nuclear Instruments and Methods in Physics Research Section A: Accelerators, Spectrometers, Detectors and Associated Equipment*, vol. 441, no. 3, pp. 459–467, 2000.